Compressible Convection and Subduction: Kinematic and Dynamic Modeling

Changyeol Lee

Dissertation submitted to the faculty of the Virginia Polytechnic Institute and State University in partial fulfillment of the requirements for the degree of

Doctor of Philosophy
In
Geosciences

Scott D. King
John A. Hole
Chester J. Weiss
Ross J. Angel
Peter E. van Keken

Oct, 5th, 2010
Blacksburg, Virginia

Keywords: Subduction zone, Numerical model, Compressibility, Viscous dissipation, High-Mg# andesite, Aleutian island arc, Periodic slab buckling

Compressible Convection and Subduction: Kinematic and Dynamic Modeling

Changyeol Lee

(ABSTRACT)

Subduction is a dynamic and time-dependent process which requires time-dependent models for its study. In addition, due to the very high pressures within the Earth's interior, an evaluation of the role of compressibility in subduction studies should be undertaken. However, most subduction studies have been conducted by using kinematic, steady-state, and/or incompressible mantle convection models; these simplifications may miss important elements of the subduction process. In this dissertation, I evaluate the effects of time-dependence and compressibility on the evolution of subduction by using 2-D Cartesian numerical models.

The effect of compressibility on the thermal and flow structures of subduction zones is evaluated by using kinematically prescribed slab and steady-state models. The effect of compressibility is primarily expressed as an additional heat source created by viscous dissipation. The heat results in thinner thermal boundary layer on the subducting slab and increases slab temperatures. With that exception, the effect of compressibility is relatively small compared with, for example, the effect of the mantle rheology on the thermal and flow structures of the mantle wedge.

Plate reconstruction models show that the convergence rate and age of the incoming plate to trench vary with time, which poses a problem for steady-state subduction models. Thus, I consider the time-dependent convergence rate and age of the incoming plate in the kinematic-dynamic subduction models in order to understand the localization of high-Mg# andesites in the western Aleutians. The results show that the localization of high-Mg# andesites is a consequence of the time-dependent convergence rate and slab age along the Aleutian arc.

The influence of mantle and slab parameters as well as compressibility on the slab dynamics is evaluated by using 2-D dynamic subduction models. The results demonstrate that periodic slab buckling in the mantle results in periodic convergence rate and dip of the subducting slab; time-dependence is a natural expression of subduction. The effect of compressibility on the slab dynamics is not significant. The periodic convergence rate and dip of the subducting slab explain time-dependent seafloor spreading at the mid-ocean ridge, convergence rate of the oceanic plate at trench and arc-normal migration of arc volcanoes.

DEDICATION

This dissertation is dedicated to my parents, who allowed me to exist in the World, have given me their endless loves, and have supported me during my life.

ACKNOWLEDGEMENTS

First of all, I would like to express my countless thanks to my advisor, Dr. Scott King who has been my teacher, supervisor and friend during my Ph. D. program. To me, 'Teacher – 선생 in Korean' has a special meaning: I use the word for the person who has intellectually and humanely guided people. Thus, I do not hesitate to call Dr. King my teacher who allowed me to endeavor in the Earth's interior with his intelligences and humane guides. Without his patience and encouragements, I do never finish my Ph. D. program.

Also, I would like to thanks to my committee members, Dr. John Hole, Dr. Ross Angel, Dr. Chester Weiss and Dr. Peter van Keken who provided me prominent opportunities to enjoy my studies, classes and even chats. Dr. Hole gave me plenty of seismological intelligences and humors. Dr. Angel has improved my backgrounds related to mineral physics though I am still a novice in Mineralogy. Dr. Weiss gave me intelligent backgrounds of Geomagnetisms which are helpful to understand the Earth's interior. In addition, I had an excellent chance to be involved in his undergraduate class of Geophysics as a TA. I have many feedbacks from Dr. van Keken regarding my studies with his specialties in Geodynamic modeling and Geophysics. Although she is not on the list of my committee members, I would like to thank to Dr. Ying Zhou for her numberless contributions to my studies.

Here, I would like to express many thanks to my undergraduate advisor, Dr. Youngdo Park who let me to know a 'new world' in Geology. I met him when I was a freshman and we have kept fantastic relations since 1999. He made me to learn fundamental basics for my Ph. D. program: He is the other 'teacher' of mine with Dr. King. I am a very fortunate person because I already have two great teachers during my undergraduate and graduate programs.

I owe many people of the department of Geosciences at the Virginia Tech. At first, I deeply appreciate Ms. Connie Lowe's numerous technical assistants for my Ph. D. program. She always has processed many tedious documentary works very precisely. Also, Ms. Carolyn Williams, Ms. Mary McMurray, Ms. Linda Bland and Ms. Ellen Mathena gave me countless helps to finish my Ph. D. degree smoothly. I will remember their smiles and kindness during my life. I need to thank to Mr. Mark Lemon and Mr. Miles Gentry who gave me plenty of computational and technical assistants.

I have many friends and colleagues of the department of Geosciences. Mr. Youyi Ruan is the first friend I met at the Virginia Tech. I always like to chat with him regarding studies and others. I also enjoyed nattering with his wife, Ms. Wei Ruan who recently became a graduate student at the Virginia Tech. Liang Han (Panda) is also a good friend of mine here. He is much younger than me but, his mature

personality always made it possible to enjoy chats with him. I do not hesitate to express my thanks to Ms. Pavithra Sekhar, Ms. Karina Cheung and Ms. Tannistha Maiti who are excellent colleagues and friends under the same advisor, Dr. King. I also would like to thanks to Ms. Carol Johnson, Ms. Rebecca French, Ms. Lindsay Kolbus, Ms. Kate Craft, Ms. Aida Farough, Ms. Sharmin Shamsalsadati, Mr. Eric Kazlaukas, Mr. Kui Liu, Mr. Oluyinka Oyewumi, Mr. Di Wang, Mr Kai Wang, Mr. Cable Warren and Mr. Samuel Fortson for their friendships. I regret not to enumerate all the friends at the Virginia Tech here.

Here, I would like to express numberless thanks to my Korean friends who have supported me. Mr. Jungwon Jun and Ms. Miye Cha have been my best friends during my life. Although we could not frequently meet since the friends stay in the Republic of Korea, they have encouraged me through e-mails, mails, msn and telephone. Without their friendships and supports, my studies in the USA should have been much difficult. Mr. Jinyong Sung has been another excellent friend helped me a lot during the early days in the USA. I am also very fortunate in that I made friendships with Dr. Eunkyung Jung and Dr. Ilhan Kim in the USA. Mr. Donghyun Choi has been a very good friend and alumni since 2000. Dr. Eunseo Choi and Dr. Bojeong Kim are my respectable friends who helped me for years. I cannot miss to notify my roommates, Mr. Jungyong Lee and Mr. Seunguk Hur for their humors and kindness. At last, I would like to thank to Dr. Park's wife and daughter, Ms. Kyunghee Park and Ms. Hemi Park for their kindness and encouragements.

At last, I have to express my deepest thanks to my parents and family who always have supported me financially and mentally. I cannot be physically existed here unless my parents' endless loves and affections on me. My two brothers, a sister, two sisters in-law and a brother in-law always are the people whom I count on during my studies in the USA. Also, I owe my uncle, aunt, and two cousins for their affections and concerns on me. I would like to thank to my relatives although I cannot list all the people here.

TABLE OF CONTENTS

LIST OF FIGURES

Chapter 2

Chapter 3

Chapter 4

LIST OF TABLES

Chapter 2

Chapter 4

Chapter 1

Introduction

1.1 Mantle Convection and Subduction

History is full of fascinating accounts of speculation regarding the Earth's interior. Ancient natural philosophers thought that volcanoes, earthquakes and mountain ranges are attributed to the deforming molten rocks in the Earth's interior. The concept that the Earth's interior is molten had been succeeded to 18th century's scientists; Newton and Laplace suggested that the molten Earth's interior allows the equatorial bulge of the Earth. However, most of our present understanding of the Earth's interior has come through the modern scientific instrumentations and techniques developed since 19th century. Early seismological and tidal surveys conducted in late 19th and early 20th centuries suggested a contradictory interpretation of the Earth's interior; the Earth's interior except for the outer core consists of layered elastic bodies of which bulk and shear moduli are even larger than those of hard steel [*Darwin*, 1898; *Jeffreys*, 1929]. The Earth's small deviatoric stresses were considered too weak to deform the hard Earth's interior; mantle deformation was not accepted by many scientists.

However, a series of evidence from geophysical and geological observations incessantly suggest that the Earth's interior has been largely deformed through time, contrasting the very hard Earth's interior estimated by the seismological and tidal studies. Analog experiments and topography analyses show that viscous flow of the Earth's interior explains the mountain building, sea trench and postglacial rebounding since the post-ice-age [*Haskell*, 1935; *Pekeris*, 1935; *Hales*, 1936; *Griggs*, 1939]. The diverse and reliable geological evidence derived a meteorologist, Alfred Wegener to hypothesize, 'continental drift'; deformation of the Earth's interior transposes and breaks the large continents throughout the Earth's history [*Wegener*, 1924]. In spite of the fact that the hypothesis of continental drift explains the

observations, the hypothesis was extensively criticized by scientists because Wegener could not provide a reasonable driving force for the large mantle deformation. Therefore, the hypothesis was abandoned and the resurrection of the hypothesis had to wait after the World War II. The seafloor and paleomagnetism surveys conducted throughout the Atlantic seafloor show that the oceanic plate has laterally spread from the mid-ocean ridge over millions of years, which indicates the Earth's fluid-like deformation [*Mason*, 1958; *Hess*, 1962]. The contradiction between the seismological observations (suggesting elastic body) and the geophysical and geological observations (suggesting fluid-like body) was resolved when subsolidus solid-state flow (creeping) of the elastic materials was suggested as a reasonable deformation mechanism under the geological time scale and conditions [*Gorden*, 1967]. Finally, the theory of plate tectonics, one of the most important achievements in Earth sciences, was established [e.g., *Wilson*, 1963; *McKenzie and Parker*, 1967; *Morgan*, 1968; *Atwater*, 1970].

While plate tectonics is a kinematic concept to explain Earth's surface deformation and evolution, it conveys the style of mantle convection occurring in the Earth's interior [*Oxburgh and Turcotte*, 1968; *Forsyth and Uyeda*, 1975; *Parmentier et al.*, 1976]. The thermal instability above the core-mantle boundary (CMB) has been considered the birthplace for the upwelling [*Morgan*, 1971; *Sleep*, 1992; *Kellogg and King*, 1997] though the rheological and compositional boundary between the upper and lower mantle (660 km discontinuity) has been suggested as a birthplace of the secondary upwelling [*McKenzie and O'Nions*, 1983; *Allègre and Turcotte*, 1985; *Courtillot et al.*, 2003]. The downwelling could be categorized into two; delamination from the bottom of the oceanic/continental plates [*Chalot-Prat and Girbacea*, 2000; *Zegers and van Keken*, 2001] and subduction of the oceanic plate at the trench [*Stern*, 2002; *Hansen*, 2007 and references therein]. Throughout this thesis, I will primarily discuss the one of downwellings, subduction.

1.2 Subduction Zones: Observations

The very high temperatures and pressures of the Earth's interior frustrate our attempts to access to the Earth's interior. In 2005, the Japanese advanced drilling vessel, 'Chikyu' (Earth in Japanese) was constructed to endeavor the Earth's interior by drilling down to the uppermost upper mantle but, the expected accessible depth is only down to ~7 km, literally the Earth's shallowest outer shell, the crust. Therefore, understanding of the evolution of subduction zones has been facilitated by indirect methods, as described below.

First of all, seismology should be one of the most well-known methods to infer the evolution of subduction from the top to the bottom. Seismic tomographic studies reveal 1) the geometry of subducting slabs expressed as Wadati-Benioff zones from analyses of earthquake epicenters [e.g., *Isacks and Molnar*, 1971; *Engdahl et al.*, 1998; *Syracuse and Abers*, 2006], 2) global compilation of slab dips ranging from vertical to flat [e.g., *Jarrard*, 1986; *Sdrolias and Müller*, 2006; *Li et al.*, 2008], 3) complex features including slab tearing and detachment [e.g., *Chatelain et al.*, 1992; *Miller et al.*, 2005] and 4) stagnant slab above the 660 km discontinuity [e.g., *Fukao et al.*, 2001; *Li et al.*, 2008]. In addition, other tomographic studies have shown that subducted slabs in the mantle are not linear features and interact with phase transitions and/or viscosity increases in the transition zone [e.g., *Karason and van der Hilst*, 2001; *Ren et al.*, 2007]. The seismology further infers the deepest slab structures in the core-mantle boundary (CMB); an accumulation of the ancient subducted material has been proposed in order to explain the observed seismic anisotropy around the core-mantle boundary [e.g., *Kendall and Silver*, 1996; *Lay et al.*, 1998].

Along with the seismological studies, gravity, geomagnetic and geodetic studies have been conducted to understand the evolution of subduction zones. The geoid, or departure of gravitational potential field from a reference ellipsoid, has local maxima above the Tonga-Kermadec, New Guinea and Japanese subduction zones; slab strengths and viscosity profiles of the mantle such as viscosity increases across the 660 km discontinuity are constrained by analyzing the geoid data [e.g., *Hager et al.*, 1985; *Hager and Richards*, 1989; *King and Masters*, 1992; *Forte and Mitrovica*, 1996]. Geomagnetism studies measuring susceptibility of the mantle minerals have inferred the effect of the slab dehydrations on the

distribution of hydrated minerals (serpentine and/or chlorite) in the mantle wedge and deep mantle [e.g., *Kido et al.*, 2004; *Blakely et al.*, 2005; *Kelbert et al.*, 2009]. With the help of satellites and GPS stations, accumulated GPS monitoring data allows Earth scientists to quantitatively analyze the plate rebounds and uplift in the subduction zones (e.g., forearc bulge); rheology of the subducting slab and overriding continental/oceanic lithosphere is constrained [e.g., *Dragert and Hyndman*, 1995; *Rogers and Dragert*, 2003; *Leonard et al.*, 2004].

In addition to the geophysical observations, geological studies including petrology and geochemistry have been facilitated to infer the evolution of subduction zones. Compared with the intraplate volcanisms (e.g., Hawaii), arc volcanoes have experienced diverse igneous activities related to the interaction between the subducting slab and overlying mantle wedge [*Peacock et al.*, 1994; *Ulmer*, 2001; *Kelemen et al.*, 2003]. Subduction zones are thought to be the only place where flux melting occurs; the dehydrated fluids from the subducting slab decrease the solidus of the mantle wedge, which results in melting of the mantle wedge [*Kawamoto and Holloway*, 1997; *Ulmer*, 2001; *Grove et al.*, 2006]. Also, subduction zones are important in the studies of continental genesis; high-Mg# andesites (e.g., Adakite) similar to bulk composition of the continents are thought to be generated by the slab melting [*Kay*, 1978; *Yogodzinski and Kelemen*, 1998; *Kelemen et al.*, 2003].

1.3 Subduction Zones: Modeling

Lifetime of the typical subduction zone spans approximately 200 Myr while the time scale of seismic tomography images, geoid and topography and GPS data is restricted to a snapshot of the present-day state of the slab. These observations are insufficient to infer subduction dynamics without additional insights provided by laboratory (analog) and numerical modeling. Laboratory modeling was used to infer the evolution of subduction zones; one or mixed of sand, silly-putty, honey and corn syrup, etc are used for imitating the rheology of the oceanic plate and mantle. Although simplified rheology as well as initial

and boundary conditions are different than the Earth's, the results of laboratory modeling experiments contribute to first-order understanding of the evolution of subduction zones [e.g., *Guillou-Frottier et al.*, 1995; *Funiciello et al.*, 2003b; *Guillaume et al.*, 2009].

Along with laboratory modeling, numerical models have become a useful tool for mantle convection research [e.g., *Richter*, 1973; *Schubert and Zebib*, 1980; *Moresi and Solomatov*, 1998; *Tan and Gurnis*, 2007]. The principle equations relevant to the mantle approximated as a very stiff fluid are the Navier-Stokes equations derived in early 19th century [*Schubert et al.*, 2001]. However, the solution of the partial differential equation (PDE) can be attained with the idealized initial and boundary conditions only, which are not relevant to the Earth's complex conditions. In order to solve the PDE, numerical approximations such as finite difference (FD) or finite element (FE) methods were developed through 19th and 20th centuries but, the huge amount of calculations even for a simple model prevented the numerical methods from being applied to Earth sciences. However, faster and cheaper computers with enhanced numerical techniques allow Earth scientists to access large scale computations with complex mantle and subduction parameters [e.g., *King et al.*, 1990; *Zhong et al.*, 2000; *O'Neill et al.*, 2006]. Numerical modeling has several advantages compared with laboratory modeling; compressibility and relevant adiabatic gradient, large viscosity variations and melting of mantle and slab can be considered in numerical models and are difficult or impossible in laboratory modeling.

In order to understand the evolution of subduction zones, numerous numerical modeling studies have been conducted for decades [*King*, 2007; *Billen*, 2008 and references therein]. Among them, kinematic-dynamic subduction models have been used to constrain the thermal and flow structures of subduction zones since 1960's [e.g., *McKenzie*, 1969; *Minear and Toksoz*, 1970; *Peacock and Wang*, 1999; *Billen and Hirth*, 2007]. Some of the findings include: 1) the extent of the updip and downdip ruptures which limit the depth and location of great earthquakes in subduction zones [e.g., *Hyndman and Wang*, 1993; *Hyndman et al.*, 1995; *Oleskevich et al.*, 1999], 2) distribution of slab and mantle melting in the mantle wedge which controls origin and distribution of arc volcanoes [e.g., *Iwamori*, 1998; *Gerya and*

Yuen, 2003; *Grove et al.*, 2006] and 3) style of metamorphism occurring in the subducting slab which constrains the depth of slab dehydration [e.g., *Peacock*, 1996; *van Keken et al.*, 2002; *Grove et al.*, 2009].

In the kinematic-dynamic subduction models addressing many problems, the slab buoyancy, the driving force for subduction, is neglected; thus the subducting slab is kinematically prescribed as a boundary condition. However, slab buoyancy is needed to be considered if our interests are focused on the slab deformation in the deeper mantle. Therefore, fully dynamic subduction models allowing free slab deformation have been facilitated though there are still limitations such as the implementation of the thrust between the subducting slab and overriding plate [e.g., *Zhong and Gurnis*, 1992; *King and Hager*, 1994; *Billen and Hirth*, 2007; *Behounková and Cízková*, 2008]. Despite the limitations, dynamic subduction models significantly improve our understanding of the dynamics of subduction zones including: 1) the effect of trench migration on slab geometry [e.g., *Christensen*, 1996; *Funiciello et al.*, 2003a; *Enns et al.*, 2005], 2) the effect of phase transitions and viscosity contrast across the upper and lower mantle on the vigor of the subduction (whole or layered mantle convection) [e.g., *Christensen and Yuen*, 1984; *Peltier and Solheim*, 1992; *King and Ita*, 1995], 3) back-arc compression/extension and relevant slab deformation [e.g., *Wdowinski and Bock*, 1994; *Pope and Willett*, 1998; *Sobolev and Babeyko*, 2005], 4) slab detachment and ridge subduction [e.g., *Chatelain et al.*, 1992; *Gerya et al.*, 2004; *Burkett and Billen*, 2009; *Mason et al.*, 2010], and 5) the effect of slab strength and viscosity contrast across the upper-lower mantle boundary on geoid and elevation [e.g., *Hager et al.*, 1985; *King and Hager*, 1994; *Chen and King*, 1998; *King*, 2002].

Although the kinematic-dynamic and dynamic subduction models considerably contribute to our understanding of subduction zones, the effect of time-dependence of the subduction parameters and compressibility on the evolution of subduction zones has been rarely evaluated: Steady-state and/or incompressible subduction models have been broadly used. However, the growing evidence indicating time-dependence in subduction zones requires consideration of the time-dependence in the subduction zone models [e.g., *Kay et al.*, 2005; *Sdrolias and Müller*, 2006; *Stepashko*, 2008]. In addition, compressibility resulting from the very high pressures within the mantle requires to consider the mantle

adiabatic gradient and viscous dissipation in the subduction zone models. Throughout this dissertation, I focus on the effect of time-dependence and compressibility on the evolution of subduction zones.

1.4 Summary of Following Chapters

In Chapter 2, I evaluate the effect of compressibility on the thermal and flow structures of subduction zones. This work was published by American Geophysical Union – Lee and King (2009), Effect of mantle compressibility on the thermal and flow structures of the subduction zones, *Geochemistry Geophysics Geosystems*, 10, Q1006, doi:10.1029/2008GC002151. For this study, I formulated 2-D kinematic-dynamic numerical subduction models similar to those that have been used in subduction zone research for the past four decades. In the kinematic-dynamic models, the subducting slab is prescribed as a rigid body subducted at a constant rate and the overriding plate is fixed during the experiment run. The thermal and flow structures in the mantle wedge between the subducting slab and overriding plate are dynamically calculated by excluding the mantle buoyancy which is thought to play a minor role in the calculations. The slab dip and thermal boundary conditions for the subducting slab and mantle wedge are kept constant for the experiment run. Because the subducting rate and slab dip, as well as thermal boundary conditions, are fixed for the experiment run, the thermal and flow structures of the subduction zone models reach to the steady-state. These simplifications and idealizations might be far different than the real evolution of subduction zones but, the effect of compressibility can be evaluated by excluding the effect of the other subduction parameters such as trench migration. The results show that heat created by viscous dissipation thins the thermal boundary layer above the subducting slab and slab temperatures increase when compressibility is considered. However, the thermal and flow structures in the mantle wedge are not considerably affected by compressibility. This study indicates that incompressible mantle convection models could be a good first-order approximation for kinematic-dynamic subduction zone modeling.

In Chapter 3, I discuss the effect of the time-dependent evolution of the convergence rate and slab age on slab melting which contributes to localized high-Mg# andesites in the Aleutian island arc. This work was published by the Geological Society of America – Lee and King (2010), Why are high-Mg# andesites widespread in the western Aleutians? A numerical model approach, *Geology*, v.38, no. 7, p. 583-586, doi: 10.1130/G30714.1. High-Mg# andesites observed in the western Aleutians have been thought to be attributed to melting of very young subducting slab whereas the present-day old subducting slab appears to be too cold to generate slab melting. A recent numerical model shows that melting of the present-day old subducting slab is possible. However, confinement of the high-Mg# andesites to the western Aleutians cannot be correlated with the similar slab age along the trench. Plate reconstruction models show that the convergence rate and slab age have been significantly changed along the Aleutian island arc, which implies the time-dependent evolution of the convergence rate and slab age are important to infer million-year scale arc magmatism in the Aleutians. The results from Chapter 2 show that the influence of compressibility is mostly expressed as viscous dissipation. Therefore, instead of using a fully compressible model described in Chapter 2, I use incompressible subduction models with viscous dissipation. Compared with traditional steady-state slab thermal structure models, the convergence rate and slab age are updated at every time step following the onset of subduction. The results show that the localized distribution of the high-Mg# andesites in the western Aleutians is a consequence of the time-dependent convergence rate and slab age along the Aleutian island arc. This study illustrates that time-dependent subduction parameters such as slab age and convergence rates (i.e. geological history) contribute to the spatial and temporal arc magmatism in subduction zones.

In Chapter 4, I evaluate time-dependent (periodic) slab buckling which develops in the shallow lower mantle and its expression on Earth's surface, periodic changes in the convergence rate of the oceanic lithosphere toward the trench. This work will be submitted to Journal of Geophysical Research published by American Geophysical Union. There is abundant evidence indicating that subduction processes are time-dependent. First, plate reconstruction models show that the spreading and convergence rates are time-dependent, especially, in the plate bounded by subduction zones such as the

Pacific and Nazca plates. Another line of evidence supporting time-dependent subduction is the poor correlation between the slab dip and age. In addition, the alternating eastward and westward arc volcanoes in the Andes have been thought to be attributed to alternating dip of the subducting slab under the arc volcanoes. In order to infer the time-dependent nature of the subducting slab and its expression, 2-D dynamic subduction models are formulated with relevant parameters and rheologies for the mantle and slab. The results show that periodic slab buckling develops through alternating slab shallowing and steepening in the upper mantle and the buckled slab stacks in the shallower lower mantle. The periodic slab buckling results in the periodic convergence rate of the oceanic plate. Despite the complexities of the dynamic subduction models, the period and amplitude of the slab buckling are generally consistent with the scaling laws valid for the buckling behavior of vertically descending fluid. The periodic slab buckling and convergence rate in the modeling calculations explain time-dependent seafloor spreading and convergence rate, and the poor correlation between the slab dip and age. The alternating shallowing and steepening slab is consistent with the alternating eastward and westward migration of the arc volcanoes in the Andes. This study indicates that consideration of time-dependence significantly improves our understanding of subduction zones.

In Chapter 5, I briefly propose to conduct time-dependent 3-D (4-D) subduction experiments where I can evaluate 3-D aspects of the subduction zones as future studies. Because all the experiments described in this thesis are based on 2-D Cartesian models, along-strike variations of the subduction parameters such as oblique convergence and trench geometry can not be included in the models. Therefore, I propose that the following studies of 3-D subduction represent the next logical steps in this research. One study should investigate the effect of the oblique convergence and concave trench geometry in the Aleutian island arc on distribution of high Mg# andesites, which is an improved study described in Chapter 3. A second study should investigate the effect of asymmetric trench roll-back on the slab morphology in the Izu-Bonin-Mariana subduction system. Seismic tomography images show that stagnant slab on the 660 km discontinuity and steeply subducting slab in the Izu-Bonin and the Mariana subduction system, respectively. Plate reconstruction models and numerical models imply that

asymmetric trench roll-back may be responsible for the slab morphology. However, quantitative analysis of the effect of the asymmetric roll-back on the slab morphology can be conducted through time-dependent 3-D subduction experiments. As a first step, the asymmetric trench roll-back is kinematically prescribed with time-dependent convergence rate and slab age, constrained by the relevant plate reconstruction models. Next, dynamically controlled trench roll-back and the effect of the subduction of the low-density plateau on the slab morphology will be tested in the time-dependent 3-D subduction experiments.

References

Allègre, C. J., and D. L. Turcotte (1985), Geodynamic mixing in the mesosphere boundary layer and the origin of oceanic islands, *Geophysical Research Letter*, *12*(4), 207-210.

Atwater, T. (1970), Implications of plate tectonics for the Cenozoic tectonic evolution of western North America, *Geological Society of America Bulletin*, *81*(12), 3513-3536.

Behounková, M., and H. Cízková (2008), Long-wavelength character of subducted slabs in the lower mantle, *Earth and Planetary Science Letters*, *275*(1-2), 43-53.

Billen, M. I. (2008), Modeling the Dynamics of Subducting Slabs, *Annual Review of Earth and Planetary Sciences*, *36*(1), 325-356.

Billen, M. I., and G. Hirth (2007), Rheologic controls on slab dynamics, *Geochemistry Geophysics Geosystems*, *8*(8), Q08012. doi:10.1029/2007gc001597

Blakely, R. J., T. M. Brocher, and R. E. Wells (2005), Subduction-zone magnetic anomalies and implications for hydrated forearc mantle, *Geology*, *33*(6), 445-448.

Burkett, E. R., and M. I. Billen (2009), Dynamics and implications of slab detachment due to ridge-trench collision, *Journal of Geophysical Research*, *114*(B12), B12402.

Chalot-Prat, F., and R. Girbacea (2000), Partial delamination of continental mantle lithosphere, uplift-related crust-mantle decoupling, volcanism and basin formation: a new model for the Pliocene-Quaternary evolution of the southern East-Carpathians, Romania, *Tectonophysics*, *327*(1-2), 83-107.

Chatelain, J. L., P. Molnar, R. Prevot, and B. Isacks (1992), Detachment of part of the downgoing slab and uplift of the new Hebrides (Vanuatu) islands, *Geophysical Research Letters*, *19*(14), 1507-1510.

Chen, J. N., and S. D. King (1998), The influence of temperature and depth dependent viscosity on geoid and topography profiles from models of mantle convection, *Physics of the Earth and Planetary Interiors*, *106*(1-2), 75-92.

Christensen, U. R. (1996), The influence of trench migration on slab penetration into the lower mantle, *Earth and Planetary Science Letters*, *140*(1-4), 27-39.

Christensen, U. R., and D. A. Yuen (1984), The interaction of a subducting lithosphere slab with a chemical or phase-boundary, *Journal of Geophysical Research, 89 (NB6)*, 4389-4402.

Courtillot, V., A. Davaille, J. Besse, and J. Stock (2003), Three distinct types of hotspots in the Earth's mantle, *Earth and Planetary Science Letters*, *205*(3-4), 295-308.

Darwin, G. H. (1898), The Tides and Kindred Phenomena in the Solar System., *Houghton Miffin and Company*, Boston and New York.

Dragert, H., and R. D. Hyndman (1995), Continuous GPS monitorning of elastic strain in the northern Cascadia subduction zone, *Geophysical Research Letter*, *22*(7), 755-758.

Engdahl, E. R., R. van der Hilst, and R. Buland (1998), Global teleseismic earthquake relocation with improved travel times and procedures for depth determination, *Bulletin of the Seismological Society of America*, *88*(3), 722-743.

Enns, A., T. W. Becker, and H. Schmeling (2005), The dynamics of subduction and trench migration for viscosity stratification, *Geophysical Journal International*, *160*(2), 761-775.

Forsyth, D., and S. Uyeda (1975), On the relative importance of the driving forces of plate motion, *Geophysical Journal of the Royal Astronomical Society*, *43*(1), 163-200.

Forte, A. M., and J. X. Mitrovica (1996), New inferences of mantle viscosity from joint inversion of long-wavelength mantle convection and post-glacial rebound data, *Geophysical Research Letters*, *23*(10), 1147-1150.

Fukao, Y., S. Widiyantoro, and M. Obayashi (2001), Stagnant slabs in the upper and lower mantle transition region, *Review of Geophysics*, *39*(3), 291-323.

Funiciello, F., G. Morra, K. Regenauer-Lieb, and D. Giardini (2003a), Dynamics of retreating slabs: 1. Insights from two-dimensional numerical experiments, *Journal of Geophysical Research*, *108*(B4), 2206.

Funiciello, F., C. Faccenna, D. Giardini, and K. Regenauer-Lieb (2003b), Dynamics of retreating slabs: 2. Insights from three-dimensional laboratory experiments, *Journal of Geophysical Research*, *108*(B4), 2207.

Gerya, T. V., and D. A. Yuen (2003), Rayleigh-Taylor instabilities from hydration and melting propel 'cold plumes' at subduction zones, *Earth and Planetary Science Letters*, *212*(1-2), 47-62.

Gerya, T. V., D. A. Yuen, and W. V. Maresch (2004), Thermomechanical modelling of slab detachment, *Earth and Planetary Science Letters*, *226*(1-2), 101-116.

Gorden, R. B. (1967), Thermally activated processes in the Earth: Creep and seismic attenuation, *Geophysical Journal of the Royal Astronomical Society*, *14*, 33-43.

Griggs, D. T. (1939), A theory of mountain-building, *American Journal of Science*, *237*(9), 611-650.

Grove, T. L., N. Chatterjee, S. W. Parman, and E. Médard (2006), The influence of H_2O on mantle wedge melting, *Earth and Planetary Science Letters*, *249*(1-2), 74-89.

Grove, T. L., C. B. Till, E. Lev, N. Chatterjee, and E. Medard (2009), Kinematic variables and water transport control the formation and location of arc volcanoes, *Nature*, *459*(7247), 694-697.

Guillaume, B., J. Martinod, and N. Espurt (2009), Variations of slab dip and overriding plate tectonics during subduction: Insights from analogue modelling, *Tectonophysics*, *463*(1-4), 167-174.

Guillou-Frottier, L., J. Buttles, and P. Olson (1995), Laboratory experiments on the structure of subducted lithosphere, *Earth and Planetary Science Letters*, *133*(1-2), 19-34.

Hager, B. H., and M. A. Richards (1989), Long-wavelength variatios in Earth's geoid – physical models and dynamic implications, *Philosophical Transactions of the Royal Society of London Series A*, *328 (1599)*, 309-327.

Hager, B. H., R. W. Clayton, M. A. Richards, R. P. Comer, and A. M. Dziewonski (1985), Lower mantle heterogeneity, dynamic topography and the geoid, *Nature*, *313*(6003), 541-546.

Hales, A. L. (1936), Convection currents in the Earth, *Monthly Notices of the Royal Astronomical Society*, *3*, 372-379.

Hansen, V. L. (2007), Subduction origin on early Earth: A hypothesis, *Geology*, *35*(12), 1059-1062.

Haskell, N. A. (1935), The motion of a viscous fluid under a surface load, *Physics, 6*, 265-269.

Hess, H. H. (1962), History of ocean basins, In Petrologic Studies - A Volume in Honor of A. F. Buddington, 599-620, Eds. A. Engeln, H. L. James, & B. F. Leonard. *Geological Society of America*, New York.

Hyndman, R. D., and K. Wang (1993), Thermal constraints on the zone of major thrust earthquake failure: The Cascadia subduction zone, *Journal of Geophysical Research, 98*(B2), 2039-2060.

Hyndman, R. D., K. Wang, and M. Yamano (1995), Thermal constraints on the seismogenic portion of the southwestern Japan subduction thrust, *Journal of Geophysical Research*, *100*(B8), 15373-15392.

Isacks, B., and P. Molnar (1971), Distribution of stresses in the descending lithosphere from a global survey of focal-mechanism solutions of mantle earthquakes, *Review of Geophysics*, *9*, 103-174.

Iwamori, H. (1998), Transportation of H_2O and melting in subduction zones, *Earth and Planetary Science Letters*, *160*(1-2), 65-80.

Jarrard, R. D. (1986), Relations among subduction parameters, *Review of Geophysics*, *24*, 217-284.

Jeffreys, H. (1929), The Earth, its Origin, History, and Physical Constitution, *Cambridge Univ. Press, Cambridge (2nd Ed).*

Karason, H., and R. D. van der Hilst (2001), Tomographic imaging of the lowermost mantle with differential times of refracted and diffracted core phases (PKP, P-diff), *Journal of Geophysical Research*, *106*(B4), 6569-6587.

Kawamoto, T., and J. R. Holloway (1997), Melting temperature and partial melt chemistry of H_2O-saturated mantle peridotite to 11 gigapascals, *Science*, *276*(5310), 240-243.

Kay, R. W. (1978), Aleutian magnesian andesites: Melts from subducted Pacific ocean crust, *Journal of Volcanology and Geothermal Research*, *4*(1-2), 117-132.

Kay, S. M., E. Godoy, and A. Kurtz (2005), Episodic arc migration, crustal thickening, subduction erosion, and magmatism in the south-central Andes, *Geological Society of America Bulletin*, *117*(1-2), 67-88.

Kelbert, A., A. Schultz, G. Egbert (2009), Global electromagnetic induction constraints on transition-zone water content variations, *Nature*, 460(7258), 1003-1006

Kelemen, P. B., G. M. Yogodzinski, and D. W. Scholl (2003), Along-strike variation in the Aleutian island arc: Genesis of high Mg# andesite and implications for continental crust, in Eiler, J., ed., Inside the Subduction Factory, *American Geophysical Union*, Washington, D.C., 223-276.

Kellogg, L. H., and S. D. King (1997), The effect of temperature dependent viscosity on the structure of new plumes in the mantle: Results of a finite element model in a spherical, axisymmetric shell, *Earth and Planetary Science Letters*, *148*(1-2), 13-26.

Kendall, J. M., and P. G. Silver (1996), Constraints from seismic anisotropy on the nature of the lowermost mantle, *Nature*, *381*(6581), 409-412.

Kido, Y., M. Kido, and K. Fujioka (2004), Magnetic dipole anomalies as indicators of mantle wedge serpentinization, *Geochemistry Geophysics Geosystems*, *5*(8), Q08J13. doi: 10.1029/2004gc000697

King, S. D. (2002), Geoid and topography over subduction zones: The effect of phase transformations, *Journal of Geophysical Research*, *107*(B1), doi: 10.1029/2000JB000141

King, S. D. (2007), Mantle downwellings and the fate of subducting slabs: Constraints from seismology, geoid topography, geochemistry, and petrology, in Treatise on Geophysics, ed. S. Gerald, *Elsevier*, Amsterdam, 325-370.

King, S. D., and G. Masters (1992), An inversion for radial viscosity structure using seismic tomography, *Geophysical Research Letter*, *19*(15), 1551-1554.

King, S. D., and B. H. Hager (1994), Subducted slabs and the geoid. 1. Numerical experiments with temperature-dependent viscosity, *Journal of Geophysical Research*, *99*(B10), 19843- 19852.

King, S. D., and J. Ita (1995), Effect of slab rheology on mass-transport across a phase-transition boundary, *Journal of Geophysical Research*, *99*(B10), 19843-19852.

King, S. D., A. Raefsky, and B. H. Hager (1990), Conman: vectorizing a finite element code for incompressible two-dimensional convection in the Earth's mantle, *Physics of the Earth and Planetary Interiors*, *59*(3), 195-207.

Lay, T., Q. Williams, and E. J. Garnero (1998), The core-mantle boundary layer and deep Earth dynamics, *Nature*, *392*(6675), 461-468.

Leonard, L. J., R. D. Hyndman, and S. Mazzotti (2004), Coseismic subsidence in the 1700 great Cascadia earthquake: Coastal estimates versus elastic dislocation models, *Geological Society of America Bulletin*, *116*(5-6), 655-670.

Li, C., R. D. van der Hilst, E. R. Engdahl, and S. Burdick (2008), A new global model for P wave speed variations in Earth's mantle, *Geochemistry Geophysics Geosystems*, *9*(5), Q05018. doi: 10.1029/2007gc001806

Mason, R. G. (1958), A magnetic survey of the west coast of the United States between Latitudes 32 and 36 N, longitudes 121 and 128 W., *Geophysical Journal of the Royal Astronomical Society*, *1*, 320-329.

Mason, W. G., L. Moresi, P. G. Betts, and M. S. Miller (2010), Three-dimensional numerical models of the influence of a buoyant oceanic plateau on subduction zones, *Tectonophysics*, *483*(1-2), 71-79.

McKenzie, D., and R. K. O'Nions (1983), Mantle reservoirs and ocean island basalts, *Nature*, *301*(5897), 229-231.

McKenzie, D. P. (1969), Speculations on the consequences and causes of plate motions, *Geophysical Journal of the Royal Astronomical Society*, *18*, 1-32.

McKenzie, D. P., and R. L. Parker (1967), The north Pacific, an example of tectonics on a sphere, *Nature*, *216*, 1276-1280.

Miller, M. S., A. Gorbatov, and B. L. N. Kennett (2005), Heterogeneity within the subducting Pacific slab beneath the Izu-Bonin-Mariana arc: Evidence from tomography using 3D ray tracing inversion techniques, *Earth and Planetary Science Letters*, *235*(1-2), 331-342.

Minear, J. W., and M. N. Toksoz (1970), Thermal regime of a downgoing slab and new global tectonics, *Journal of Geophysical Research*, *75*, 1397-1419.

Moresi, L., and V. Solomatov (1998), Mantle convection with a brittle lithosphere: thoughts on the global tectonic styles of the Earth and Venus, *Geophysical Journal International*, *133*(3), 669-682.

Morgan, W. (1968), Rises, trenches, great faults, and crustal blocks, *Journal of Geophysical Research*, *73*(6), 1959-1982.

Morgan, W. J. (1971), Convection plumes in the lower mantle, *Nature*, *230*(5288), 42-43.

O'Neill, C., L. Moresi, D. Muller, R. Albert, and F. Dufour (2006), Ellipsis 3D: A particle-in-cell finite-element hybrid code for modelling mantle convection and lithospheric deformation, *Computers & Geosciences*, *32*(10), 1769-1779.

Oleskevich, D. A., R. D. Hyndman, and K. Wang (1999), The updip and downdip limits to great subduction earthquakes: Thermal and structural models of Cascadia, south Alaska, SW Japan, and Chile, *Journal of Geophysical Research*, *104*(B7), 14965-14991.

Oxburgh, E. R., and D. L. Turcotte (1968), Problem of high heat flow and volcanism associated with zones of descending mantle convective flow, *Nature*, *218*, 1041-1043.

Parmentier, E., D. Turcotte, and K. Torrance (1976), Studies of finite amplitude non-Newtonian thermal convection with application to convection in the Earth's mantle, *Journal of Geophysical Research*, *81*(11), 1839-1846.

Peacock, S. M. (1996), Thermal and petrological structure of subduction zones (overview), In Subduction, Top to Bottom, *Ed. Bebout, G. E., et al.*, Washington, D.C., *American Geophysical Union*, 119-134.

Peacock, S. M., and K. Wang (1999), Seismic consequences of warm versus cool subduction metamorphism: Examples from southwest and northeast Japan, *Science*, *286*(5441), 937-939.

Peacock, S. M., T. Rushmer, and A. B. Thompson (1994), Partial melting of subducting oceanic crust, *Earth and Planetary Science Letters*, *121*(1-2), 227-244.

Pekeris, C. L. (1935), Thermal convection in the interior of the Earth, *Monthly Notices of the Royal Astronomical Society*, *3*, 343-367.

Peltier, W. R., and L. P. Solheim (1992), Mantle phase transitions and layered chaotic convection, *Geophysical Research Letter*, *19*(3), 321-324.

Pope, D. C., and S. D. Willett (1998), Thermal-mechanical model for crustal thickening in the central Andes driven by ablative subduction, *Geology*, *26*(6), 511-514.

Ren, Y., E. Stutzmann, R. D. van der Hilst, and J. Besse (2007), Understanding seismic heterogeneities in the lower mantle beneath the Americas from seismic tomography and plate tectonic history, *Journal of Geophysical Research*, *112*(B1), B01302.

Richter, F. M. (1973), Dynamical models for sea floor spreading, *Review of Geophysics*, *11*(2), 223-287.

Rogers, G., and H. Dragert (2003), Episodic tremor and slip on the Cascadia subduction zone: The chatter of silent slip, *Science*, *300*(5627), 1942-1943.

Schubert, G., and A. Zebib (1980), Thermal-convection of an internally heated infinite prandtl number fluid in a sperical-shell, *Geophysical and Astrophysical Fluid Dynamics*, *15*(1-2), 65-90.

Schubert, G., D. L. Turcotte, and P. Olson (2001), Mantle convection in the Earth and planets, *Cambridge University Press*, Cambridge.

Sdrolias, M., and R. D. Müller (2006), Controls on back-arc basin formation, *Geochemistry Geophysics Geosystems*, *7*(Q04016), doi: 10.1029/2005GC001090

Sleep, N. H. (1992), Hotspot volcanism and mantle plumes, *Annual Review of Earth and Planetary Sciences*, *20*, 19-43.

Sobolev, S. V., and A. Y. Babeyko (2005), What drives orogeny in the Andes?, *Geology*, *33*(8), 617-620.

Stepashko, A. (2008), Spreading cycles in the Pacific Ocean, *Oceanology*, *48*(3), 401-408.

Stern, R. J. (2002), Subduction zones, *Review of Geophysics*, *40*(4), 1012.

Syracuse, E. M., and G. A. Abers (2006), Global compilation of variations in slab depth beneath arc volcanoes and implications, *Geochemistry Geophysics Geosystems*, *7*(Q05017), doi:10.1029/2005GC001045

Tan, E., and M. Gurnis (2007), Compressible thermochemical convection and application to lower mantle structures, *Journal of Geophysical Research*, *112*(B6).

Ulmer, P. (2001), Partial melting in the mantle wedge -- the role of H_2O in the genesis of mantle-derived 'arc-related' magmas, *Physics of the Earth and Planetary Interiors*, *127*(1-4), 215-232.

van Keken, P. E., B. Kiefer, and S. M. Peacock (2002), High-resolution models of subduction zones: Implications for mineral dehydration reactions and the transport of water into the deep mantle, *Geochemistry Geophysics Geosystems*, 3, doi: 10.1029/2001GC000256

Wdowinski, S., and Y. Bock (1994), The evolution of deformation and topography of high elevated plateaus 1. Model, numerical analysis, and general results, *Journal of Geohphysical Research*, *99*(B4), 7103-7119.

Wegener, A. (1924), The Origin of Continents and Oceans, *E. P. Dutton, New York*, 212, Translated from 3rd German ed by J.G. A Skerl.

Wilson, J. T. (1963), Hypothesis of Earth's behavior, *Nature*, *198*, 925-929.

Yogodzinski, G. M., and P. B. Kelemen (1998), Slab melting in the Aleutians: implications of an ion probe study of clinopyroxene in primitive adakite and basalt, *Earth and Planetary Science Letters*, *158*(1-2), 53-65.

Zegers, T. E., and P. E. van Keken (2001), Middle Archean continent formation by crustal delamination, *Geology*, *29*(12), 1083-1086.

Zhong, S. J., and M. Gurnis (1992), Viscous-flow model of a subduction zone with a faulted lithosphere – Long and short wavelength topography, gravity and geoid, *Geophysical Research Letters*, *19*(18), 1891-1894.

Zhong, S. J., M. T. Zuber, L. Moresi, and M. Gurnis (2000), Role of temperature-dependent viscosity and surface plates in spherical shell models of mantle convection, *Journal of Geophysical Research*, *105*(B5), 11063-11082.

Chapter 2

Effect of mantle compressibility on the thermal and flow structures of the subduction zones *

Abstract

The heat generated by viscous dissipation is consistently evaluated using a 2-D compressible subduction model with variations of mantle rheology (constant as well as pressure and temperature dependent viscosity), dip, age, velocity of the subducting slab. For comparison, we also conduct 2-D incompressible subduction calculations with the same conditions and parameters used in the compressible formulation. The effect of compressibility on the thermal and flow structures of the subduction zones is relatively small and concentrated along the base of the mantle wedge; temperature differences < 100 ˚C and differences in kinematic energy of the mantle wedge < 1 % between compressible and incompressible models. Mantle rheology has a stronger effect on thermal and flow structures than mantle compressibility as well as the variations of dip, age and velocity of the subducting slab. The heat from viscous dissipation in the compressible model increases the slab temperatures over the incompressible model (< 70 ˚C), as a result of additional conduction across the slab surface (constant viscosity) and thinning of the thermal boundary layer caused by viscosity reduction (pressure and temperature dependent viscosity).

Keywords: subduction zone, compressible model, viscous dissipation

Lee, C. and S. D. King (2009), Effect of mantle compressibility on the thermal and flow structures of the subduction zones, *Geochemistry Geophysics Geosystems*, 10, Q1006, doi:10.1029/2008GC002151. To view the published open abstract, go to http://dx.doi.org and enter the DOI.

2.1 Introduction

Subduction zones are the sites where active arc volcanoes, orogenic processes, and destructive earthquakes from shallow to deep are observed. The mantle wedge between the slab and overlying lithosphere is expected to be cooler than that of the ambient upper mantle due to a cold subducting slab. However, both geochemistry of arc magmas and surface heat flow data in the arc and backarc seem to require high temperatures in the mantle wedge [*Currie et al.*, 2004; *Currie and Hyndman*, 2006; *Furukawa and Uyeda*, 1989; *Kelemen et al.*, 2003; *Peacock and Hyndman*, 1999; *Peacock*, 2003; *Peacock et al.*, 2005; *Ulmer*, 2001]. To reconcile these seemingly contradictory observations, previous studies have suggested induced hot mantle from deep mantle to the corner of the mantle wedge by viscous coupling between the subducting slab and mantle wedge or, small-scale mantle convection below the backarc [*Currie et al.*, 2004; *Kelemen et al.*, 2003; *Peacock et al.*, 2005; *van Keken et al.*, 2002]. Although the heat generated by frictional shear heating, viscous dissipation, exothermic metamorphic reactions and radiogenic heat production have been suggested as significant heat sources in the mantle wedge, they are insufficient to reconcile the geochemical and heat flow observations [*Iwamori*, 1997; *McKenzie and Schlater*, 1968; *Minear and Toksoz*, 1970; *Oxburgh and Turcotte*, 1968; *Peacock et al.*, 1994; *Peacock*, 1996].

McKenzie [1969] estimated the heat generated by viscous dissipation in the mantle wedge by using an analytic corner flow solution; shear heating concentrates along the bottom of the overlying lithosphere and interface between the subducting slab and mantle wedge. With radiogenic heat production in the overlying lithosphere and induced hot mantle flow under the lithosphere, the heat caused by viscous dissipation has been suggested a contribution to the high surface heat flow in the backarc. Because the analytic corner flow solution is driven by following the assumptions of an incompressible and constant viscosity fluid, it is unknown how much compressibility as well as temperature and pressure dependent rheology affects the thermal and flow structures of the subduction zones. Although *Kneller et al.* [2007] consider viscous dissipation in their subduction model with

pressure and temperature dependent viscosity, they also use an incompressible fluid model and the effect of compressibility is not quantitatively evaluated. To consider viscous dissipation and the mantle adiabat due to the mantle compressibility consistently, compressible fluid models [e.g., *Jarvis and McKenzie*, 1980] are essential but, studies that use a compressible fluid model are rare [*Ita and King*, 1994; 1998; *Leng and Zhong*, 2008; *Zhang and Yuen*, 1996]. As a result, most studies of subduction zones are based on incompressible fluid models and the differences in the thermal and flow structures of the subduction zones between incompressible and compressible fluid models have not been quantitatively evaluated. In this study, we quantitatively evaluate the differences in the thermal and flow structures of the subduction zones using incompressible and compressible fluid models.

With the consideration of compressibility, we choose a 2-D coupled kinematic-dynamic model in which the subducting slab velocity and overlying lithosphere are kinematically prescribed and temperature and flow in the mantle wedge are solved dynamically. Ultimately, a 3-D fully-dynamic model considering slab buoyancy and deformation is needed for subduction zone studies. However, convection calculations must overcome difficulties in generating asymmetric subducting slabs [e.g., *Bercovici*, 2003; *King*, 2001]. Although the coupled kinematic-dynamic model can not be used to study the slab dynamics, the fixed and rigid slab geometry in the coupled model is suitable for evaluating the effects of variations of dip, age, and velocity of the subducting slab on the thermal and flow structures of the subduction zones [*van Keken et al.*, 2008]. Recently, decoupling conditions between the subducting slab and mantle wedge have been studied because the conditions control the thermal and flow structures of the corner of the mantle wedge [*Conder*, 2005; *Kneller et al.*, 2007; *Wada et al.*, 2008]. In this study, we use partially and fully coupled zones to evaluate the effect of decoupling conditions on the thermal and flow structure of the subduction zones.

Mantle rheology has been studied through diverse geophysical methods including: analyses of postglacial rebound [*Heskell*, 1935; 1936; *Karato and Wu*, 1993; *Mitrovica*, 1996; *Wu and Yuen*, 1991; *Wu*, 1998], analyses of geoid anomalies [*Hager and Richards*, 1989; *King and Masters*, 1992; *Ricard and Wuming*, 1991; *Richards and Hager*, 1984] and laboratory experiments using mantle minerals [*Hirth and*

Kohlstedt, 1995; *Karato and Wu*, 1993; *Mei et al.*, 2002]. From previous studies, the mantle rheology is controlled by pressure, temperature and strain rate and can be expressed by two major flow mechanisms: diffusion (Newtonian) and dislocation (non-Newtonian or power-law) creep. However, it has been the subject of debate which flow mechanism is predominant in the upper and lower mantle. *Karato and Wu* [1993] and *Wu* [1998] evaluated postglacial rebound data and suggested that the predominant rheology of the upper mantle is dislocation creep and lower mantle is diffusion creep. *van Hunen et al.* [2005] also suggested that the predominant rheology for the upper mantle is dislocation creep based on mid-ocean ridge spreading studies. Distinctive seismic anisotropy implies dislocation creep as the predominant flow mechanism in the upper mantle [*Karato*, 1992; *Long and Silver*, 2008; *Savage*, 1999; *Silver*, 1996]. However, the opposite evaluation implying the predominance of diffusion creep for the upper mantle and dislocation creep for the lower mantle has also been reported [*Wu*, 1999]. It has been suggested that the effective viscosity of the upper mantle is an expression of lower viscosity either diffusion or dislocation creep with respect to temperature and pressure conditions which differ with geological setting [*Ranalli*, 2001]. In this study, we evaluate the predominant rheology in the mantle wedge using diffusion and dislocation creep as well as constant viscosity used in early subduction models.

2.2 Numerical model

2.2.1 Governing equations and numerical methods

Mantle materials deform as a very viscous fluid under high temperature conditions and geological time scales. This justifies the use of the governing equations for compressible laminar fluid flow. In addition, mantle conditions satisfies special assumptions; 1) the rate of density (volume) variation of mantle materials with time is negligible and 2) because acceleration of mantle flow is very slow compared with stress differences, acceleration and momentum can be also neglected. In other words, mantle materials can be considered as a fluid satisfying the conditions of very low Mach number (~ 0)

and infinite Prandtl number (> 10^{22}). By applying the assumptions to the equations of fluid motion [e.g., *Jarvis and McKenzie*, 1980], the governing equations relevant to compressible mantle deformation are;

$$0 = \nabla \cdot (\rho \vec{v}) \qquad \text{- } \textit{continuity equation} \qquad (1)$$

$$0 = -\nabla P + \rho \vec{g} + \nabla \cdot \underline{\tau} \qquad \text{- } \textit{momentum equation} \qquad (2)$$

$$\rho C_p \frac{DT}{Dt} - \alpha \frac{DP}{Dt} = \nabla \cdot (k \nabla T) + \phi + \rho H \qquad \text{- } \textit{energy equation} \qquad (3)$$

where ρ is the density, t is the time, $\vec{v}$ is the velocity, P is the pressure, $\vec{g}$ is the gravitational acceleration, $\underline{\tau}$ is the deviatoric stress tensor, C_p is the heat capacity under constant pressure, α is thermal expansivity, T is the temperature, k is the thermal conductivity, ϕ is the viscous dissipation and H is the rate of radiogenic heat production.

In compressible fluids, compression and expansion of fluids generate heat through viscous dissipation [*Schubert et al.*, 2001]

$$\phi = k_B \dot{\varepsilon}_{ii}^{\,2} + 2\eta \left(\frac{1}{2} \dot{\varepsilon}_{ij} - \frac{1}{3} \dot{\varepsilon}_{kk} \delta_{ij} \right)^2 \qquad \text{- } \textit{viscous dissipation} \qquad (4)$$

where η is the shear viscosity, k_B is the bulk viscosity, $\dot{\varepsilon}$ is the strain rate tensor, δ_{ij} is the Kronecker delta. k_B is neglected (the Stokes assumption) here because volume changes of the mantle occur over millions of years and relatively unimportant. From equation 4, higher viscosity and larger strain rate generate more heat energy.

If the mantle is motionless and chemically homogeneous, density, temperature and pressure increase with depth only due to adiabatic compression; this is referred to as the reference state. However, perturbations of density, temperature and pressure from the reference state are created during mantle evolution and the perturbations need to be considered. By linearly summing the reference state and perturbations, the equations of state for mantle density, temperature and pressure can be described below;

(5) *density, temperature and pressure for compressible mantle deformation*

$$\rho = \bar{\rho}(\bar{P}, \bar{T}) + \rho'(P', T')$$
$$T = \bar{T} + T'$$
$$P = \bar{P} + P'$$

where the overbar and prime mean the reference state and perturbation from the reference state, respectively.

Density perturbation (ρ') is a function of dynamic pressure (P') and temperature perturbation (T'). For the reference density, we use the Adams-Williamson equation based on the assumption of chemically homogeneous and isentropic mantle;

(6) *Adams-Williamson equation*

$$\bar{\rho} = \rho_0 \exp(\frac{d}{H_T \Gamma})$$

where ρ_0 is the top layer density of the mantle and *d* is the depth. The temperature scale height of compressible mantle (H_T) and the Grüneisen's parameter (Γ) are defined below;

(7) *temperature scale height of compressible mantle*

$$H_T = \frac{C_p}{g\alpha}$$

(8) *Grüneisen's parameter*

$$\Gamma = \frac{\alpha K_s}{\rho C_p}$$

where K_s is the isentropic modulus of bulk compressibility, respectively. Because C_p, α and K_s are not constants under mantle condition, the scale height and Grüneisen's parameter may not be constants [*Anderson et al.*, 1992; *Anderson*, 1995; *Kittel*, 1956; *Stixrude and Lithgow-Bertelloni*, 2005]. However, previous studies [*Anderson*, 2000, and references therein] suggest that the scale height and Grüneisen's parameter may not vary greatly, especially over the upper mantle so we assume the scale height and Grüneisen's parameter constants having values of 6.12×10^6 m and 1.1, respectively. With the assumption

of constant gravitational acceleration and ignoring phase transitions, the adiabatic temperature distribution ($\overline{T}$) and lithostatic pressure ($\overline{P}$) are defined below;

(9) *adiabatic temperature distribution*

$$\overline{T} = T_{surface} \exp(\frac{\alpha g d}{C_p})$$

(10) *lithostatic pressure of the adiabatically compressed mantle*

$$\overline{P} = \rho_c g_0 H_T \Gamma \left(\exp(\frac{d}{H_T \Gamma}) - 1 \right)$$

where $T_{surface}$ is the surface temperature at the top of the fluid. Density perturbations (ρ', mantle buoyancy) due to temperature perturbations (T') and dynamic pressure (P') in the momentum equation are the driving forces for mantle convection. When temperature perturbations and dynamic pressure in the continuity and energy equations are neglected, the governing equations above are reduced to the Anelastic Liquid Approximation (ALA, hereafter). [*Jarvis and McKenzie*, 1980; *Leng and Zhong*, 2008]. We neglect the buoyancy term in the momentum equation because convection in the mantle wedge thought to be primarily induced by viscous coupling between the subducting slab and mantle wedge [e.g., *Currie et al.*, 2004; *Peacock*, 1991; *van Keken et al.*, 2002]. Therefore, there is no difference between the ALA and Truncated Anelastic Liquid Approximation (TALA, hereafter) which neglects the density perturbations due to dynamic pressure in the momentum equation. Finally, the governing equations for the compressible mantle convection used in this study are reduced below.

$$0 = \nabla \cdot (\overline{\rho} \vec{v}) \qquad \text{- } \textit{continuity equation} \qquad (11)$$

$$0 = -\nabla P^{'} + \nabla \cdot \underline{\tau} \qquad \text{- } \textit{momentum equation} \qquad (12)$$

$$\overline{\rho} C_p \frac{DT}{Dt} - \alpha \frac{D\overline{P}}{Dt} = \nabla \cdot (k \nabla T) + \phi + \overline{\rho} H \qquad \text{- } \textit{energy equation} \qquad (13)$$

Because the ALA and TALA are the same for the induced mantle convection model, we use the ALA to indicate the compressible convection model instead of using the TALA. When we assume that

the density is a constant through the whole domain, the governing equations are reduced to those for incompressible fluid flow, the Boussinesq approximation (BA, hereafter) which has been used in most of the previous subduction zone studies.

The finite element code, ConMan [*King et al.*, 1990] based on 2-D Cartesian coordinate system (plain strain), infinite Prandtl number approximation and incompressible fluid approximation (BA) has been modified to solve the governing equations for compressible mantle deformation with the equations of state and parameters described above. ConMan solves the continuity and momentum equations simultaneously using a penalty method formulation [*Hughes*, 1987]. To solve the energy equation, the method of Streamline Upwind Petrov-Galerkin (SUPG) is used [*Hughes and Brooks*, 1979].

We use 300 by 200 four-node quadrilateral elements (same elements through the domain) with an explicit time solver for solving the energy equation. Also, we use 600 by 400 element meshes to evaluate mesh dependence of our numerical experiments (see Appendix). Because we change the dip of the subducting slab by changing the width of the box, laterally longer and shorter rectangular elements are used for the experiments using the dips of 30 and 60 degrees, respectively. To attain convergence, we conduct every experiment for 300 Myr. We also use the Picard solver but, the Picard solver does not converge in some experiments using pressure and temperature dependent viscosity without a special modification [*Kneller et al.*, 2007]. For comparison, we conduct the BA experiments using the same parameters used in the ALA experiments.

2.2.2 Model geometry

In this study, we formulate a 2-D numerical subduction model consisting of a prescribed subducting slab, a 50 km thick overlying rigid lid (lithosphere) and the mantle wedge between the slab and lid (Figure 1). Because the main purpose of this study is to evaluate the effect of the mantle compressibility on the thermal and flow structures of the subduction zones, geometry of the subduction model here is arbitrary and simplified. Similar numerical models have been used in previous studies [e.g., *Currie et al.*, 2004; *Davies and Stevenson*, 1992; *Iwamori*, 1998; *Kneller et al.*, 2007; *Peacock*, 1990;

1991; *Peacock et al.*, 1994; *Peacock and Hyndman*, 1999; *van Keken et al.*, 2002; 2008]. The left top of the box corresponds to the trench where subduction of the slab starts. For the geometry of the subducting slab, we divide the slab into two parts; a curving slab to 50 km depth and a straight slab from 50 km to 400 km depth. For the slab geometry to 50 km depth, we use an ellipsoidal curve where gradient changes gradually from 0 degree at the trench to the dip of the straight slab (45 degrees in Figure 1) at the tip of the mantle wedge. Because we vary the dip of the straight slab, considering the dips of 30, 45 and 60 degrees by changing the ratio of depth (400 km fixed) to widths of the boxes as $1:3\sqrt{3}/2$, 1:3/2 and $1:\sqrt{3}/2$, respectively, the gradient of the curving slab to 50 km depth is also changed with respect to the dips. We vary the ages of the subducting slab as 100, 130 and 180 Myr old by using the half-space cooling model. Distribution of radiogenic heat production is different with respect to lithology and depth; continental lithosphere usually has higher heat production (granite, ~ 10^{-9} J/kg·s) and oceanic lithosphere has relatively lower heat production (basalt, ~ 10^{-11} J/kg·s) [*Schubert et al.*, 2001]. For simplicity, a uniform radiogenic heat production of 3×10^{-10} J/kg·s is implemented for the upper 20 km depth in the slab and lid. Except for the upper lithosphere, no radiogenic heat production is assumed in the whole domain. 3, 5 and 10 cm/year are used for the velocities of the subducting slab.

Although the surface of the subducting slab is expressed with an ellipsoidal curve, the curve is approximated as a step-like surface by selecting the closest nodal points but below the ellipsoidal curve due to the use of the quadrilateral elements in this study. As a result, the surface consists of laterally extended flat surfaces along the nodal points at certain depths rather than a smooth curve; from the trench to 48 km distance (2 km depth), 50 to 68 km (4 km depth), 70 to 82 km (6 km depth) and so on. Surface heat flow is calculated at an element level by considering the convection and conduction in the top elements between the nodal points prescribed at the 0 km (top of the box) and 2 km depth. Therefore, the surface heat flow from the trench to 48 km distance is reduced by the top of the subducting slab (2 km depth) which removes the heat of the top elements. Except for this region, surface heat flow is calculated by considering only conduction in the top elements. This is expressed by the decreases in the surface heat

flow from the trench to 48 km distance; the heat flow jump occurs along the region from 50 to 70 km distance from the trench (Figure 1a and 1b). As the slab surface becomes deeper, the effect of calculation errors on the surface heat flow becomes smaller. In addition, the surface of the slab below 50 km depth cuts the four-node elements diagonally. Because viscous dissipation is calculated at an element level using finite element integration, there is a numerical issue in the calculation of viscous dissipation for the elements consisting of half rigid (slab) and half fluid (wedge) bodies. Therefore, we neglect the elements that are cut diagonally by the surface of the slab in the calculation of viscous dissipation and the effect of half rigid and fluid elements is discussed later. This difficulty in the calculation of viscous dissipation can be minimized or overcome through the introduction of non-uniform or uniform unstructured or, adaptive meshes [e.g., *Davies et al.,* in press; *Kneller et al.,* 2005; *Wada et al.,* 2008].

For the temperature boundary conditions, many experiments have used a constant temperature below a specific depth for the subducting slab and inflow/outflow boundary in the mantle wedge [e.g., *Currie et al.,* 2004; *Kneller et al.,* 2005; *van Keken et al.,* 2002]. However, mantle temperature increases with depth due to compression, so we simply extend the half-space cooling model down to 400 km depth along the left and right sides of the box by satisfying the fixed bottom temperature of 1550 ˚C [*Ita and Stixrude,* 1992]. Therefore, the temperature profile along the subducting side (left side of the box in Figure 1) is prescribed by using the half-space cooling model corresponding to 100, 130 and 180 Myr old lithosphere. The temperature profile along the inflow/outflow boundary of the mantle wedge is prescribed by using the half-space cooling model corresponding to 130 Myr old lithosphere. The temperature of the top surface of the box is fixed as 0 ˚C (273 K).

A no-slip boundary condition is implemented at the bottom of the overlying rigid lid. A stress-free boundary condition is implemented along the inflow/outflow boundary of the mantle wedge. The mantle below the subducting slab is assumed to be fully coupled to the slab; mantle velocity below the slab is the same as that of the slab. This assumption is arbitrary but, the subducting slab transfers heat slowly through conduction so this assumption does not affect the thermal and flow structures of the mantle wedge significantly [*Kneller et al.,* 2005]. To represent shear localization between the subducting

slab and mantle wedge, a partially coupled zone is prescribed along the slab surface from the tip of the mantle wedge (50 km depth) to 100 km depth. Various decoupling conditions have been used in previous studies [e.g., *Abers et al.*, 2006; *Conder*, 2005; *Kneller et al.*, 2005; 2007; *Wada et al.*, 2008] and we prescribe a linear velocity ramp from 10 % at the tip to the full velocity (100 %) at 100 km depth on the slab surface (Figure 1). Frictional shear heating along the surface of the subducting slab (seismogenic zone) may play an important role in increasing the slab and wedge temperature and arbitrarily considered in previous subduction models [e.g., *Peacock*, 1996] but, the shear heating along the seismogenic zone is neglected here. Shear heating on the surface of the subducting slab is considered through viscous dissipation instead of using arbitrarily implemented shear heating.

2.2.3 Mantle rheology

Because of diverse mantle mineralogy and the effects of hydration/dehydration and partial melting on mantle viscosity, the viscosity of the mantle wedge is poorly constrained. However, geoid anomalies, electrical conductivity, seismic tomography and laboratory experiments suggest that the viscosity of the mantle wedge is significantly lower than that of primitive (dry) upper mantle because of hydration and/or partial melting caused by free water dehydrated from the subducting slab, especially, oceanic crust and overlying sediments [*Billen and Gurnis*, 2001, and references therein]. Also, geophysical and geological evidence suggests the presence of serpentinite in the corner of the mantle wedge and olivine as the major upper mantle mineral to the 410 km transition zone [*Brocher et al.*, 2003; *Hyndman and Peacock*, 2003; *Reynard et al.*, 2007; *Schmidt and Poli*, 1998; *Ulmer and Trommsdorff*, 1995]. Based on these findings, we assume that serpentinite exists to 70 km depth and wet olivine exists to 150 km depth in the mantle wedge, which is called the low viscosity zone hereafter. Compared with the sharp viscosity transition between serpentinite and wet olivine zones, we use a linear viscosity transition zone to represent the gradual termination of dehydration of the subducting slab. The transition zone is prescribed as a region extending from the bottom of the overlying lid to the top of the slab where

the bottom of the region extends to the slab surface from 150 km (left-bottom corner) to 200 km depth (right-bottom corner) (Figure 1).

In many numerical experiments, constant viscosity or diffusion creep of dry/wet olivine has been used for the mantle rheology [e.g., *Davies and Stevenson*, 1992; *Honda and Saito*, 2003; *Iwamori*, 1998; *Kincaid and Sacks*, 1997; *McKenzie*, 1969; *Peacock*, 1996]. However, laboratory as well as numerical experiments and seismic anisotropy show that diverse flow mechanisms such as dislocation and Peierls creep could be dominating flow mechanisms with respect to pressure, temperature and strain rate conditions in the upper mantle [*Hirth and Kohlstedt*, 1995; *Kameyama et al.*, 1999; *Kneller et al.*, 2005; *Long and Silver*, 2008; *van Hunen et al.*, 2005]. Therefore, we consider two different mantle rheologies; constant viscosity and composite viscosity of diffusion and dislocation creep as an effective viscosity in the upper mantle. The composite viscosity is expressed by a harmonic average of the viscosities calculated from diffusion and dislocation creep, respectively [e.g., *Kneller et al.*, 2005; 2007];

(14) *diffusion creep (dry olivine)*

$$\eta_{diff} = A_{diff}^{-1} d_g^{\ m} \exp[\frac{E_{diff} + PV_{diff}}{RT}]$$

(15) *dislocation creep (dry olivine)*

$$\eta_{disloc} = A_{disloc}^{-1/n} \exp[\frac{E_{disloc} + PV_{disloc}}{nRT}] \dot{\varepsilon}_s^{\ 1-n/n}$$

(16) *composite viscosity of diffusion and dislocation creep*

$$\eta_{comp} = \left(\frac{1}{\eta_{diff}} + \frac{1}{\eta_{disloc}} \right)^{-1}$$

where $\dot{\varepsilon}_s$ is the square root of the second invariant of strain rate tensor and the parameters related to diffusion and dislocation creep are described in Table 1 and 2. For composite viscosity, effective viscosity is controlled by the lower viscosity between diffusion and dislocation creep.

For the viscosity of wet olivine, a viscosity reduction number of 0.05 is multiplied to the viscosity of dry olivine as a first-order approximation because viscosity of wet olivine is approximately 5 % of that of dry olivine under temperature, pressure and strain rate of the upper mantle [*Honda and Saito*, 2003]. The viscosity of serpentinite is poorly constrained due to rare data from laboratory experiments [*Hilairet et al.*, 2007]. However, aseismicity of the serpentinite zone even at very low temperature conditions (< ~ 700 ˚C) suggests very low viscosity [*Brocher et al.*, 2003]. Therefore, we multiply a viscosity reduction number of 0.0005 to the viscosity of dry olivine to represent the very low viscosity of serpentinite. For the constant viscosity experiments, we use fixed viscosities of 3.0×10^{20}, 1.5×10^{19} and 1.5×10^{17} Pa·s for dry, wet and serpentinite zones, respectively, by using the viscosity reduction numbers above.

2.3 Results

2.3.1 Effects of the mantle rheology

As described above, we consider variations of dip, age and velocity of the subducting slab. For simplicity, we describe here the BA and ALA experiments using the dip of 45 degrees, 130 Myr old lithosphere and velocity of 5 cm/year with constant and composite viscosity. The results of other experiments where we vary dip, age and velocity of the subducting slab are summarized later. Figure 2 shows surface heat flow, temperature and flow in the mantle wedge of the BA and ALA experiments using constant and composite viscosity. In general, weak flow and low temperature field develop in the corner of the mantle wedge in the BA and ALA experiments using constant viscosity, consistent with previous BA studies [*Currie et al.*, 2004; *van Keken et al.*, 2002]. In the BA and ALA experiments using constant viscosity, an isolated roll-like convection develops in the corner, similar to other studies using a low viscosity zone in the corner [*Honda and Saito*, 2003]. As a result, hot mantle in the deeper mantle wedge does not reach the corner and, the surface heat flow in the forearc is much lower than observations. The temperature (< ~ 700 ˚C) in the corner is in the serpentinite stability field [*Ulmer and Trommsdorff*, 1995].

In contrast to the experiments using constant viscosity, the BA and ALA experiments using composite viscosity produce strong corner flow that induces hot mantle to the corner. In this case, the low viscosity zone does not isolate the corner from the hot mantle in the deeper wedge. The corner temperatures are much higher (> 1000 ˚C) than those in the experiments using constant viscosity, consistent with previous studies [*Currie et al.*, 2004; *van Keken et al.*, 2002]. Due to higher corner temperatures, the surface heat flow is higher but, still low compared with the observed surface heat flow data. Because our models do not consider magma generation in the mantle wedge and overlying lithosphere, and lithosphere thinning [*Arcay et al.*, 2005; *Currie et al.*, 2008], the surface heat flow might be underestimated in our models. Higher corner temperatures restrict the serpentinite stability field to a small corner of the mantle wedge and the peak of surface heat flow advances toward the trench compared with the surface heat flow data. As observed in previous studies, a very thick stagnant lid (thermal lithosphere) develops in the overlying plate above the mantle wedge in both BA and ALA experiments using composite viscosity and this leads to much lower surface heat flow in the backarc [*Currie et al.*, 2004; *van Keken et al.*, 2002; 2008].

2.3.2 Effects of the mantle compressibility

The small differences in the surface heat flow between the BA and ALA experiments imply negligible differences in the shallow thermal structure of the mantle wedge because the bottom temperature of the overlying lithosphere (conductive lid) controls the surface heat flow (Figure 2a and 2b). As illustrated in Figure 2, the thermal and flow structures between the BA and ALA experiments are similar each other; temperature differences are < 100 ˚C (mostly observed at the base of the mantle wedge and subducting slab) and differences in kinematic energy of the mantle wedge are < 1 % between the BA and ALA results. There is a more significant difference between the constant and composite viscosity results than between the BA and ALA results; however, differences are observed in temperature of the base of the mantle wedge and subducting slab between the BA and ALA experiments. Figure 3 shows pressure (depth) versus temperature paths for the top of the subducting slab corresponding to the BA and

ALA experiments shown in Figure 2 using constant and composite viscosity. In general, the ALA experiments produce higher temperatures than the BA experiments; ~ 17.67 ˚C (constant viscosity) and ~ 26.35 ˚C (composite viscosity) at 150 km depth. The differences in temperature increase with depth; ~ 66.19 ˚C (constant viscosity) and ~ 69.74 ˚C (composite viscosity) at 400 km depth, as expected due to the greater influence of compressibility. Because the slab is heated by conduction across the slab surface, higher temperature of the slab implies a stronger thermal gradient and hotter mantle temperatures above the slab surface. The mechanism generating a stronger thermal gradient for constant and composite viscosity in the ALA experiments differs. Figure 4 shows that the viscosity structures of the mantle wedge in the BA and ALA experiments using composite viscosity are similar, except that a stronger thermal gradient – thinner thermal boundary layer – develops above the slab surface in the ALA experiments. The heat generated by viscous dissipation in the low viscosity zone is relatively small ($< 10^{-10}$ J/kg·s except for very top of the slab, Figure 5b) so increases in temperature are < 30 ˚C. However, the composite viscosity is sensitive to temperature variation and is reduced by a factor of ~ 10 above the slab surface in the low viscosity zone (Figure 4c). As a result of the reduced viscosity, hot mantle from deeper in the mantle wedge reaches closer to the slab surface; hot and low viscosity mantle can be induced along the slab surface and thins the thermal boundary layer above the slab surface. Therefore, a thinner and less viscous thermal boundary layer develops above the slab surface in the ALA experiments. The temperature jump around 70 km depth in the ALA experiments using composite viscosity is consistent with the region of relatively stronger viscous dissipation above the slab surface showing that the corner flow reaches closer to the slab surface as a result of the viscosity reduction (Figure 3 and 5b).

The strong thermal gradient associated with the viscosity reduction in the ALA experiments using constant viscosity differs from that in the ALA experiments using composite viscosity. In the constant viscosity case, the strong gradient is related to the additional heat conduction driven by increase in temperature of the mantle wedge due to the heat generated by viscous dissipation. Because viscosity in the ALA experiments using constant viscosity is independent of temperature and flow, the thermal gradient that is developed by viscosity reduction is not observed. Therefore, the thermal gradient above

the subducting slab is affected by the additional heat generated by viscous dissipation through out the mantle wedge. The heat generated by viscous dissipation above the subducting slab in the ALA experiments using constant viscosity is comparable to those using composite viscosity except for the zone near the partially coupled zone (Figure 5a vs. 5b). However, the slab temperature in the ALA experiments using constant viscosity increases slower than those using composite viscosity. This implies that increase in temperature of the slab surface is caused by additional conduction, not the viscosity reduction of the thermal boundary layer observed in the ALA experiments using composite viscosity. In addition, the gradually increasing differences in temperature between the BA and ALA experiments using constant viscosity imply the continuous conduction of the heat generated by viscous dissipation along the slab (Figure 3 and 5a).

2.3.3 Evaluation of relative importance of diffusion and dislocation creep as the mantle flow mechanism in the mantle wedge

In this section, we evaluate the dominant mantle flow mechanism in the mantle wedge by comparing the end-member viscosities; diffusion and dislocation creep. Figure 6 shows pressure versus temperature paths for the top of the subducting slab corresponding to the BA and ALA experiments using constant viscosity, diffusion creep, dislocation creep and composite viscosity. The viscosities for diffusion and dislocation creep are calculated by using the same parameters in Table 1 and are non-dimensionalized with ~ 4.073×10^{21} Pa·s for the ALA experiments using composite viscosity. We find an excellent agreement between pressure versus temperature paths in the experiments using dislocation creep and composite viscosity, indicating that the composite rheology is controlled by dislocation creep. Figure 7 shows the log-scaled viscosity ratio of diffusion to dislocation creep in the mantle wedge for the BA and ALA experiments using composite viscosity. If the ratio is greater than 0, the viscosity from dislocation creep is lower than that from diffusion creep, which means dislocation creep becomes the predominant deformation mechanism. Except the middle of the stagnant lid and base of the mantle wedge deeper than ~150 km in the BA experiments, dislocation creep is the predominant rheology in the mantle wedge. In

both the BA and ALA experiments, the partially coupled zone develops a strong shear localized zone where dislocation creep is predominant.

In general, differences in the slab temperatures between the BA and ALA experiments are relatively small. However, we found significant differences in the slab temperatures between the BA and ALA experiments using diffusion creep (Figure 6). The pressure versus temperature paths of the BA experiments using diffusion creep have lower temperatures (~ 31 % lower at 54 km depth) than those using composite viscosity to approximately 70 km depth due to higher viscosity of the base of the serpentinite zone. However, because hot, low viscosity material from deeper in the mantle wedge creates a stronger thermal gradient below 70 km, the temperature increases faster and becomes similar to that of the BA experiments using dislocation creep and composite viscosity. In the ALA experiments using diffusion creep, we find considerable thinning of the thermal boundary layer above the slab surface; the heat generated by viscous dissipation reduces the viscosity of the thermal boundary layer by a factor of ~ 100 (~ 10 in the ALA experiments using composite viscosity). Therefore, hot and low viscosity mantle reaches very close to the slab surface and increases slab temperature up to 1046 ˚C causing considerable partial melting of the oceanic crust. This significant viscosity reduction is concentrated along the partially coupled zone and becomes weaker below the end of the partially coupled zone (100 km depth).

2.3.4 Effect of decoupling between the mantle wedge and subducting slab

Seismology, field observations and surface heat flow data in the forearc imply relatively low temperatures in the mantle wedge below the forearc [*Furukawa and Uyeda*, 1989; *Guillot et al.*, 2000; *Hacker et al.*, 2003a; 2003b; *Rondenay et al.*, 2008]. To attain the low temperatures below the forearc, decoupling between the mantle wedge and subducting slab has been applied along the top of the subducting slab because the decoupling weakens the flow in the mantle wedge below the forearc [e.g., *Abers et al.*, 2006; *Kneller et al.*, 2007; *Wada et al.*, 2008]. Hydrous minerals and pore pressure could justify the implementation of decoupling on the top of the subducting slab [*Bebout and Barton*, 1989; *Hyndman and Peacock*, 2003; *Morrow et al.*, 2000; *Peacock and Hyndman*, 1999]. A variety of

decoupling conditions have been used in numerical experiments and here we use a linear velocity ramp for the decoupling condition (Figure 1). In the BA and ALA experiments using composite viscosity, we observe very strong shear localization along the partially coupled zone (Figure 7). This suggests decoupling condition could be an important factor for the characteristics of shear localization. Therefore, we evaluate the effect of decoupling by comparing the results without decoupling (fully coupling, no reduction of velocity along the slab surface) to the results from our experiments that include decoupling. In numerical models which assume an overlying rigid lid and subducting slab, the singularity at the tip of the mantle wedge requires a special treatment. The singularity treatments have been discussed in previous studies [*van Keken et al.*, 2002; 2008] and a short ramp of the increasing velocity boundary condition is appropriate to suppress the singularity. However, the singularity treatment is neglected in this study and the effect of the singularity will be discussed later.

Figure 8 shows pressure versus temperature paths for the top of the subducting slab corresponding to the BA and ALA experiments by varying decoupling condition and the mantle rheology. In general, the pressure versus temperature paths show that the ALA experiments produce slightly higher slab temperature than the BA experiments except for those using diffusion creep. For example, temperature differences at 150 km depth between the BA and ALA experiments using a fully coupled zone are 18.3 ˚C (constant viscosity), 20.6 ˚C (dislocation creep) and 20.4 ˚C (composite viscosity). As described above, the higher slab temperature in the ALA experiments is attributed to viscous dissipation: additional heat conduction for constant viscosity and viscosity reduction of the thermal boundary layer for diffusion creep, dislocation creep and composite viscosity. The BA and ALA experiments using constant viscosity with a partially coupled zone produce hotter subducting slabs than those with a fully coupled zone. The differences between the two experiments become larger through the range of the partially coupled zone, indicating that the changes in flow style due to changes in decoupling condition affect the heating style of the subducting slab.

In the BA and ALA experiments using dislocation creep and composite viscosity, a fully coupled zone produces smoother pressure versus temperature paths compared with those using a partially coupled

zone. Compared with the experiments using a partially coupled zone, much weaker shear localization is observed along the fully coupled zone. Despite having no singularity treatment at the tip of the mantle wedge, a temperature peak at the tip is not observed in the ALA experiment, implying that viscosity reduction by dislocation creep due to high strain rate near the tip weakens viscous dissipation. In the BA and ALA experiments using a partially coupled zone, the small convection cell in the serpentinite zone is more isolated so that heat transfer between the serpentinite and wet olivine zones is suppressed. Therefore, heating of the subducting slab is weaker than that using a fully coupled zone. However, weaker heat transfer between the serpentinite and wet olivine zones prevents heat loss through the serpentinite zone; higher temperature and lower viscous mantle in the wet olivine zone makes the thermal boundary layer thinner. In addition, strong shear localization along the partially coupled zone reduces viscosity of the thermal boundary layer. Therefore, increases in temperature of the subducting slab are faster from the base of the wet olivine zone.

The BA experiments using diffusion creep produce pressure versus temperature paths similar to those using dislocation creep and composite viscosity. However, noticeably, the ALA experiments using diffusion creep have very high temperatures up to 1046.0 ˚C (partially coupled zone) and 841.1 ˚C (fully coupled zone). In the case using a fully coupled zone, the local temperature peak is observed at the tip of the mantle wedge, unlike the experiments using composite viscosity or dislocation creep. Even a partially coupled zone can not alleviate the temperature peak at the tip and the peak is related to the flow structure in the corner of the mantle wedge. In all the experiments using temperature and pressure dependent viscosity with a partially coupled zone, the flow above the subducting slab is faster than the prescribed velocity along the partially coupled zone because of the strong corner flow driven by the entire subducting slab. This creates a strong shear localization zone on the top of the subducting slab and reduces viscosity of the thermal boundary layer through dislocation creep (higher strain rate, lower viscosity, see eq. 12) in the experiments using composite viscosity or dislocation creep. Therefore, the heat generated by viscous dissipation is not large and does not thin the thermal boundary layer considerably. However, viscosity from diffusion creep is independent of strain rate (see eq. 11) and more

heat along the shear localization zone is generated than in the dislocation creep calculation. This heat thins the thermal boundary layer significantly and increases the slab temperature.

2.3.5 Summary of the other experiments varying dip, age and velocity of the subducting slab

In general, the temperature and flow in the BA and ALA experiments are more strongly affected by the variation of rheology (constant viscosity versus composite viscosity) than the variations of dip, age and velocity of the subducting slab, and compressibility. In the BA and ALA experiments using constant viscosity and the dips of 30 and 45 degrees, an isolated roll-like convection develops in the low viscosity zone and produces low surface heat flow in the forearc (Figure 9a, 2c and 2e). However, isolated roll-like convection is not observed in the experiments using the dip of 60 degrees (Figure 9b). In the BA and ALA experiments using composite viscosity, a strong corner flow increases the surface heat flow in the forearc and a very thick stagnant lid below the backarc develops in contrast to the experiments using constant viscosity (Figure 9c and 9d), consistent with the observations above.

Figure 10 shows mean temperatures of the top of the subducting slabs corresponding to the BA and ALA experiments varying dip, age and velocity of the subducting slab. As described above, different mantle rheologies result in significant differences in slab temperature. In general, the variation of age of the subducting slab systematically shifts temperature of the top of the subducting slab in the BA and ALA experiments. Increasing velocity of the subducting slab decreases the temperature of the top of the subducting slab because the slab has less time to be heated compared with that using lower velocity of the subducting slab. There is not a simple linear relation between dip and temperature of the subducting slab. Compressibility increases the temperature of the top of the subducting slab through the heat generated by viscous dissipation. In the ALA experiments using composite viscosity, the net increase in temperature of the top of the subducting slab due to the heat generated by viscous dissipation slightly decreases with velocity of the subducting slab. However, the net increase in temperature of the top of the subducting slab increases with increasing velocity of the subducting slab in the ALA experiments using constant viscosity. This suggests that the heat generated by viscous dissipation in the ALA experiments using

composite viscosity does not increase considerably with increasing velocity of the subducting slab because viscosity reduction due to heat and higher strain rate weakens viscous dissipation. In contrast to the ALA experiments using composite viscosity, viscosity in the ALA experiments using constant viscosity is independent of pressure, temperature and strain rate so the heat generated by viscous dissipation increases temperature of the top of the subducting slab with increasing velocity of the subducting slab.

2.4 Discussion

In the mantle wedge, mantle compressibility is mostly expressed by viscous dissipation and produces only small differences in the thermal and flow structures of the subduction zones (Figure 2 and 3). However, noticeably, the ALA experiments using diffusion creep produce a significantly thinned thermal boundary layer on the top of the subducting slab because higher strain rate on the top can not weaken viscous dissipation and large heat is generated. Except in this case, the effect of mantle compressibility on the subduction zone can be considered as minor, which may justify the broad use of incompressible models in subduction zone studies. Differences in rheology (constant viscosity vs. temperature and pressure dependent viscosity) in the mantle wedge produce major effects on the thermal and flow structures of the subduction zones. Also, variations of dip, age and velocity of the subducting slab are considered but, the effects of the variations on the thermal and flow structures of the subduction zones are relatively minor compared with the effects of differences in rheology on the structures (Figure 9). In general, similar thermal and flow structures develop in the experiments using diffusion, dislocation and composite viscosity.

From the end-member experiments using diffusion and dislocation creep, dislocation creep is the dominant flow mechanism in the mantle wedge (Figure 7). The observations of distinctive seismic anisotropy in the mantle wedge of the subduction zones such as Tonga [e.g., *Conder and Wiens*, 2006; *Long and van der Hilst*, 2005; *Long and Silver*, 2008] and laboratory experiments on the olivine

anisotropy [e.g., *Hirth and Kohlstedt*, 1995; *Jung and Karato*, 2001; *Karato and Wu*, 1993] are consistent with this observation. However, this may not negate the existence of diffusion creep in the mantle wedge. We assume the grain size for diffusion creep as a constant (0.1 mm) but, this is a somewhat arbitrary value which could be varied in the upper mantle [*Ranalli*, 1991; 1995; *van der Berg et al.*, 1993]. In addition, dynamic recrystallization during dislocation creep could reduce the grain size significantly; a jump of the predominant mechanism from dislocation to diffusion creep could be possible in the mantle wedge [*Poirier*, 1985; *Ranalli*, 1995; *Solomatov*, 2001; *Twiss*, 1977]. Therefore, grain size evolution is an important factor in determining which creep mechanism dominates in the mantle wedge and consideration of the evolution can be a potential improvement in subduction zone models.

Two decoupling conditions, partially and fully coupled zones are used in this study. A fully coupled zone produces little deformation (good coupling) between the subducting slab and mantle wedge; strong shear localization is not observed. However, a partially coupled zone generates strong shear localization along the zone in the BA and ALA experiments using pressure and temperature dependent viscosity because the prescribed velocity along the partially coupled zone is slower than the flow in the mantle wedge above. To simulate the shear zone on the top of the subducting slab, the prescribed velocity on the top of the subducting slab should match the mantle flow on the top. Therefore, the prescribed partially coupled zone (a linear velocity ramp) may not be a relevant decoupling condition to simulate the shear localization on the top of the subducting slab. The heat generation along the partially coupled zone in the ALA experiments using diffusion creep suggests that it is crucial that careful implementation of a partially coupled zone for the shear localization. Ultimately, to overcome this problem, a dynamically evolving partially coupled zone on the top of the subducting slab might be needed; velocity for a partially coupled zone evolves with the mantle flow above the zone.

In this study, the wet olivine and serpentinite zones are arbitrarily assumed. The extension of wet olivine zone may depend on the depth where dehydration of the subducting slab terminates; the wet olivine zone could be laterally extended or shrunk. We evaluate the effects of the extension of wet olivine zones on the thermal and flow structures of the subduction zones by varying the dehydration

termination depth: shallow (100 km depth), intermediate (150 km depth), and deep (200 km depth) with the 50 km thickness viscosity transition zone. Because serpentinite can exist under 700 ˚C, the extension of serpentinite zone would be controlled by temperature conditions of the mantle corner. The viscosity reduction numbers to express lower viscosity for serpentinite and wet olivine are also somewhat arbitrarily assumed so the numbers could be smaller or larger. Therefore, we evaluate the effects of the numbers on the thermal and flow structures: serpentinite zone (0.0001, 0.0005, 0.001, 0.01 and 0.05 – no serpentinite zone – with the fixed viscosity reduction number of 0.05 for wet olivine zone) and wet olivine zone (0.001, 0.01, 0.05, 0.1 and 1 – dry olivine – with the fixed viscosity reduction number of 0.0005 for serpentinite zone). For simplicity, we use the BA and ALA experiments using the dip of 45 degrees, 130 Myr old and velocity of 5 cm/year of the subducting slab with constant and composite viscosity.

First, we evaluate the effect of serpentinite zone on the thermal and flow structures of the subduction zone by varying viscosity reduction number. Figure 11 shows pressure versus temperature paths for the BA and ALA experiments using constant and composite viscosity. In the BA experiments, the effect of variation in viscosity reduction number is relatively small and the variation affects the flow in the serpentinite zone (Figure 10a). Smaller numbers isolate the serpentinite zone from the mantle corner. No serpentinite zone (number = 0.05) generates a corner flow reaching the tip of the mantle wedge and produces smooth pressure versus temperature paths. However, mantle compressibility creates noticeable differences in the thermal and flow structures, especially, near the top of the subducting slab which controls the slab temperature. The ALA experiments using constant viscosity produce small temperature perturbations but larger than that of the BA experiments. The effect of varying viscosity reduction number on the thermal boundary layer and slab temperature becomes distinctive in the ALA experiments using composite viscosity. Larger viscosity reduction numbers allow the hot mantle to reach the tip of the mantle wedge and generate more heat through viscous dissipation. Therefore, the thermal boundary layer along the top of the subducting slab becomes thinner and increases the slab temperature faster (Figure 11b).

Secondly, the effect of wet olivine zone on the thermal and flow structures of the subduction zones is evaluated with varying viscosity reduction number (Figure 12). In all the experiments, smaller numbers isolate the corner of the mantle wedge with an isolated convection cell, especially, in the experiments using constant viscosity. Even though the isolated corner of the mantle wedge, differences in temperature of the subducting slab are relatively small in the experiments using composite viscosity compared with those using constant viscosity (Figure 12a vs. 12c and 12b vs. 12d) because the degree of isolation of mantle corner is much weaker in the experiments using composite viscosity. Mantle compressibility creates noticeable differences in the thermal and flow structures of the subduction zones. In the ALA experiments using constant viscosity, additional heat from viscous dissipation increases temperatures of the slab and mantle wedge significantly. The ALA experiments using constant viscosity and no wet olivine zone increases the slab temperature more than that using composite viscosity and no wet olivine zone (Figure 11c vs. 11d). Compared with temperature increases in the ALA experiments using constant viscosity, temperature increases in the slab and mantle wedge are relatively small even in the experiments using no wet olivine zone. This implies that the heat from viscous dissipation is not considerable in the ALA experiments using composite viscosity compared with that using constant viscosity. As discussed above, higher viscosity generates larger heat energy through viscous dissipation but, increase in temperature decreases viscosity and weakens viscous dissipation as a counter effect. Therefore, the thermal and flow structures in the ALA experiments using composite viscosity are relatively insensitive to viscous dissipation.

The thermal and flow structures of the subduction zones are controlled by the extent of wet olivine zone. A larger wet olivine zone isolates the corner through an isolated convection cell at the corner in the BA and ALA experiments using constant viscosity. A weak isolation is observed at the corner in the BA and ALA experiments using composite viscosity. The effect of extent of wet olivine zone on the slab temperature is relatively small in the BA experiments using constant viscosity even though distinctive differences in the mantle flow and thermal structures (Figure 13a). In the ALA experiments using constant viscosity, smaller wet olivine zone creates much hotter slab temperature due

to stronger viscous dissipation in the dry olivine zone which starts 100 km depth (Figure 13b). Surprisingly, the slab temperature only shows very slight differences regardless the extent of wet olivine zone in the BA and ALA experiments. This implies that the thermal boundary layer on the top of the subducting slab is not significantly affected by the changes of corner flow in the mantle wedge.

In all the ALA experiments, we neglect the half rigid (slab) and half fluid (wedge) elements diagonally cut by the top of the subducting slab in the calculation of viscous dissipation. However, viscous dissipation on the top of the slab is thought to be extensive so this limitation needs to be overcome in the future studies. Here, we evaluate the effect of half rigid and fluid elements on the thermal and flow structures of the subduction zones by assuming the elements as whole fluid. No significant differences in the thermal and flow structures of the mantle wedge are observed in the experiments including the half rigid and fluid elements. However, we find noticeable differences in the slab temperatures from the experiments; 6.73 % and 7.03 % temperature increases for composite and diffusion viscosity, respectively (Figure 14). Although the heat from the half rigid and fluid elements increases the slab temperature, it is relatively minor and general patterns of slab heating are not changed. In addition, the increase in slab temperature would be smaller because heat will not be generated in the half solid elements. Therefore, neglecting the half rigid and fluid elements in the calculation of viscous dissipation could be justified in this study.

In the BA and ALA experiments using pressure and temperature dependent viscosity, we find a temperature jump at the top of the subducting slab ~ 70 km depth (Figure 6 and 8). The jump becomes distinctive in the ALA experiments with a partially coupled zone and larger viscosity contrast between serpentinite and wet olivine zones (Figure 8, 11 and 12). The large viscosity contrast develops a strong isolated convection cell in the corner of the mantle wedge and creates a temperature jump ~ 150 km depth even in the BA and ALA experiments using constant viscosity (Figure 12a and b). However, compared with the abrupt temperature jump ~ 70 km depth in the BA and ALA experiments using pressure and temperature dependent viscosity, the temperature jump ~ 150 km depth is smoothly changed through the viscosity transition zone. This implies that the abrupt large viscosity contrast due to the sharp transition

from serpentinite to wet olivine zones plays an important role in the thermal and flow structures in the corner, especially where a partially coupled zone isolates the serpentinite zone more than the case using a fully coupled zone. Higher strain rate at the boundary between the serpentinite and wet olivine zones creates significant heat through the viscous dissipation along the boundary in the ALA experiments using pressure and temperature dependent viscosity. However, the temperature jump in the ALA experiments using composite viscosity and dislocation creep is smoother and smaller compared with that using diffusion creep. This can be explained by viscosity reduction due to higher strain rate in the ALA experiments containing dislocation creep. As discussed above, diffusion viscosity can not be reduced by higher strain rate along the boundary between serpentinite and wet olivine zones. Therefore, the boundary creates extensive heat and thins the thermal boundary layer on the top of the subducting slab significantly: the abrupt temperature jump in the ALA experiments using diffusion creep (Figure 6). As well as implementation of decoupling condition, consideration of dynamically evolving serpentinite and wet olivine zones with a viscosity transition zone could be a possible improvement to alleviate the temperature jump.

2.5 Conclusion

We conduct numerical subduction experiments using incompressible (BA) and compressible (ALA) fluid models to evaluate the effect of compressibility on the thermal and flow structures of the subduction zones. Variations of dip, age and velocity of the subducting slab are considered with constant viscosity and pressure and temperature dependent viscosity. In general, there are only small differences between the results from the BA and ALA experiments. Unlike compressibility, rheology is a more important factor affecting the thermal and flow structures of the subduction zones; we observe lower surface heat flow in the arc in the BA and ALA experiments using constant viscosity and higher surface heat flow, faster slab heating and a very thick thermal lithosphere below the backarc in the BA and ALA experiments using pressure and temperature dependent viscosity. We find that compressibility affects the

slab temperature through a feed back with the heat generated by viscous dissipation. In the ALA experiments using constant viscosity, the heat generated by viscous dissipation increases the slab temperature faster through additional conduction across the slab surface. In the ALA experiments using pressure and temperature dependent viscosity, the heat energy generated by viscous dissipation is comparable with that using constant viscosity but, the heat thins the thermal boundary layer above the slab which is sensitive to temperature. Therefore, hot mantle deeper in the mantle wedge can reach closer to the slab surface and increases the slab temperature faster than the BA experiments using composite viscosity. In general, older age, steeper dip and slower velocity of the subducting slab reduce temperature of the mantle wedge, consistent with previous studies.

References

Abers, G. A., P. E. van Keken, E. A. Kneller, A. Ferris, and J. C. Stachnik (2006), The thermal structure of subduction zones constrained by seismic imaging: Implications for slab dehydration and wedge flow, *Earth and Planetary Science Letters*, *241*(3-4), 387-397.

Anderson, O. L., D. G. Issak, and H. Oda (1992), High temperature elastic constant data on minerals relevant to geophysics, *Review of Geophysics*, *30*, 57-90.

Anderson, O. L. (1995), Equations of State for Geophysics and Ceramic Science, *Oxford University Press, New York*.

Anderson, O. L. (2000), The Grüneisen ratio for the last 30 years, *Geophysical Journal International*, *143*(2), 279-294.

Arcay, D., E. Tric, and M. P. Doin (2005), Numerical simulations of subduction zones: Effect of slab dehydration on the mantle wedge dynamics, *Physics of the Earth and Planetary Interiors*, *149*(1-2), 133-153.

Bebout, G. E., and M. D. Barton (1989), Fluid flow and metasomatism in a subduction zone hydrothermal system: Catalina Schist terrane, California, *Geology*, *17*(11), 976-980.

Bercovici, D. (2003), The generation of plate tectonics from mantle convection, *Earth and Planetary Science Letters*, *205*(3-4), 107-121.

Billen, M. I., and M. Gurnis (2001), A low viscosity wedge in subduction zones, *Earth and Planetary Science Letters*, *193*(1-2), 227-236.

Brocher, T., T. Parsons, A. Trehu, C. Snelson, and M. Fisher (2003), Seismic evidence for widespread serpentinizted forearc upper mantle along the Cascadia margin, *Geology*, *31*, 267-270.

Conder, J. A. (2005), A case for hot slab surface temperatures in numerical viscous flow models of subduction zones with an improved fault zone parameterization, *Physics of the Earth and Planetary Interiors*, *149*(1-2), 155-164.

Conder, J. A., and D. A. Wiens (2006), Seismic structure beneath the Tonga arc and Lau back-arc basin determined by joint Vp, Vp/Vs tomography, *Geochemistry Geophysics Geosystems*, *7*, doi:10.1029/2005GC001113

Currie, C. A., K. Wang, R. D. Hyndman, and J. He (2004), The thermal effects of steady-state slab-driven mantle flow above a subducting plate: the Cascadia subduction zone and backarc, *Earth and Planetary Science Letters*, *223*(1-2), 35-48.

Currie, C. A., and R. D. Hyndman (2006), The thermal structure of subduction zone back arcs *Journal of Geophysical Research*, *111*, doi:10.1029/2005JB004024

Currie, C. A., R. S. Huismans, and C. Beaumont (2008), Thinning of continental backarc lithosphere by flow-induced gravitational instability, *Earth and Planetary Science Letters*, *269*(3-4), 436-447.

Davies, D. R., J. H. Davies, O. Hassan, K. Morgan, and P. Nithiarasu (2008), Adaptive Finite Element Methods in Geodynamics; Convection Dominated Mid-Ocean Ridge and Subduction Zone Simulations, *International Journal of Numerical Methods for Heat & Fluid Flow*, *18(7/8)*, 1015-1035.

Davies, J. H., and D. J. Stevenson (1992), Physical Model of Source Region of Subduction Zone Volcanics, *Journal of Geophysical Research*, *97(B2)*, 2037-2070.

Furukawa, Y., and S. Uyeda (1989), Thermal state under the Tohoku Arc with consideration of crustal heat generation, *Tectonophysics*, *164*(2-4), 175-187.

Gibert, B., U. Seipold, A. Tommasi, and D. Mainprice (2003), Thermal diffusivity of upper mantle rocks: Influence of temperature, pressure, and the deformation fabric, *Journal of Geophysical Research*, *108*, doi:10.1029/2002JB002108

Guillot, S., K. Hattori, H. iko, and J. de Sigoyer (2000), Mantle wedge serpentinization and exhumation of eclogites: Insights from eastern Ladakh, northwest Himalaya, *Geology*, *28*(3), 199-202.

Hacker, B. R., G. A. Abers, and S. M. Peacock (2003a), Subduction factory - 1. Theoretical mineralogy, densities, seismic wave speeds, and H_2O contents, *Journal of Geophysical Research, 108*(B1), doi:10.1029/2001JB001127

Hacker, B. R., S. M. Peacock, G. A. Abers, and S. D. Holloway (2003b), Subduction factory - 2. Are intermediate-depth earthquakes in subducting slabs linked to metamorphic dehydration reactions?, *Journal of Geophysical Research, 108*(B1), doi:10.1029/2001JB001129

Hager, B. H., and M. A. Richards (1989), Long-Wavelength Variations in Earth's Geoid: Physical Models and Dynamical Implications, *Philosophical Transactions of the Royal Society of London. Series A, Mathematical and Physical Sciences, 328*(1599), 309-327.

Heskell, N. A. (1935), The motion of a fluid under a surface load, 1, *Physics, 6*, 265-269.

Heskell, N. A. (1936), The motion of a fluid under a surface load, 2, *Physics, 7*, 56-61.

Hilairet, N., B. Reynard, Y. Wang, I. Daniel, S. Merkel, N. Nishiyama, and S. Petitgirard (2007), High-pressure creep of serpentine, interseismic deformation, and initiation of subduction, *Science, 318*(5858), 1910-1913.

Hirth, G., and D. Kohlstedt (1995), Experimental constraints on the dynamics of the partially molten upper mantle 2. Deformation in the dislocation creep regime, *Journal of Geophysical Research, 100*, 15441-15449.

Hofmeister, A. M. (1999), Mantle values of thermal conductivity and the geotherm from phonon lifetimes, *Science, 283*(5408), 1699-1706.

Honda, S., and M. Saito (2003), Small-scale convection under the back-arc occurring in the low viscosity wedge, *Earth and Planetary Science Letters, 216*(4), 703-715.

Hughes, T. (1987), The Finite Element Method: Linear Static and Dynamics Finite Element Analysis, *Prentice-Hall, Englewood Cliffs, New Jersey*

Hughes, T. J. R., and A. Brooks (1979), A multidimensional upwind scheme with no crosswind diffusion, in T. J. R. Hughes, ed., *Finite element methods for convection dominated flows, AMD, 34*, 19-35,

Presented at the Winter Annual Meeting of the ASME, Amer. Soc. Mech. Engrs. (ASME), New York.

Hyndman, R. D., and S. M. Peacock (2003), Serpentinization of the forearc mantle, *Earth and Planetary Science Letters, 212*(3-4), 417-432.

Ita, J., and L. Stixrude (1992), Petrology, Elasticity, and Composition of the Mantle Transition Zone, *Journal of Geophysical Research, 97 (B5)*, 6849-6866.

Ita, J., and S. D. King (1994), Sensitivity of convection with an endothermic phase change to the form of governing equations, initial conditions, boundary conditions, and equation of state, *Journal of Geophysical Research, 99*(B8), 15919-15938.

Ita, J., and S. D. King (1998), The influence of thermodynamic formulation on simulations of subduction zone geometry and history, *Geophysical Research Letters, 25*(9), 1463-1466.

Iwamori, H. (1997), Heat sources and melting in subduction zones, *Journal of Geophysical Research, 102*, 14803-14820.

Iwamori, H. (1998), Transportation of H_2O and melting in subduction zones, *Earth and Planetary Science Letters*, *160*(1-2), 65-80.

Jarvis, G., and D. McKenzie (1980), Convection in a compressible fluid with infinite Prandtl number, *Journal of Fluid Mechanics*, *96*, 515-583.

Jung, H., and S.-i. Karato (2001), Water-induced fabric transitions in olivine, *Science*, *293*(5534), 1460-1463.

Kameyama, M., D. A. Yuen, and S. I. Karato (1999), Thermal-mechanical effects of low-temperature plasticity (the Peierls mechanism) on the deformation of a viscoelastic shear zone, *Earth and Planetary Science Letters, 168*(1-2), 159-172.

Karato, S.-I., and P. Wu (1993), Rheology of the upper mantle: a synthesis, *Science, 260*, 771-778.

Karato, S. (1992), On the Lehmann discontinuity, *Geophysical Research Letters*, *19*, 2255-2258.

Kelemen, P. B., J. L. Rilling, E. M. Parmentier, M. Luc, and B. R. Hacker (2003), Thermal structure due to solid-state flow in the mantle wedge beneath arcs, in *Inside the Subduction Factory, edited by J. Eiler, Geophysical Monograph, 138*, 293-311.

Kincaid, C., and I. S. Sacks (1997), Thermal and dynamical evolution of the upper mantle in subduction zones, *Journal of Geophysical Research, 102*, 12295-12315.

King, S. D., A. Raefsky, and B. H. Hager (1990), Conman: vectorizing a finite element code for incompressible two-dimensional convection in the Earth's mantle, *Physics of the Earth and Planetary Interiors*, *59*(3), 195-207.

King, S. D., and G. Masters (1992), An inversion for radial viscosity structure using seismic tomography, *Geophysical Research Letter*, *19*(15), 1551-1554.

King, S. D. (2001), Subduction zones: observations and geodynamic models, *Physics of the Earth and Planetary Interiors*, *127*(1-4), 9-24.

Kittel, C. (1956), Introduction to Solid State Physics, 2nd Ed., *John Wiley & Sons, New York*.

Kneller, E. A., P. E. van Keken, S. Karato, and J. Park (2005), B-type olivine fabric in the mantle wedge: Insights from high-resolution non-Newtonian subduction zone models, *Earth and Planetary Science Letters*, *237*(3-4), 781-797.

Kneller, E. A., P. E. van Keken, I. Katayama, and S. Karato (2007), Stress, strain, and B-type olivine fabric in the fore-arc mantle: Sensitivity tests using high-resolution steady-state subduction zone models, *Journal of Geophysical Research*, *112*(B4), doi:10.1029/2006JB004544

Leng, W., and S. Zhong (2008), Viscous heating, adiabatic heating and energetic consistency in compressible mantle convection, *Geophysical Journal International*, *173*, 693-702.

Long, M. D., and R. D. van der Hilst (2005), Upper mantle anisotropy beneath Japan from shear wave splitting, *Physics of the Earth and Planetary Interiors*, *151*(3-4), 206-222.

Long, M. D., and P. G. Silver (2008), The subduction zone flow field from seismic anisotropy: A global view, *Science*, *319*(5861), 315-318.

McKenzie, D. P., and J. C. Sclater (1968), Heat-flow inside the island arcs of the northwest Pacific, *Journal of Geophysical Research, 73*, 3173-3179.

McKenzie, D. P. (1969), Speculations on the Consequences and Causes of Plate Motions, *Geophysical Journal of the Royal Astronomical Society, 18*, 1-32.

Mei, S., W. Bai, T. Hiraga, and D. L. Kohlstedt (2002), Influence of melt on the creep behavior of olivine-basalt aggregates under hydrous conditions, *Earth and Planetary Science Letters, 201*(3-4), 491-507.

Minear, J. W., and M. N. Toksoz (1970), Thermal regime of a downgoing slab and new global tectonics, *Journal of Geophysical Research, 75*, 1397-1419.

Mitrovica, J. X. (1996), Haskell [1935] revisited, *Journal of Geophysical Research, 101*(B1), 555-569.

Morrow, C. A., D. E. Moore, and D. A. Lockner (2000), The effect of mineral bond strength and absorbed water on fault gouge frictional strenghth, *Geophysical Research Letters, 27*, 815-818.

Oxburgh, E. R., and D. L. Turcotte (1968), Problem of high heat flow and volcanism associated with zones of descending mantle convective flow, *Nature, 218*, 1041-1043.

Peacock, S. M. (1990), Fluid processes in subduction zones, *Science*, *248*(4953), 329-337.

Peacock, S. M. (1991), Numerical simulation of subduction zone pressure-temperature-time paths: Constraints on fluid production and arc magmatism, *Philosophical Transactions of the Royal Society of London Series a-Mathematical Physical and Engineering Sciences*, *335*(1638), 341-353.

Peacock, S. M., T. Rushmer, and A. B. Thompson (1994), Partial melting of subducting oceanic crust, *Earth and Planetary Science Letters, 121*(1-2), 227-244.

Peacock, S. M. (1996), Thermal and petrological structure of subduction zones (overview) *In Subduction, Top to Bottom, Geophysical Monography, 96, edited by G. E. Bebout et al.*, 119-134.

Peacock, S. M., and R. D. Hyndman (1999), Hydrous minerals in the mantle wedge and the maximum depth of subduction thrust earthquakes, *Geophysical Research Letters*, *26*(16), 2517-2520.

Peacock, S. M. (2003), Thermal structure and metamorphic evolution of subducting slab, in *Inside the Subduction Factory, Geophysical Monograph, 138, edited by J. Eiler*, 7-22.

Peacock, S. M., P. E. van Keken, S. D. Holloway, B. R. Hacker, G. A. Abers, and R. L. Fergason (2005), Thermal structure of the Costa Rica - Nicaragua subduction zone, *Physics of the Earth and Planetary Interiors*, *149*(1-2), 187-200.

Poirier, J. P. (1985), Creep of Crystals-High Temperature Deformation Processes in Metals, Ceramics and Minerals, *Cambridge University Press, Cambridge*.

Ranalli, G. (1991), The microphysical approach to mantle rheology, *In: Sabadini, R., Lambeck, K., Boschi, E. (Eds.), Glacial Isostacy, Sea-Level and Mantle Rheology*, 343-378.

Ranalli, G. (1995), Rheology of the Earth, 2nd Edition, *Chapman & Hall, London*.

Ranalli, G. (2001), Mantle rheology: radial and lateral viscosity variations inferred from microphysical creep laws, *Journal of Geodynamics*, *32*(4-5), 425-444.

Reynard, B., N. Hilairet, E. Balan, and M. Lazzeri (2007), Elasticity of serpentines and extensive serpentinization in subduction zones, *Geophysical Research Letters*, *34*, doi: 10.1029/2007GL030176

Ricard, Y., and B. Wuming (1991), Inferring the viscosity and the 3-D density structure of the mantle from geoid, topography and plate velocities, *Geophysical Journal International*, *105*(3), 561-571.

Richards, M. A., and B. H. Hager (1984), Geoid Anomalies in a Dynamic Earth, *Journal of Geophysical Research*, *89*, 5987-6002.

Rondenay, S., phane, G. A. Abers, and P. E. van Keken (2008), Seismic imaging of subduction zone metamorphism, *Geology*, *36*(4), 275-278.

Savage, M. K. (1999), Seismic anisotropy and mantle deformation: What have we learned from shear wave splitting?, *Review of Geophysics*, *37*, 65-106.

Schmidt, M. W., and S. Poli (1998), Experimentally based water budgets for dehydrating slabs and consequences for arc magma generation, *Earth and Planetary Science Letters*, *163*(1-4), 361-379.

Schubert, G., D. L. Turcotte, and P. Olson (2001), Mantle Convection in the Earth and Planets, *Cambridge University Press, Cambridge*.

Silver, P. G. (1996), Seismic anisotrophy beneath the continents: Probing the depths of geology, *Annual Review of Earth and Planetary Sciences, 24*(1), 385-432.

Solomatov, V. S. (2001), Grain size-dependent viscosity convection and the thermal evolution of the Earth, *Earth and Planetary Science Letters, 191*(3-4), 203-212.

Stixrude, L., and C. Lithgow-Bertelloni (2005), Thermodynamics of mantle minerals - I. Physical properties, *Geophysical Journal International, 162*(2), 610-632.

Twiss, R. J. (1977), Theory and applicability of a recrystallized grain size paleopiezometer, *Pure and Applied Geophysics, 115*, 227-244.

Ulmer, P., and V. Trommsdorff (1995), Serpentine stability to mantle depths and subduction-related magmatism, *Science, 268*(5212), 858-861.

Ulmer, P. (2001), Partial melting in the mantle wedge -- the role of H_2O in the genesis of mantle-derived `arc-related' magmas, *Physics of the Earth and Planetary Interiors, 127*(1-4), 215-232.

van der Berg, A. P., P. E. van Keken, and D. Yuen (1993), The effects of a composite non-Newtonian and Newtonian rheology on mantle convection, *Geophysical Journal International, 115*, 62-78.

van Hunen, J., S. J. Zhong, N. M. Shapiro, and M. H. Ritzwoller (2005), New evidence for dislocation creep from 3-D geodynamic modeling of the Pacific upper mantle structure, *Earth and Planetary Science Letters, 238*(1-2), 146-155.

van Keken, P. E., B. Kiefer, and S. M. Peacock (2002), High-resolution models of subduction zones: Implications for mineral dehydration reactions and the transport of water into the deep mantle, *Geochemistry Geophysics Geosystems, 3*, doi: 10.1029/2001GC000256

van Keken, P. E., C. Currie, S. D. King, M. D. Behn, A. Cagnioncle, J. He, R. F. Katz, S.-C. Lin, E. M. Parmentier, M. Spiegelman, and K. Wang (2008), A community benchmark for subduction zone modeling, *Physics of the Earth and Planetary Interiors, 171*(1-4), 187-197.

Wada, I., K. Wang, J. He, and R. D. Hyndman (2008), Weakening of the subduction interface and its effects on surface heat flow, slab dehydration, and mantle wedge serpentinization, *Journal of Geophysical Research, 113,* doi: 10.1029/2007JB005190

Wu, J., and D. A. Yuen (1991), Post-glacial relaxation of a viscously stratified compressible mantle, *Geophysical Journal International, 104*(2), 331-349.

Wu, P. (1998), Postglacial rebound modeling with power-law rheology, *In: Wu, P. (Ed.), Dynamics of the Ice Age Earth-A Modern Perspective, Trans Tech Publications, Zurich*, 365-382.

Wu, P. (1999), Modelling postglacial sea levels with power-law rheology and a realistic ice model in the absence of ambient tectonic stress, *Geophysical Journal International, 139,* 691-702.

Zhang, S. X., and D. A. Yuen (1996), Various influences on plumes and dynamics in time-dependent, compressible mantle convection in 3-D spherical shell, *Physics of the Earth and Planetary Interiors*, *94*(3-4), 241-267.

Table 2.1 Model parameters

width (km) for dip: 30 degrees	$600\sqrt{3}$
45 degrees	600
60 degrees	$600/\sqrt{3}$
depth (km)	400
surface density (kg/m^3)	3300
gravitational acceleration (m/s^2)	9.81
surface temperature (K)	273
temperature contrast (K)	1550
heat capacity (J/kg·K)*	1200
thermal conductivity (W/m·K)*	3.96
thermal expansivity (/K)*	2.0×10^{-5}

*: These values are varying with respect to temperature, pressure and mineralogy (e.g., *Gibert et al.*, 2003; *Hofmeister*, 1999). We select 'representative' values for the upper mantle condition.

Table 2.2 Rheological parameters (from *Karato and Wu*, 1993)

E_{diff} (J/mol)	300×10^{3}
E_{disloc} (J/mol)	540×10^{3}
V_{diff} (m^3/mol)	6.0×10^{-6}
V_{disloc} (m^3/mol)	1.5×10^{-5}
A_{diff} ($m^{2.5}$/Pa·s)	6.1×10^{-19}
A_{disloc} ($s^{1.5}$/$Pa^{3.5}$)	2.4×10^{-16}
d_g (m)	1.0×10^{-3}
m (·)	2.5
n (·)	3.5
R (J/mol)	8.314

E: activation energy, V: activation volume, A: prefactor, d_g: grain size, m: grain size exponent, n: stress exponent, and R: gas constant

Figure 2.1

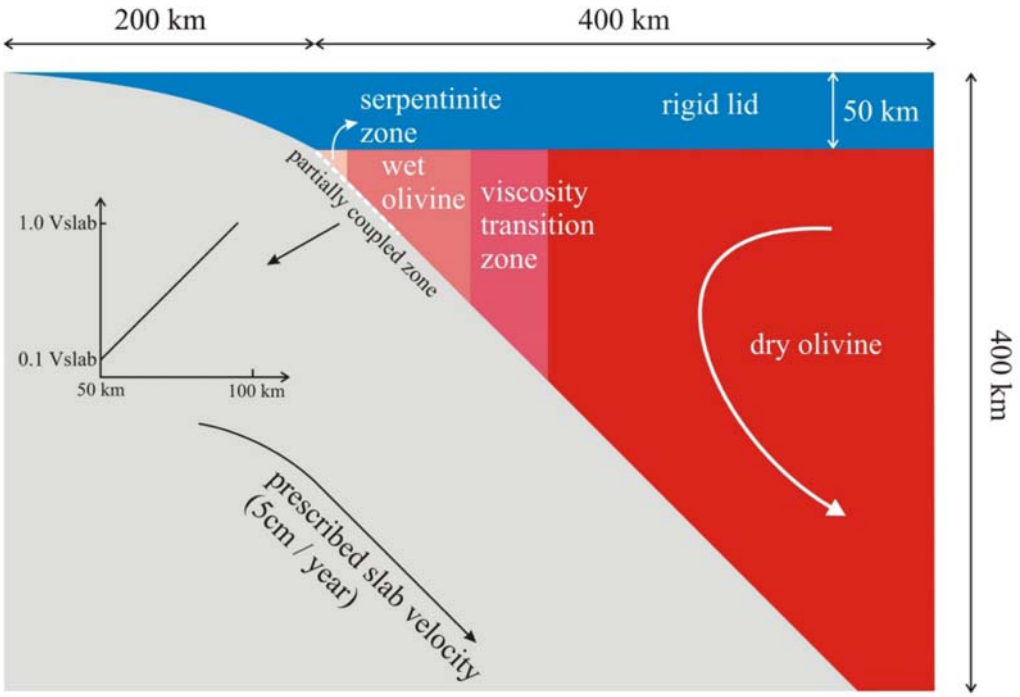

Schematic diagram of the subduction zone model using the dip of 45 degrees for the straight slab and the subducting slab velocity of 5 cm/year. The subducting slab and upper mantle below the slab are subducted together. For details about initial and boundary conditions, rheology and a decoupling condition, see text.

Figure 2.2

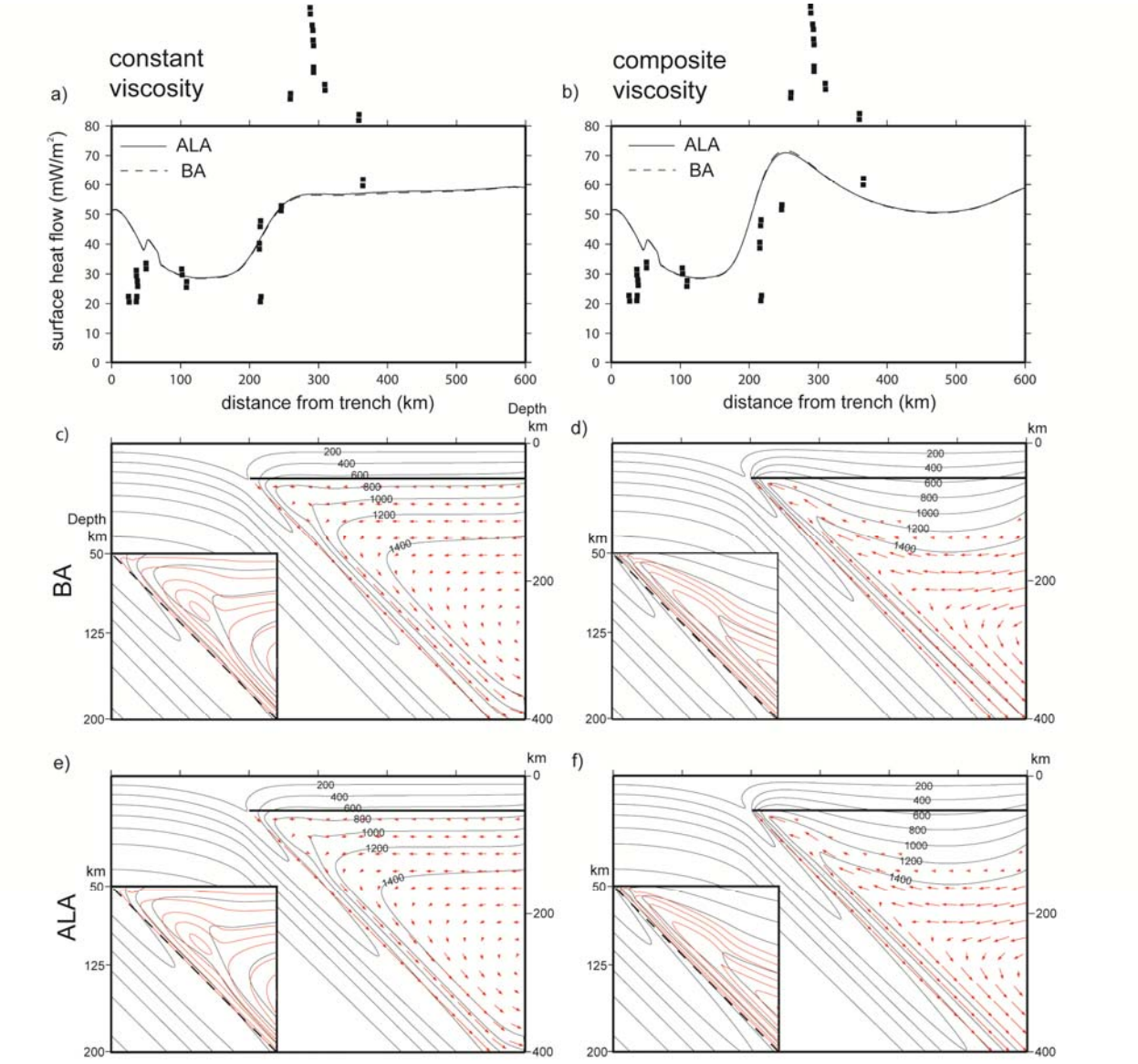

Surface heat flow, temperature and flow in the mantle wedge resulting from the BA and ALA experiments using constant and composite viscosity. In the surface heat flow (a and b), a small ramp of heat flow from 50 km to 70 km distance from the trench is caused by the irregularly prescribed step-like slab surface for the kinematically driven subducting slab (see text). The observed surface heat flow data are (filled black square) from *Furukawa and Uyeda* [1989] for the Japanese subduction zone. (c) and (e), and (d) and (f) show the temperature and flow in the mantle wedge in the BA and ALA experiments using constant and composite viscosity, respectively. The horizontal thick solid line at 50 km depth indicates

the bottom of the overlying rigid lid and the diagonal velocity vectors at the base of the mantle wedge correspond to the top slab velocity. In the experiments using composite viscosity, velocity vectors in the mantle wedges show stronger coupling (larger velocity vectors) between the mantle wedge and subducting slab, compared with the experiments using constant viscosity. The figures illustrated at the left-bottom show the detailed mantle temperature and flow in the low viscosity zone (serpentinite and wet olivine zones) using tracer-lines. The diagonal dashed line corresponds to the top of the subducting slab. In the experiences using composite viscosity, the tracers in the thermal lithosphere are extremely slow, so they are not displayed in the figures. The unit of temperature used here is Celsius.

Figure 2.3

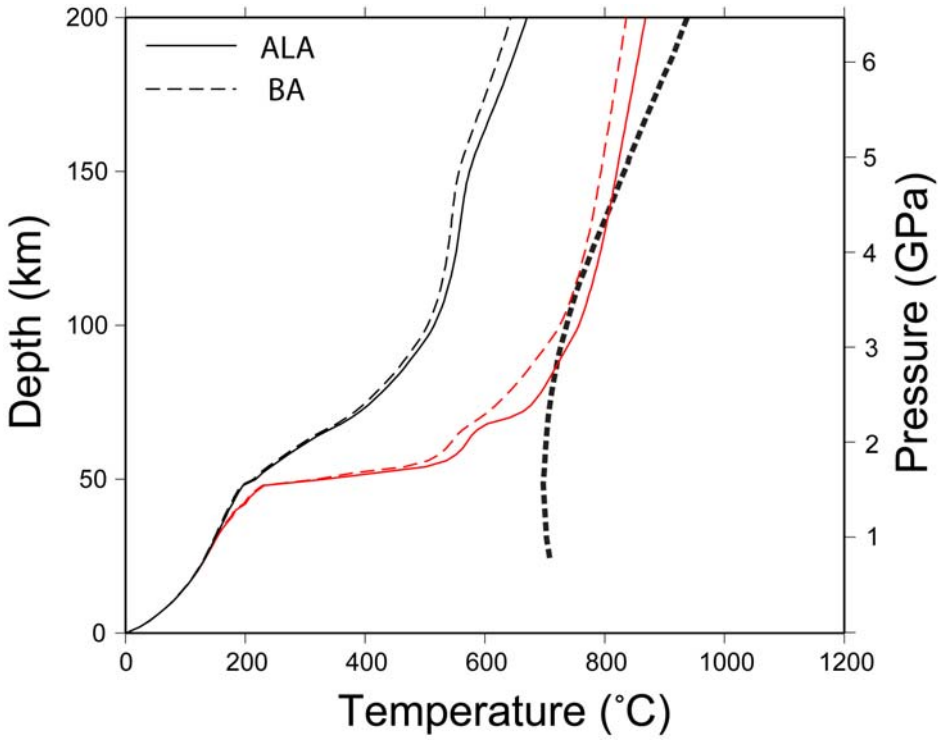

Pressure (depth) versus temperature paths for the top of the subducting slab corresponding to the BA and ALA experiments using constant and composite viscosity. Black and red colored lines correspond to the experiments using constant and composite viscosity, respectively. The dashed and solid lines indicate the BA and ALA experiments, respectively. The H_2O-saturated basalt solidus comes from *Schmidt and Poli* [1998] and partial melting of the top region of the slab is expected in the experiments using composite viscosity. The pressure is simply calculated by using constant density of 3300 kg/m^3 and gravitational acceleration of 9.81 m/s^2. Due to compressibility, pressure in the ALA experiments is slightly higher than that in the BA experiments at the same depth. However, the small differences in pressure between the BA and ALA experiments (e.g., ~ 0.1 GPa at a 200 km depth) and uncertainty of the H_2O-saturated basalt solidus justify the use of the simple pressure calculation for pressure description. This simple pressure description is used in the other figures.

Figure 2.4

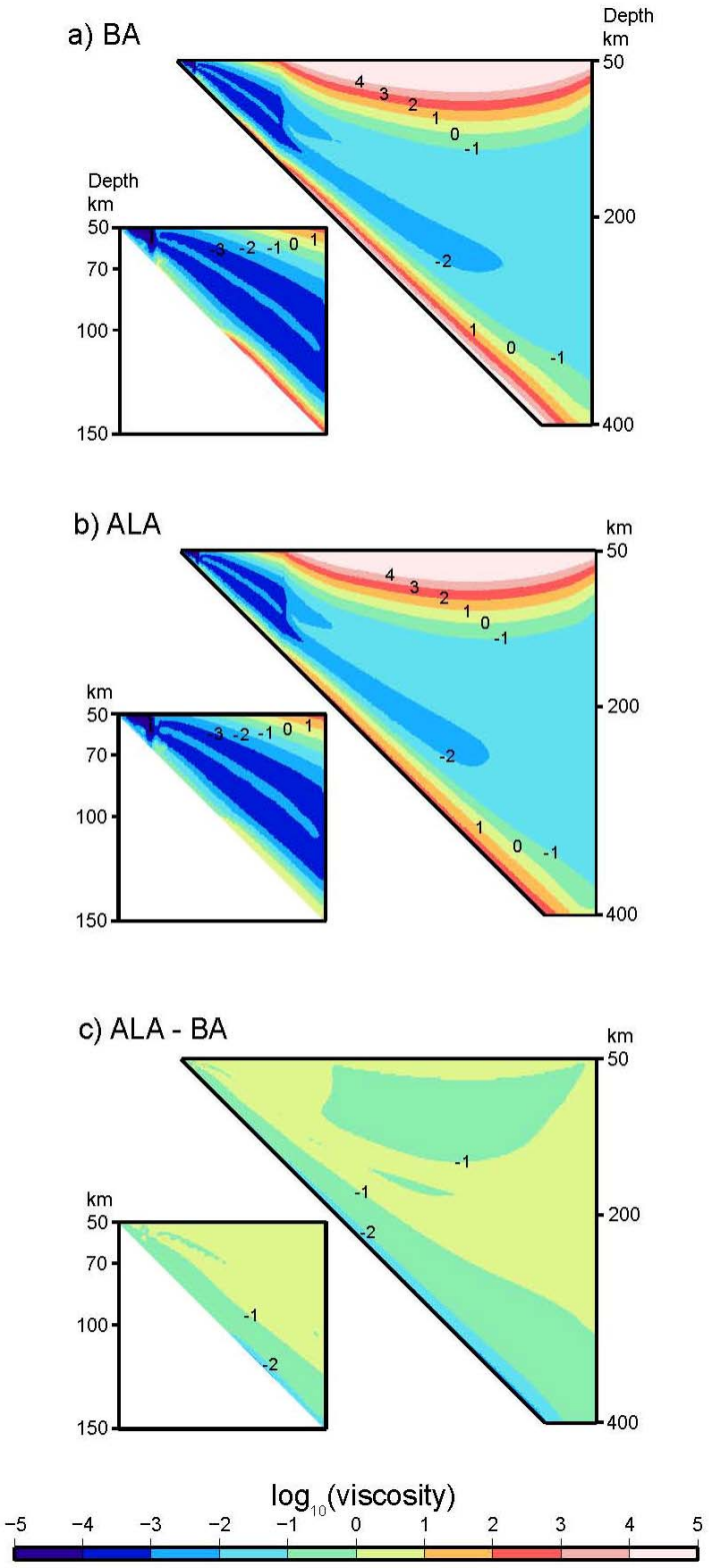
a) BA
Depth
km
50
200
400
Depth
km
50
70
100
150
b) ALA
km
c) ALA - BA
log10(viscosity)
−5 −4 −3 −2 −1 0 1 2 3 4 5

Log-scaled normalized viscosity in the mantle wedge from the BA and ALA experiments using composite viscosity. Normalization is conducted by using the bottom viscosity (~ 4.073×10^{21} Pa·s) calculated from diffusion creep with the temperature of 1550 ˚C and pressure at 400 km depth corresponding to the ALA experiments. Due to compressibility, viscosity of the ALA experiments is slightly higher than that of the BA experiments: ~ 3.487×10^{21} Pa·s (BA) versus ~ 4.073×10^{21} Pa·s (ALA) with the bottom pressure and 1550 ˚C. Except for the thermal boundary layer develops on the top of the subducting slab and the bottom of the overlying lithosphere, serpentinite and wet olivine zones produce lower viscosities compared with the viscosities in the dry olivine zone. (c) shows the viscosity contrast between the BA and ALA experiments by subtracting the viscosity of the BA from that of the ALA. Lower viscosity zone above the subducting slab is observed and represents thinner thermal boundary layer on the subducting slab in the ALA experiments (for details, see text).

Figure 2.5

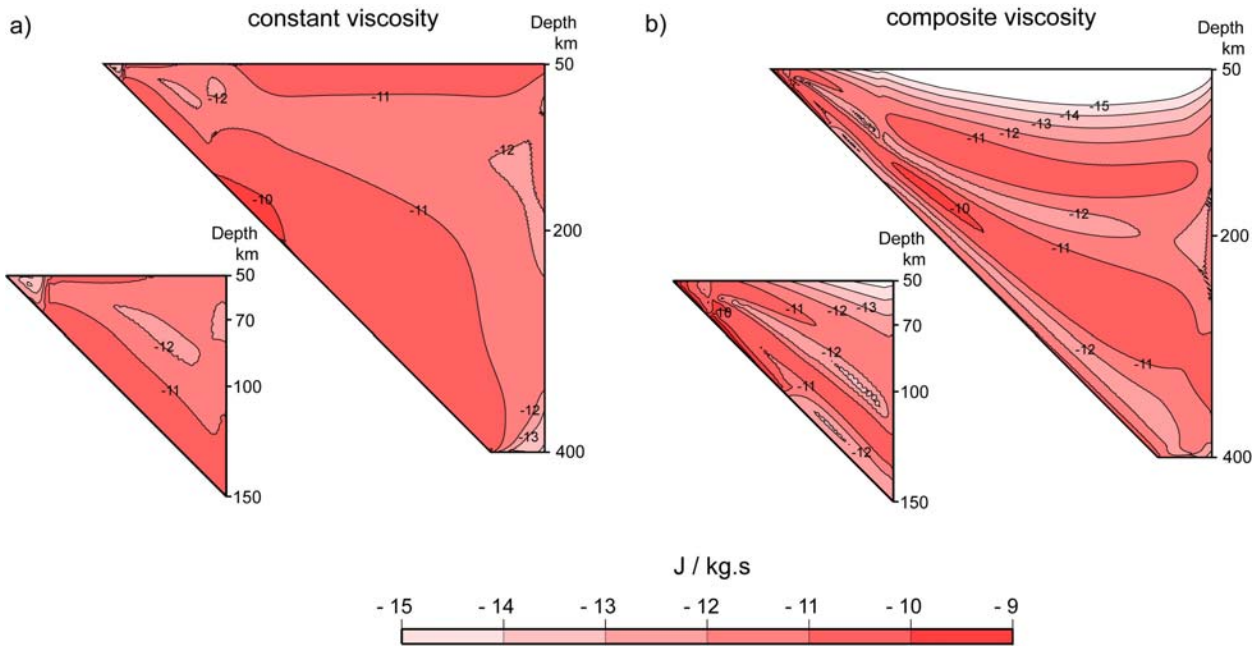

Heat generated by viscous dissipation in the mantle wedge for the ALA experiments using constant and composite viscosity. (a) shows the heat production from the ALA experiments using constant viscosity. On the slab surface, the calculated heat energy is around 10^{-10} (J/kg·s) comparable with the heat production calculated in *McKenzie* [1969]. The ALA experiments using composite viscosity (b) show a complicated heat production distribution. Localized strong viscous dissipation on the partially coupled zone implies very strong shear localization (large changes in strain rate) above the zone. Larger heat energy is generated below the thermal lithosphere and above the subducting slab where strain rate is relatively high. White colored region produces very little heat energy ($< 10^{-15}$ J/kg·s).

Figure 2.6

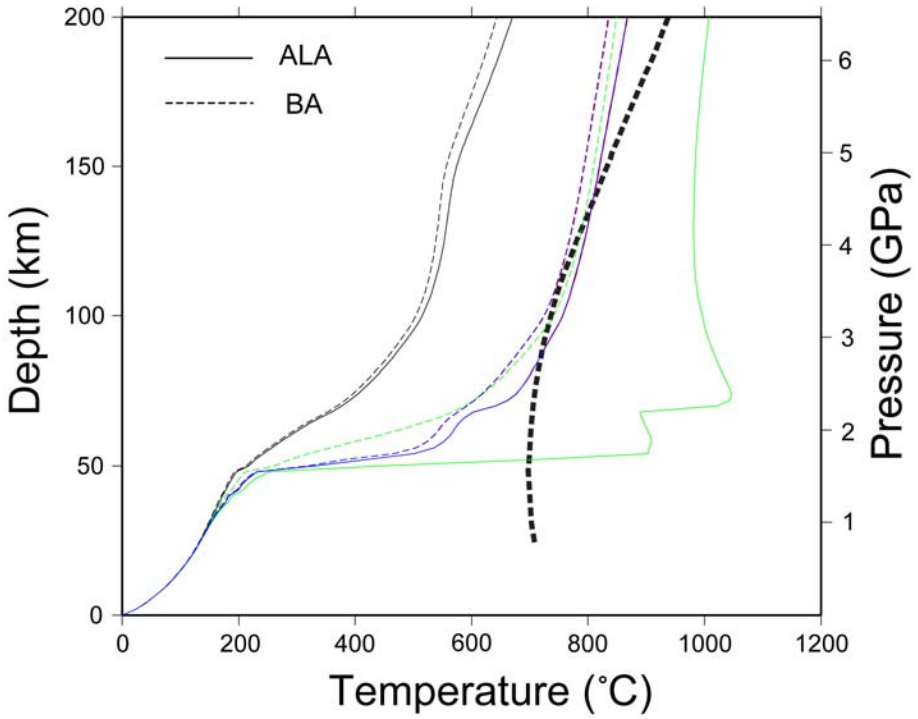

Pressure versus temperature paths for the top of the subducting slab corresponding to the BA and ALA experiments using constant viscosity, diffusion creep, dislocation creep and composite viscosity. Black, green, blue and red colors correspond to constant viscosity, diffusion creep, dislocation creep and composite viscosity, respectively. The paths for constant and composite viscosity are the same as Figure 3. The pressure and temperature paths for dislocation creep and composite viscosity almost overlap each other, which indicates the predominance of dislocation creep in the BA and ALA experiments using composite viscosity (see text for details.). The H_2O-saturated basalt solidus comes from *Schmidt and Poli* [1998].

Figure 2.7

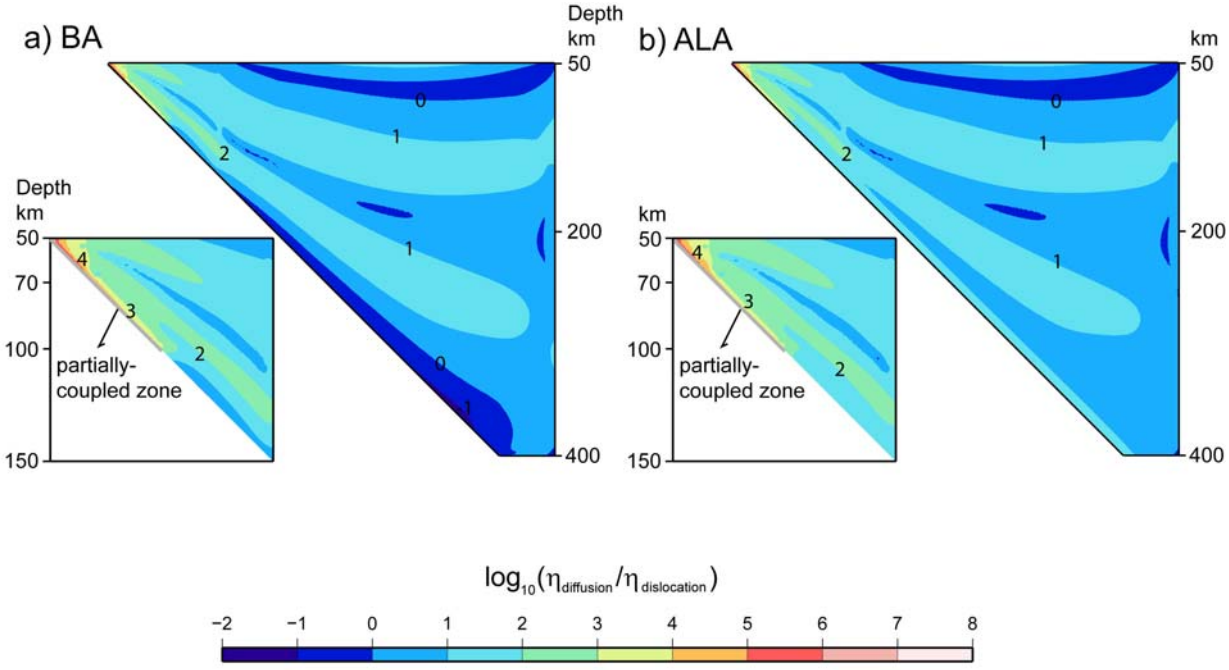

Log-scaled viscosity ratio of diffusion to dislocation creep in the mantle wedge for the BA and ALA experiments using composite viscosity. Dislocation creep becomes the predominant mantle rheology in the region where strain rate is high, especially, by the partially coupled zone. In the ALA experiments using composite viscosity (b), the predominance of dislocation creep above the slab surface is extended to the bottom of the box.

Figure 2.8

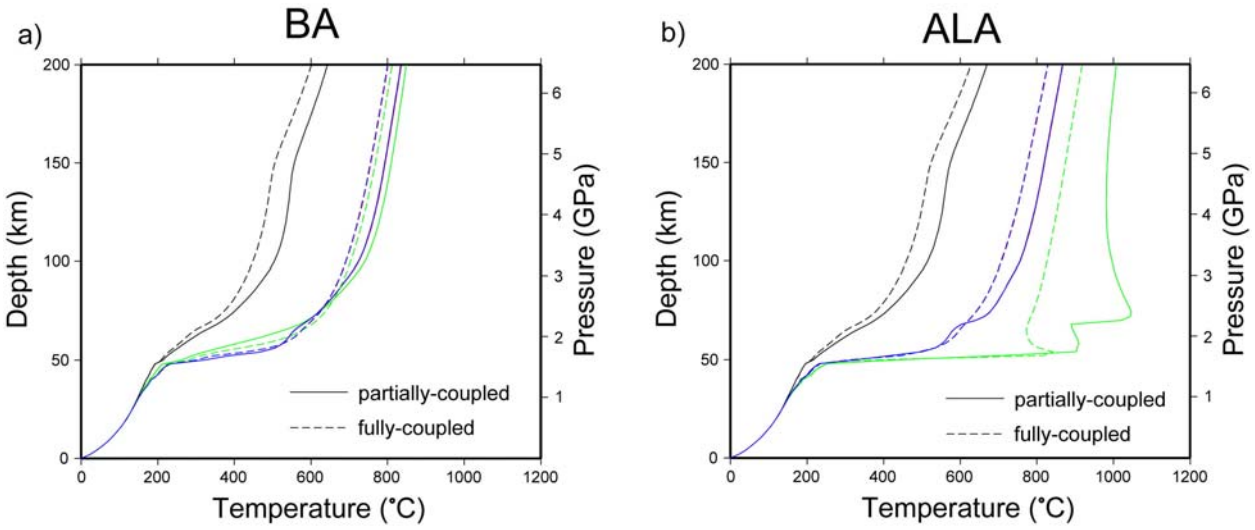

Pressure versus temperature paths for the top of the subducting slab by using a partially and fully coupled zone. The solid and dashed lines correspond to partially and fully coupled zones, respectively. (a) shows pressure versus temperature paths in the BA experiments using constant viscosity (black), diffusion creep (green), dislocation creep (blue) and composite viscosity (red). (b) shows the same as the (a) except for consideration of compressibility. In the BA and ALA experiments using dislocation creep and composite viscosity, pressure versus temperature paths almost overlap each other. Except the ALA experiments using diffusion creep, pressure versus temperature paths in the ALA experiments show systematic increases in temperature through viscosity reduction or additional heat conduction due to the heat generated by viscous dissipation.

Figure 2.9

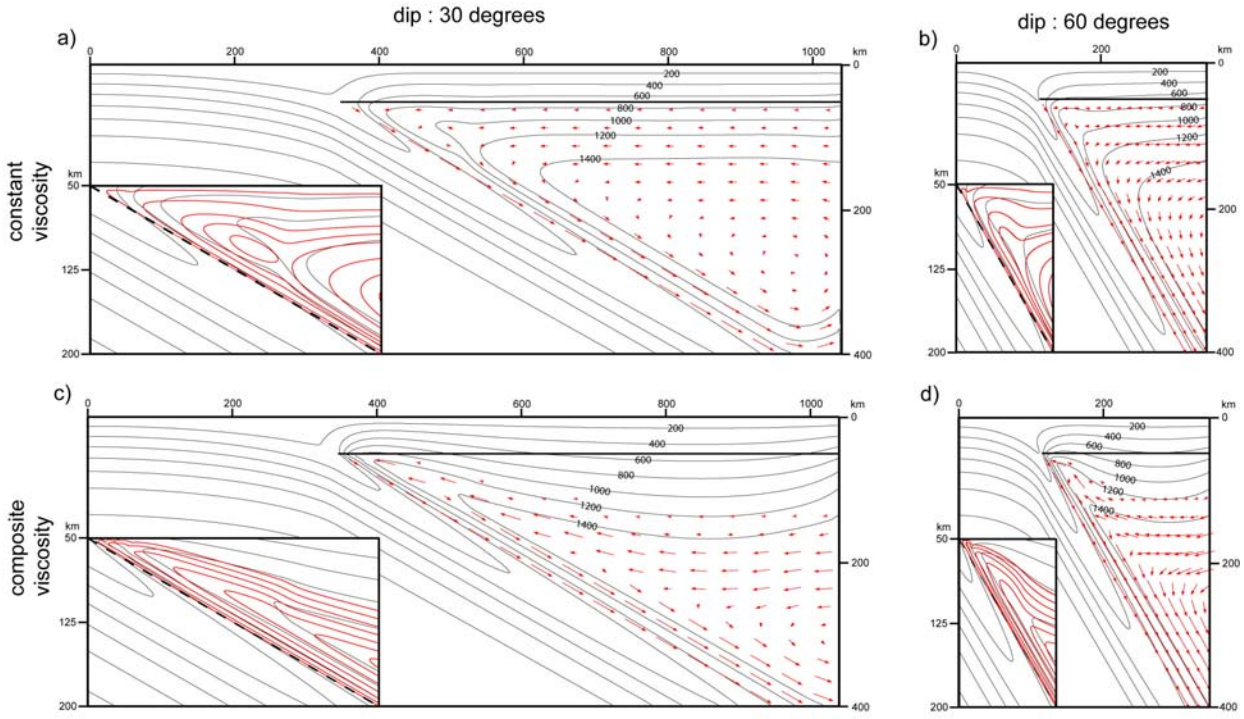

Temperature and flow structures in the mantle wedge in the ALA experiments using constant and composite viscosity with 30 and 60 degree dips of the subducting slab. Velocity of 5cm/year is used for the velocity of the subducting slab. The horizontal thick solid line at the 50 km depth indicates the bottom of the overlying lid. The diagonal velocity vectors along the base of the mantle wedge correspond to the imposed surface velocity of the subducting slab. Length of the vector corresponds to the magnitude of velocity. The figures in the small boxes illustrated at the left-bottom show the detailed temperature and flow in the low viscosity zone (serpentinite and wet olivine zones) using tracer-lines. Diagonal dashed lines in the small boxes represent the top of the subducting slab.

Figure 2.10

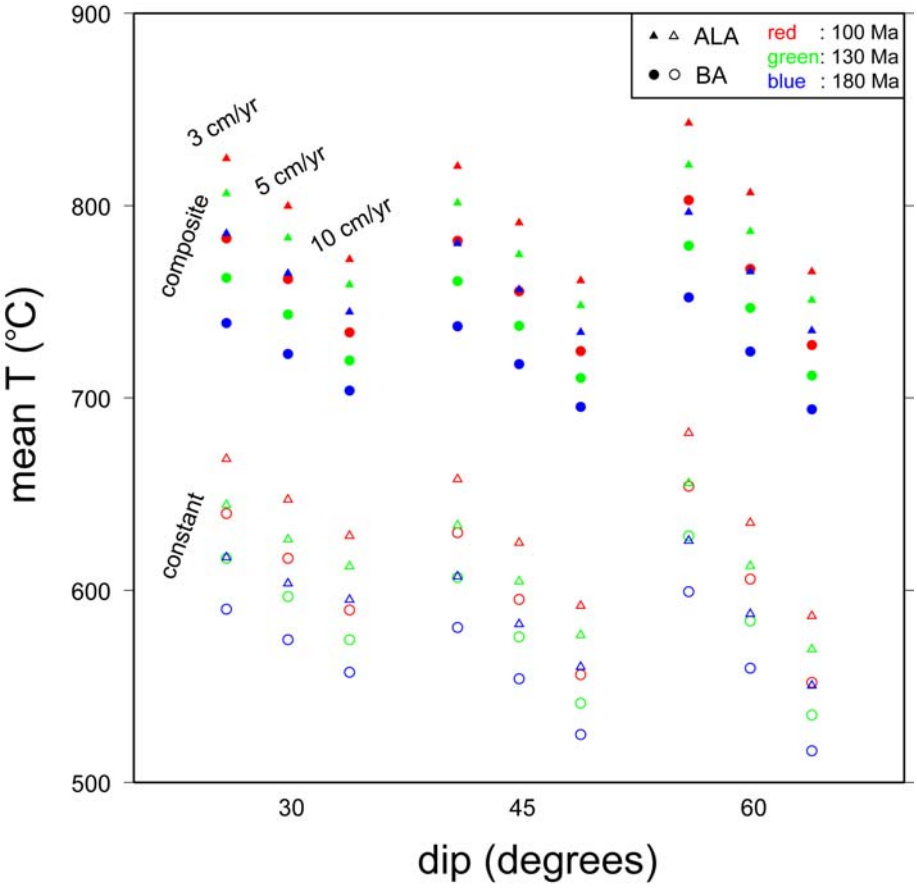

Mean temperatures of the top of the subducting slabs. Each mean temperature is calculated by summing temperatures of the nodal points corresponding to the top of the subducting slab and dividing the sum with the quantity of the nodal points (201). Triangle and circle correspond to the ALA and BA experiments, respectively. Red, green and blue colors correspond to 100, 130 and 180 Myr old subducting slabs, respectively. Filled and void symbols correspond to composite and constant viscosity, respectively.

Figure 2.11

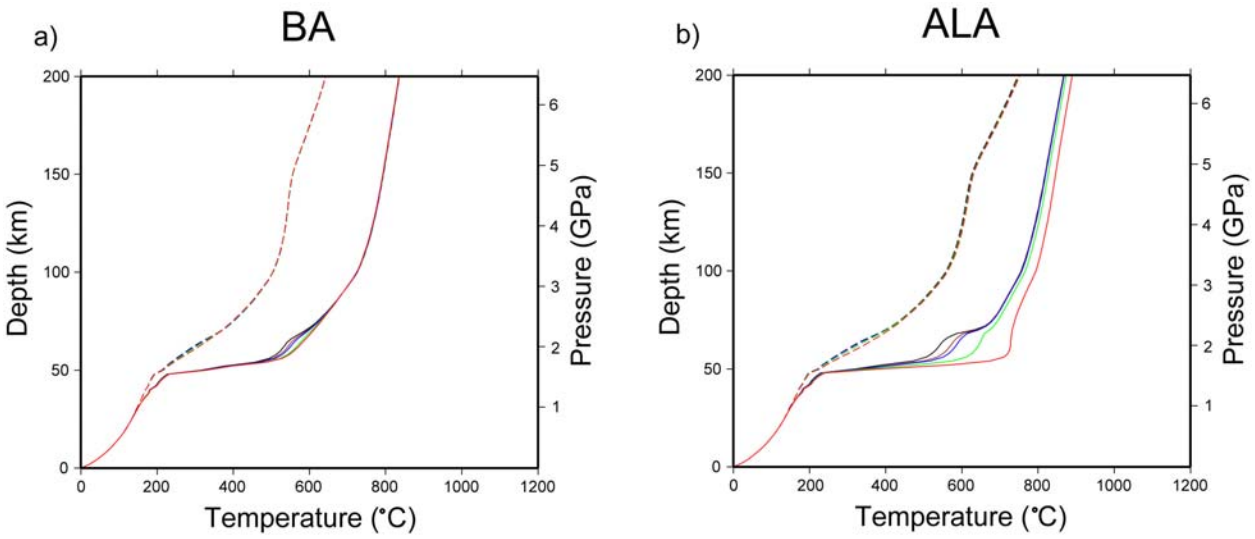

Pressure versus temperature paths for the top of the subducting slab with variations of viscosity reduction number for serpentinite zone. The BA (a) and ALA (b) experiments using constant and composite viscosity are illustrated separately for clarity. Dashed and solid lines represent the experiments using constant and composite viscosity, respectively. Black, brown, blue, green and red colors are corresponding to viscosity reduction numbers for serpentinite zone: 0.0001, 0.0005, 0.001, 0.01 and 0.05, respectively.

Figure 2.12

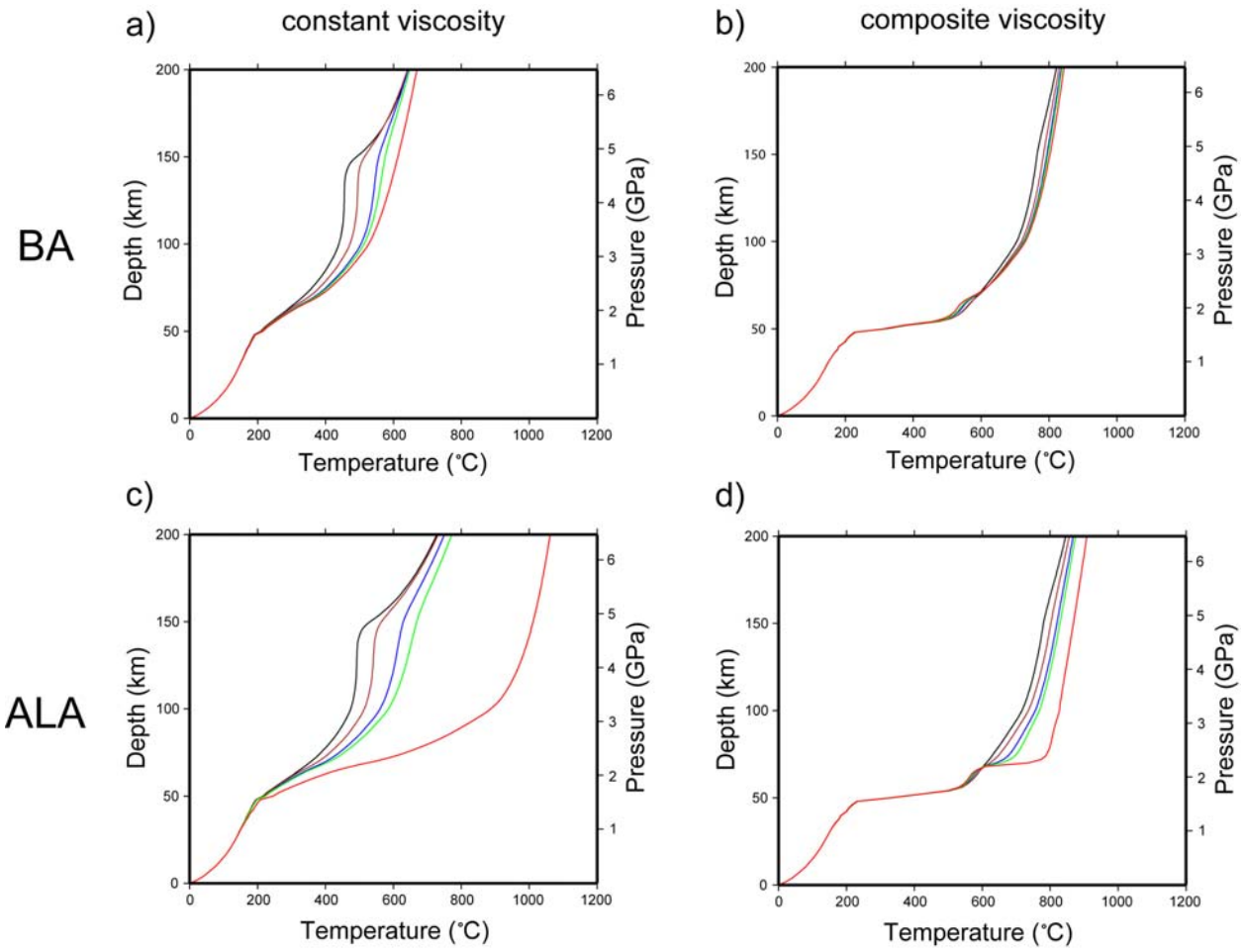

Pressure versus temperature paths for the top of the subduction slab with variations of viscosity reduction number for wet olivine zone: the BA and ALA experiments using constant and composite viscosity. For clarity, the paths corresponding to constant and composite viscosity are illustrated separately. Black, brown, blue, green and red colors are corresponding viscosity reduction numbers for wet olivine zone: 0.001, 0.01, 0.05, 0.1 and 1, respectively.

Figure 2.13

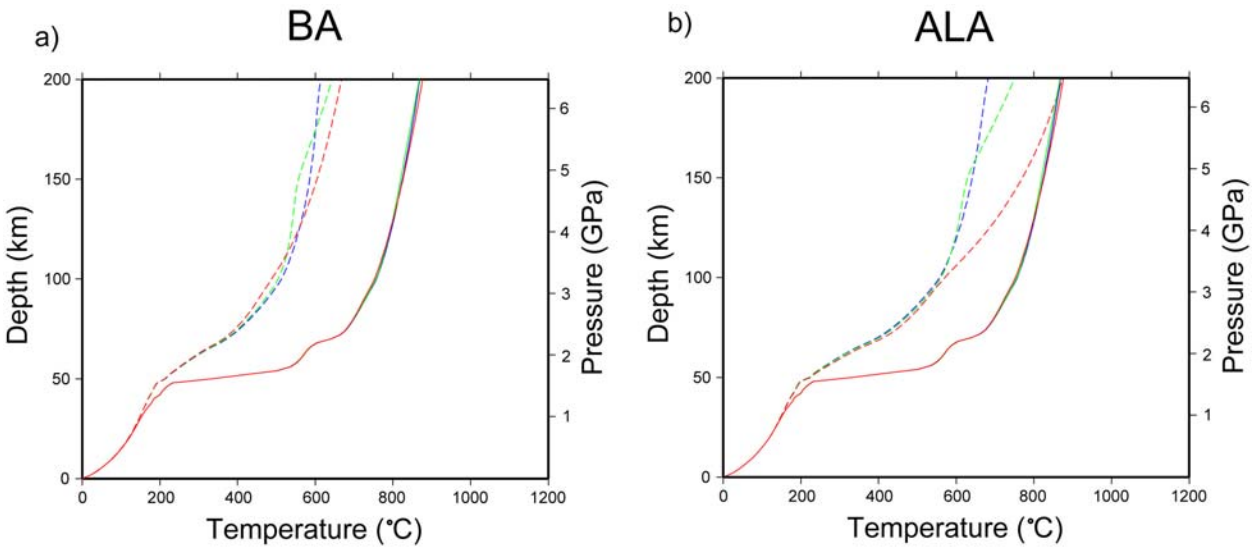

Pressure versus temperature paths for the top of the subduction slab by changing the region of wet olivine zone: small (red), intermediate (green) and large (blue). The BA (a) and ALA (b) experiments using constant (dashed lines) and composite (solid lines) viscosity are illustrated separately.

Figure 2.14

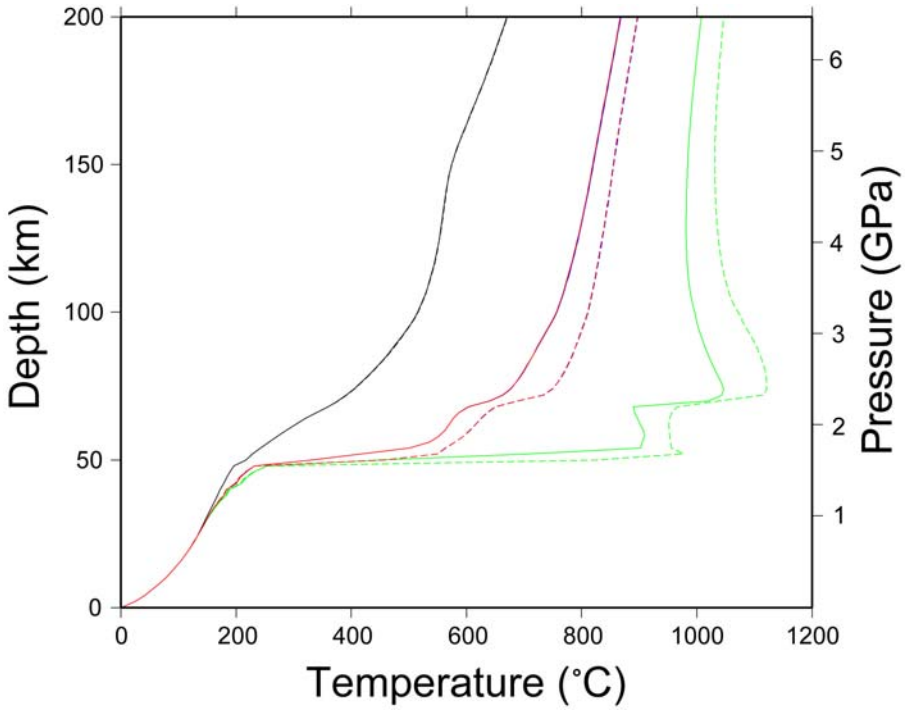

Pressure versus temperature paths for the top of the subduction slab for the ALA experiments with consideration of the half rigid and half fluid elements in the calculation of viscous dissipation: no consideration (solid lines) and consideration (dashed lines). Black, green, blue and red colors correspond to constant viscosity, diffusion creep, dislocation creep and composite viscosity, respectively. In the experiments using constant viscosity, the half rigid and half fluid elements produce negligible differences in the slab temperature.

Appendix

2.A1. Effects of grid resolution and the Picard solver

The effect of grid resolution on the thermal and flow structures of the subduction zones is evaluated by using 600 by 400 four-node quadrilateral elements (each element size: 1 by 1 km). We use the dip of 45 degrees, 130 Myr old lithosphere and velocity of 5 cm/year of the subducting slab without radiogenic heat production and compressibility (BA experiments only) for simplicity of the evaluation. Details of the effect of grid resolution with other parameters such as variations of dip, age and velocity of the subducting slab with compressibility could be the subject of the future studies. We use the Picard solver to calculate the energy equation here. The Picard solver attains the converged temperature and flow fields very fast compared with the explicit solver but, we encountered numerical difficulties in the ALA experiments using diffusion creep viscosity. In the BA experiments using the 300 by 200 element mesh, there is a very good agreement in the results calculated by using the Picard and explicit solvers. The BA experiments using constant viscosity produce no differences in temperature and the experiments using pressure and temperature dependent viscosity only produce differences in temperature within 0.30 ˚C, regardless of decoupling condition. Therefore, we assume that the Picard solver can calculate the thermal and flow structures very well in the BA experiments. Figure A1 shows pressure versus temperature paths and differences in temperature of the top of the subducting slab between the BA experiments using 600 by 400 and 300 by 200 element meshes. In general, the heat from radiogenic materials systematically shifts the slab temperature; see Figure 8a. In the experiments using the partially coupled zone, the finer grid decreases the slab temperature, most noticeably, at the base of the mantle wedge in the experiments using composite viscosity and dislocation creep, implying that grid resolution affects the mantle rheology and temperature and flow structures in the corner of the mantle wedge. These differences in temperature are still smaller than the differences by variations of age and velocity of the subducting slab and rheology (Figure 10). In contrast to the experiments using a partially coupled zone, a fully coupled zone with finer grid produces higher slab temperature. Similar to those in the experiments

using a partially coupled zone, larger differences in temperature are concentrated in the corner of the mantle wedge. These observations imply that 1) a proper treatment of singularity (abrupt changes in the slab velocity) at the tip and grid resolution in the corner of the mantle wedge are important experimental factors in the models of the subduction zones, consistent with previous experiments [*van Keken et al.*, 2002; 2008] and 2) a proper implementation of decoupling condition is also important in the BA experiments as well as the ALA experiments.

Figure 2.A1.

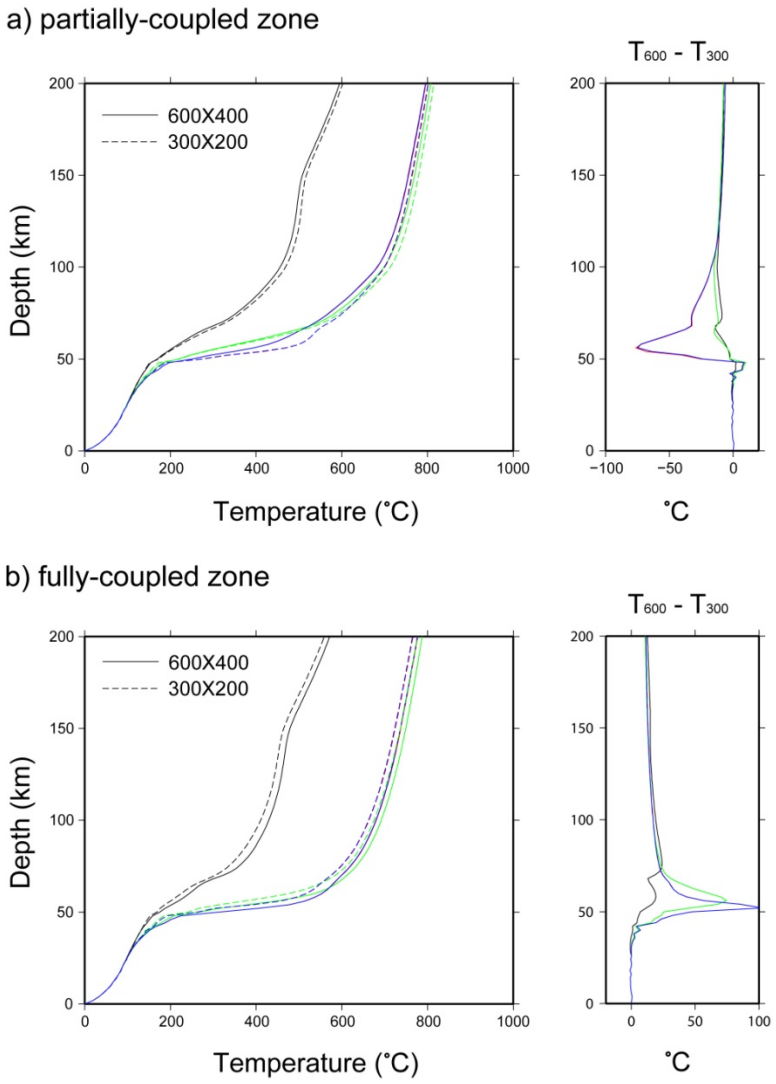

Pressure versus temperature paths and differences in temperature of the top of the subducting slab in the BA experiments using 600 by 400 and 300 by 200 element meshes. Black, green, blue and red colors correspond to constant viscosity, diffusion creep, dislocation creep and composite viscosity, respectively. The differences in temperature of the top of the subducting slab between 600 by 400 and 300 by 200 element meshes are calculated by subtracting the top temperatures of 300 by 200 experiments from those of 600 by 400 experiments. As described in results and discussion, there is a very good agreement in pressure versus temperature paths between the experiments using composite viscosity and dislocation creep.

Chapter 3

Why are high-Mg# andesites widespread in the western Aleutians? A numerical model approach *

Abstract

High-Mg# andesites are thought to be derived from partial melting of subducting oceanic basalts. Slab thermal modeling has shown that this requires a young (<25 Ma), very shallow (flat) slab and/or high shear stresses along the slab surface. These conditions currently do not exist in the Aleutian arc, the typical locality of high-Mg# andesites. Using kinematic-dynamic thermal models of subduction zone that include time-dependent age and subducting rate of the oceanic plate entering the trench since subduction initiation, we find that partial melting of the subducting oceanic basalts is restricted to the western Aleutians (from ~174° W to 195° W), consistent with the widespread occurrence of high-Mg# andesites in the western Aleutian arc. Our modeling suggests that consideration of temporal and spatial evolution of slab age and subducting rate along the Aleutian island arc is fundamental to the genesis of high-Mg# andesites in the western Aleutians.

Keywords: High-Mg# andesite, Aleutian island arc, Numerical model

* An edited version of this chapter was published by the Geological Society of America, Lee, C. and S. D. King, Why are high-Mg# andesites widespread in the western Aleutians? A numerical model approach, *Geology*, 38(7), 583-586

3.1 Introduction

High-Mg# andesites are observed in the arcs of southwest Japan, Central America, the Aleutians, Cascadia, New Guinea, and the Philippines and are considered essential to understand continent construction due to their similarity in compositions with continental crust (Gutscher et al., 2000; Kelemen et al., 2003b). Geochemical studies have attributed high-Mg# andesites to partial melting of subducting oceanic basalts (Kay, 1978; Kelemen et al., 2003b). In contrast to the evidence indicating partial melting of subducted sediments found in many subduction zones (Class et al., 2000, and references therein), high-Mg# andesites are mostly found in association with very young and/or shallow (flat) subducting slabs (Sdrolias and Müller, 2006; Syracuse and Abers, 2006). Calculations of slab and wedge thermal structure show that partial melting of subducting oceanic basalts is expected only in very young subducting slab (<25 Ma), in a shallow (flat) slab and/or in a slab with high shear stresses (~100 MPa) along the slab surface (Peacock et al., 1994; Peacock, 1996; Peacock and Wang, 1999; Gutscher et al., 2000).

While the high Mg# andesites found at many localities are consistent with the young and/or flat slab models, the genesis of high-Mg# andesites in the Aleutian island arc has been a puzzle ever since the first report of Adakite at Adak island and the western Aleutians (Kay, 1978; Yogodzinski et al., 1995; Kelemen et al., 2003b). Based on thermal modeling, a ~50 Ma old Aleutian slab is too cold for slab melting, and seismic tomographic models show no evidence of very shallow (flat) subduction in the Aleutians (Syracuse and Abers, 2006). Recent numerical models using temperature-dependent viscosity produce temperatures consistent with slab melting throughout the Aleutians (Kelemen et al., 2003a); however, high-Mg# andesites have only been found in the western Aleutians (Kelemen et al., 2003b). The present nearly uniform age of the incoming plate along the length of the Aleutian trench poses a problem for any steady-state models of slab thermal structure because of the difference in lava types found in the eastern and western Aleutians. Recent plate reconstruction shows that the age and rate of the incoming plate at the Aleutian trench has changed significantly with time (Sdrolias and Müller, 2006), suggesting the exploration of time-dependent subduction models. In this study, we use two-dimensional kinematic-

dynamic subduction models varying the age and rate of the incoming plate since subduction initiation. We find that when considering subduction history and time-dependent subduction parameters the generation of the high-Mg# andesites is restricted to the western Aleutians.

3.2 Numerical model

In order to consider the temporal and along-strike variations of the age and rate of the incoming plate, we formulated two representative two-dimensional models (Fig. 1) corresponding to the eastern and western Aleutians using recent plate reconstruction and seismic tomographic models (Sdrolias and Müller, 2006; Syracuse and Abers, 2006). The eastern and central Aleutians can be considered with one model because the age and rate of the incoming plate are comparable (Sdrolias and Müller, 2006). The two formulated models are similar to our previous models (van Keken et al., 2008; Lee and King, 2009); thus, we briefly describe the models here.

In both models, subducting slab is kinematically prescribed, and flow in the mantle wedge is calculated dynamically, excluding mantle buoyancy. To calculate mantle flow and thermal structures, we use the incompressible Boussinesq approximation implemented in ConMan (King et al., 1990) and include viscous dissipation in the additional experiments (King et al., 2010).

For the viscosity of the mantle wedge, we use a composite viscosity of diffusion and dislocation creep for dry olivine (Karato and Wu, 1993; Lee and King, 2009). Due to dehydration of the subducting slab, the mantle wedge above the slab will be hydrated (wet olivine), and to consider wet olivine rheology, we use a viscosity reduction factor of 0.05 multiplied by the composite viscosity (Honda and Saito, 2003; Lee and King, 2009). The termination depth of slab dehydration is dependent on the incoming slab temperatures (Schmidt and Poli, 1998); the extent of the hydrated mantle wedge could be varied with the termination depth. However, our preliminary experiments (not shown) show that the extent of the hydrated mantle wedge does not change slab temperatures significantly. Thus, we simply assume a 150 km depth as the termination depth of slab dehydration. Partial melting in the mantle wedge and

subducting slab should also decrease the mantle wedge viscosity (Hirth and Kohlstedt, 2003); however, this effect is not considered initially.

Two domains of 200 km (depth) by 252 km (from the trench to the backarc) and 200 by 400 km are formulated for the western and eastern Aleutians, respectively (Figs. 1B and 1C). Although the dip angle of the subducting slab varies along the Aleutian arc, averaged dip angles of 45° and 60° are used for the eastern and western Aleutians, respectively (Syracuse and Abers, 2006). The thickness of the overriding rigid crust is 30 km (Holbrook et al., 1999), and a typical value of radiogenic heat production of 3.0×10^{-12} W/kg is used for the oceanic plate to 10 km depth. Previous studies show that the mantle flow at the tip of the mantle wedge is suppressed (e.g., Currie et al., 2004; Wada et al., 2008) and we approximate the suppressed mantle flow by using a vertical boundary crossing the slab surface at 50 km depth.

To represent the time-dependent slab age and subducting rate, we estimate the incoming plate age (rate) every 10 (5) Ma at the 1000 (western Aleutians) and 2500 km (eastern Aleutians) from the west end of the Aleutian arc (Sdrolias and Müller, 2006). The age and rate of the subducting slab are approximated by piecewise polynomials, though simpler approximations could bear the distinct differences in the temporal age and rate between the eastern and western Aleutians (Figs. 2A and 2B). The velocity of the subducting slab is oblique to the trench, especially in the western Aleutians, and we use the component of velocity perpendicular to the trench in our models. The half-space cooling model is used to calculate the temperature profile of the incoming and overriding plate (Stein and Stein, 1992). For simplicity, the cooling model is extended to the 200 km depth where temperature is assumed to be 1400 °C. The age of the overriding lithosphere is held constant (50 Ma) through time. The temperature profile and subducting rate of the incoming plate are updated each time step at the trench (the left side of the model domain).

3.3 Results

Figure2 shows the slab age and subducting rate as a function of time (Figs. 2A and 2B) and depth versus temperature curves (Figs. 2C and 2D) of the subducting oceanic basalts covered by uniform thickness of sediments corresponding to the eastern and western Aleutians. Compared with the sediment thickness (>1 km) subducted along the Cascadia and Sumatra trenches, the subducted sediments along the Aleutian arc are relatively thin: ~350 m for the eastern and central Aleutians, and from ~100 to 200 m for the western Aleutians (Plank and Langmuir, 1998). Because the thickness of the sediments is comparable to the model element size (Figs. 1B and 1C), we use the temperature curves corresponding to the minimum depth of ~440 and 320 m from the slab surface for the eastern and western Aleutians, respectively.

The depth versus temperature plots for the eastern Aleutians with the incompressible model show little variation in slab temperatures through time (Fig. 2C). To reflect the uncertainty of wet basalt solidus, we plot two end-member solidi of wet basalt (Schmidt and Poli, 1998; Kessel et al., 2005). Except for the early Miocene (~20 Ma), none of the depth versus temperature curves intersect the two wet basalt solidi, indicating that no slab melting occurs through time in the eastern Aleutians. However, there is extensive slab melting in the western Aleutians if the low end-member solidus of wet basalt is considered (Fig. 2D). We expect results similar in the eastern and central Aleutians due to the similarities of age and rate of the incoming plate. Our results are consistent with previous geochemical studies (Kay and Kay, 1994; Class et al., 2000; George et al., 2003); the slab temperatures exist between the solidi of pelagic sediments and wet basalt (650-740 °C at 3 GPa) during Tertiary, which creates partial melting of the sediments except for underlying oceanic basalts under the central Aleutians such as Umnak island.

Incompressible calculations including viscous dissipation also show a variation in the style of slab melting along the Aleutian arc (not shown). As results of heat generated by viscous dissipation, the thermal boundary layer on the subducting slab becomes thinner than in otherwise similar incompressible models (Lee and King, 2009) and slab melting is expected throughout the whole arc. However, there is significantly less slab melting in the eastern and central Aleutians compared with the western Aleutians because depth versus temperature curves corresponding to the eastern Aleutians still slightly cross the low

end-member solidus. If the high end-member solidus of wet basalt is considered, there is limited partial melting of the oceanic basalts during Miocene in the eastern and central Aleutians. However, regardless of the solidi, partial melting of the oceanic basalts occurs through time in the western Aleutians. The extensive melting along the western Aleutians is consistent with the widespread occurrence of high Mg# andesites in the western Aleutians during Miocene and Quaternary (Kay, 1978; Yogodzinski et al., 1995; Kelemen et al., 2003b; Jicha et al., 2004).

Recent numerical and laboratory analyses (Hirth and Kohlstedt, 2003; Kelemen et al., 2003a) suggest that the effective viscosity of the mantle wedge is even smaller (from ~10^{17} to 10^{18} Pa.s) than previously considered (e.g., Billen and Gurnis, 2001) and the value used in the models in Figure 1 (from ~10^{18} to 10^{20} Pa.s). To address the influence of the smaller mantle wedge viscosity, we conduct the additional experiments by reducing the activation energy of olivine by 10%, resulting in the mantle viscosity an order of magnitude smaller (not shown). Although we do not consider wedge melting, this smaller mantle viscosity could be a crude estimation of the effect of wedge melting on the mantle viscosity. In this case, the slab temperatures slightly decrease due to the strengthened isolated corner flow at the corner of the mantle wedge (Lee and King, 2009), consistent with Kelemen et al. (2003a). This indicates that wide ranges of temperature- and pressure-dependent mantle viscosity can generate partial melting of the subducting slab, as pointed out by Kelemen et al. (2003a).

3.4 Discussion

Differing from our interpretation, Kelemen et al. (2003b) suggest that partial melting of the oceanic basalts occurring throughout the whole arc is obscured by mixing with partial melting of the mantle wedge except for the western Aleutians where lesser wedge melting due to lower mantle wedge temperatures does not obscure the slab melting significantly. To distinguish between these interpretations, an estimate of the amount of melt in the mantle wedge is crucial. The amount of melt in the mantle wedge is estimated by using the batch-melting calculation of Grove et al. (2006). To address the effect of lower

mantle temperatures, additional experiments were conducted by using the backarc mantle temperature of 100 °C lower (1300 °C) at 200 km depth for the western Aleutians. The extent of melt distributions in the mantle wedge has not significantly varied with time, compared with the current distribution since subduction initiation. The experiments using lower mantle temperature show reduced wedge melting (Figs. 3B versus Fig. 3C); however, the lower slab temperatures reduce slab melting significantly, making these results difficult to reconcile with the widespread occurrence of high-Mg# andesites. Therefore, partial melting in the mantle wedge would be extensive throughout the whole arc (Figs. 3A and 3B).

If partial melting in the mantle wedge is extensive throughout the whole arc, why are high-Mg# andesites observed in the western Aleutians without evidence of significant mixing with melts from the mantle wedge, which obscures slab melting? Gaetani and Grove (2003) estimate that the speed of ascending melts through porous flow is much higher than the solid-state flow of the mantle wedge. If the slab and wedge melts ascend very fast, the melts may erupt without significant mixing. Another possible explanation is related to the wet peridotite solidus of Grove et al. (2006), which is one of the lowest solidi. If we use the solidus from Schmidt and Poli (1998), wedge melting and mixing will be reduced.

As described above, the numerical models suggest that slab melting is restricted to the western Aleutians and does not occur throughout the entire Aleutian arc. However, it is worth noting that our interpretation is not unique, and several caveats need to be considered.

First, three-dimensional temporal dynamic slab evolution is not considered. Seismic tomographic models indicate the presence of a large slab window in the westernmost Aleutians, which may be due to slab tearing during Miocene (Levin et al., 2005). Rollback and westward oblique subduction in the western Aleutians (Sdrolias and Müller, 2006) may cause lateral flow of hot mantle originating from the slab window (Levin et al., 2005). This hot mantle flow could thin the thermal boundary layer and increase the slab temperature, resulting in extensive slab melting in the western Aleutians. In addition, constant slab dip used in our modeling may be a simple assumption. Using analog models, Guillaume et al. (2009) show that slab dip itself varies with time. These could be tested with three-dimensional fully dynamic subduction models.

Second, frictional shear heating along the slab surface is not considered in our modeling. Previous studies show that the magnitude of the shear stress is not well constrained; from ~0 to 100 MPa (Peacock, 1996 and references therein). However, even if frictional shear heating occurs along the slab surface, the heating would be relatively weak; extensive shear heating would increase the slab temperatures for the eastern Aleutians over the wet basalt solidus, inconsistent with the arc lava geochemistry (Class et al., 2000; George et al., 2003).

Third, a wet sediment solidus is poorly constrained. For instance, Johnson and Plank (1999) report a solidus of wet pelagic sediments higher than the wet basalt solidus (~100 °C higher at 100 km depth). However, unlike partial melting of the oceanic crust, which is restricted to the western Aleutians, partial melting of subducted sediments throughout the Aleutian arc is evident from geochemical data (Class et al., 2000; Kelemen et al., 2003b). Therefore, the wet sediment solidus in the Aleutian arc may be smaller or similar to the wet basalt solidus.

3.5 Concluding remarks

Time-dependent subduction models including varying slab age and subducting rate show that melting of the subducting oceanic basalts responsible for high-Mg# andesites is restricted to the western Aleutians (from ~174° W to 195° W), consistent with the widespread occurrence of high-Mg# andesites in the western Aleutians. Time-dependent subduction parameters provide a consistent interpretation along the Aleutian arc without requiring processes that obscure slab melting in the eastern Aleutians. Three-dimensional fully dynamic subduction models including advanced mantle rheology and melt evolution will improve understanding of the Aleutian arc magmatism.

References

Billen, M.I., and Gurnis, M., 2001, A low viscosity wedge in subduction zones: *Earth and Planetary Science Letters*, v. 193, p. 227–236, doi: 10.1016/S0012-821X(01)00482-4.

Gaetani, G.A., and Grove, T.L., 2003, Experimental Constrains on Melt Generation in the Mantle Wedge, *in* Eiler, J., ed., *Inside the Subduction Factory*: Washington, D.C., American Geophysical Union, p. 107–134.

George, R., Turner, S., Hawkesworth, C., Morris, J., Nye, C., Ryan, J., and Zheng, S.-H., 2003, Melting processes and fluid and sediment transport rates along the Alaska-Aleutian arc from an integrated U-Th-Ra-Be isotope study: *Journal of Geophysical Research*, v. 108(B5), doi:10.1029/2002JB001916

Class, C., Miller, D.M., Goldstein, S.L., and Langmuir, C.H., 2000, Distinguishing melt and fluid subduction components in Umnak Volcanics, Aleutian Arc: *Geochemistry Geophysics Geosystems*, v. 1, doi: 10.1029/1999GC000010.

Grove, T.L., Chatterjee, N., Parman, S.W., and Médard, E., 2006, The influence of H_2O on mantle wedge melting: *Earth and Planetary Science Letters*, v. 249, p. 74–89, doi: 10.1016/j.epsl.2006.06.043.

Guillaume, B., Martinod, J., and Espurt, N., 2009, Variations of slab dip and overriding plate tectonics during subduction: Insights from analogue modeling: *Tectonophysics*, v. 463, p. 167-174, doi:10.1016/j.tecto.2008.09.043

Currie, C.A., Wang, K., Hyndman, R.D., and He, J., 2004, The thermal effects of steady-state slab-driven mantle flow above a subducting plate: the Cascadia subduction zone and backarc: *Earth and Planetary Science Letters*, v. 223, p. 35–48, doi: 10.1016/j.epsl.2004.04.020.

Gutscher, M.-A., Maury, R., Eissen, J.-P., and Bourdon, E., 2000, Can slab melting be caused by flat subduction?: *Geology*, v. 28, p. 535–538, doi: 10.1130/0091-7613(2000)28<535:CSMBCB>2.0.CO;2.

Hirth, G., and Kohlstedt, D., 2003, Rheology of the Upper Mantle and the Mantle Wedge: A View from the Experimentalists, *in* Eiler, J., ed., *Inside the Subduction Factory*: Washington, D.C., American Geophysical Union, p. 83–105.

Holbrook, S.W., Lizarralde, D., McGeary, S., Bangs, N., and Diebold, J., 1999, Structure and composition of the Aleutian island arc and implications for continental crustal growth: *Geology*, v. 27, p. 31–34, doi: 10.1130/0091-7613(1999)027<0031:SACOTA>2.3.CO;2.

Honda, S., and Saito, M., 2003, Small-scale convection under the back-arc occurring in the low viscosity wedge: *Earth and Planetary Science Letters*, v. 216, p. 703–715, doi: 10.1016/S0012-821X(03)00537-5.

Jicha, B.R., Singer, B.S., Brophy, J.G., Fournelle, J.H., Johnson, C.M., Beard, B.L., Lapen, T.J., and Mahlen, N.J., 2004, Variable Impact of the Subducted Slab on Aleutian Island Arc Magma Sources: Evidence from Sr, Nd, Pb, and Hf Isotopes and Trace Element Abundances: *Journal of Petrology*, v. 45, p. 1845–1875, doi: 10.1093/petrology/egh036.

Johnson, M.C., and Plank, T., 1999, Dehydration and melting experiments constrain the fate of subducted sediments: *Geochemistry Geophysics Geosystems*, v. 1, doi: 10.1029/1999GC000014.

Karato, S.-I., and Wu, P., 1993, Rheology of the upper mantle: a synthesis: *Science*, v. 260, p. 771–778, doi: 10.1126/science.260.5109.771.

Kay, R.W., 1978, Aleutian magnesian andesites: Melts from subducted Pacific ocean crust: *Journal of Volcanology and Geothermal Research*, v. 4, p. 117–132, doi: 10.1016/0377-0273(78)90032-X.

Kay, S.M., and Kay, R.W., 1994, Aleutian magmas in time and space, *in* Plafker, G., and Berg, H.C., eds., *The Geology of Alaska*: Boulder, Colorado, Geological Society of America, V. G-1, p. 687-722.

Kelemen, P.B., Rilling, J.L., Parmentier, E.M., Luc, M., and Hacker, B.R., 2003a, Thermal structure due to solid-state flow in the mantle wedge beneath arcs, *in* Eiler, J., ed., *Inside the Subduction Factory*: Washington, D.C., American Geophysical Union, p. 293–311.

Kelemen, P.B., Yogodzinski, G.M., and Scholl, D.W., 2003b, Along-strike variation in the Aleutian island arc: Genesis of high Mg# andesite and implications for continental crust, *in* Eiler, J., ed., *Inside the Subduction Factory*: Washington, D.C. American Geophysical Union, p. 223–276.

Kessel, R., Ulmer, P., Pettke, T., Schmidt, M.W., and Thompson, A.B., 2005, The water-basalt system at 4 to 6 GPa: Phase relations and second critical endpoint in a K-free eclogite at 700 to 1400 °C: *Earth and Planetary Science Letters*, v. 237, p. 873–892, doi: 10.1016/j.epsl.2005.06.018.

King, S.D., Lee, C., van Keken, P.E., Leng, W., Zhong, S., Tan, E., Tosi, N., and Kameyama, M.C., 2010, A community benchmark for 2D Cartesian compressible convection in the Earth's mantle: *Geophysical Journal International*, v. 180(1), p. 73-87, doi: 10.1111/j.1365-246X.2009.04413.x

King, S.D., Raefsky, A., and Hager, B.H., 1990, Conman: vectorizing a finite element code for incompressible two-dimensional convection in the Earth's mantle: *Physics of the Earth and Planetary Interiors*, v. 59, p. 195–207, doi: 10.1016/0031-9201(90)90225-M.

Lee, C., and King, S.D., 2009, Effect of mantle compressibility on the thermal and flow structures of the subduction zones: *Geochemistry Geophysics Geosystems*, v. 10, doi: 10.1029/2008GC002151.

Levin, V., Shapiro, N.M., Park, J., and Ritzwoller, M.H., 2005, Slab portal beneath the western Aleutians: *Geology*, v. 33, p. 253–256, doi: 10.1130/G20863.1.

Nichols, G.T., Wyllie, P.J., and Stern, C.R., 1994, Subduction zone melting of pelagic sediments constrained by melting experiments: *Nature*, v. 371, p. 785–788, doi: 10.1038/371785a0.

Peacock, S.M., 1996, Thermal and petrological structure of subduction zones (overview), *in* Bebout, G. E., et al., ed., *Subduction: Top to Bottom*: Washington, D.C., American Geophysical Union, p. 119–134.

Peacock, S.M., Rushmer, T., and Thompson, A.B., 1994, Partial melting of subducting oceanic crust: *Earth and Planetary Science Letters*, v. 121, p. 227–244, doi: 10.1016/0012-821X(94)90042-6.

Peacock, S.M., and Wang, K., 1999, Seismic consequences of warm versus cool subduction metamorphism: Examples from southwest and northeast Japan: *Science*, v. 286, p. 937–939, doi: 10.1126/science.286.5441.937.

Plank, T., and Langmuir, C.H., 1998, The chemical composition of subducting sediment and its consequences for the crust and mantle: *Chemical Geology*, v. 145, p. 325–394, doi: 10.1016/S0009-2541(97)00150-2.

Schmidt, M.W., and Poli, S., 1998, Experimentally based water budgets for dehydrating slabs and consequences for arc magma generation: *Earth and Planetary Science Letters*, v. 163, p. 361–379, doi: 10.1016/S0012-821X(98)00142-3.

Sdrolias, M., and Müller, R.D., 2006, Controls on back-arc basin formation: *Geochemistry Geophysics Geosystems*, v. 7, doi: 10.1029/2005GC001090.

Stein, C.A., and Stein, S., 1992, A model for the global variation in oceanic depth and heat flow with lithospheric age: *Nature*, v. 359, p. 123–129, doi: 10.1038/359123a0.

Syracuse, E.M., and Abers, G.A., 2006, Global compilation of variations in slab depth beneath arc volcanoes and implications: *Geochemistry Geophysics Geosystems*, v. 7, doi: 10.1029/2005GC001045.

van Keken, P.E., Currie, C., King, S.D., Behn, M.D., Cagnioncle, A., He, J., Katz, R.F., Lin, S.-C., Parmentier, E.M., Spiegelman, M., and Wang, K., 2008, A community benchmark for subduction zone modeling: *Physics of The Earth and Planetary Interiors*, v. 171, p. 187-197. doi:10.1016/j.pepi.2008.04.015

Wada, I., Wang, K., He, J., Hyndman, R.D., 2008, Weakening of the subduction interface and its effects on surface heat flow, slab dehydration, and mantle wedge serpentinization: *Journal of Geophysical Research*, v. 113, B04402, doi:10.1029/2007JB005190.

Wessel, P., and Smith, W.H.F., 1991, Free software helps map and display data: *Eos*, Transactions, American Geophysical Union, v. 72, p. 441, doi: 10.1029/90EO00319.

Yogodzinski, G. M., Kay, R. W., Volynets, O. N., Koloskov, A. V., Kay, S. M., 1995, Magnesian andesite in the western Aleutian Komandorsky region: Implications for slab melting and processes in the mantle wedge: *Geological Society of America Bulletin*, v. 107, p. 505-519, doi: 10.1130/0016-7606(1995)107<0505:MAITWA>2.3.CO;2

Figure 3.1

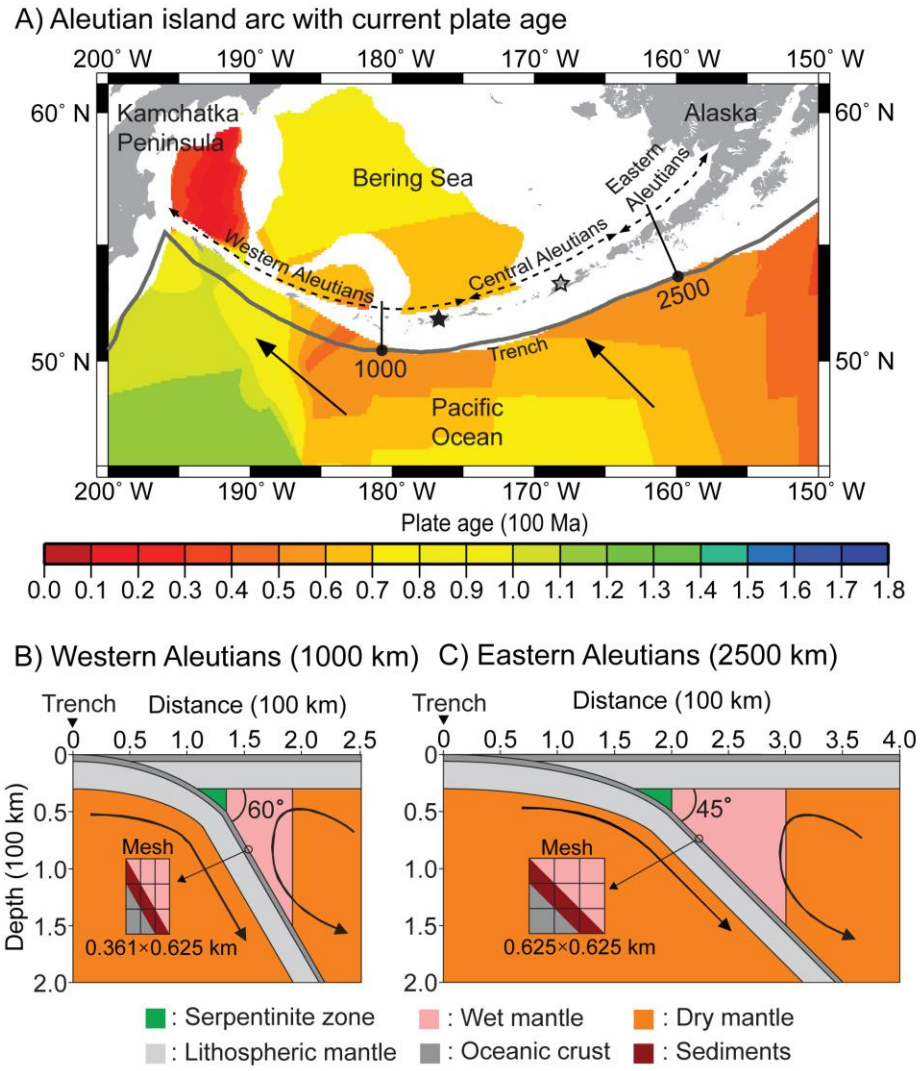

Schematic map of the Aleutian island arc and representative models for the western and eastern Aleutians. The classification of Aleutians and current plate age are based on Kelemen et al. (2003b) and Sdrolias and Müller (2006), respectively. Two subduction models (B and C) for western and eastern Aleutians correspond to the lines marked 1000 and 2500, respectively (the distance in kilometers from the west end of the Aleutian arc). The arrows on the Pacific plate indicate the direction of the subducting Pacific plates relative to the trench. The boxes labeled 'Mesh' show the element size and environment near the slab surface. The locations of Adak and Umnak islands are represented by the filled and open stars, respectively.

Figure 3.2

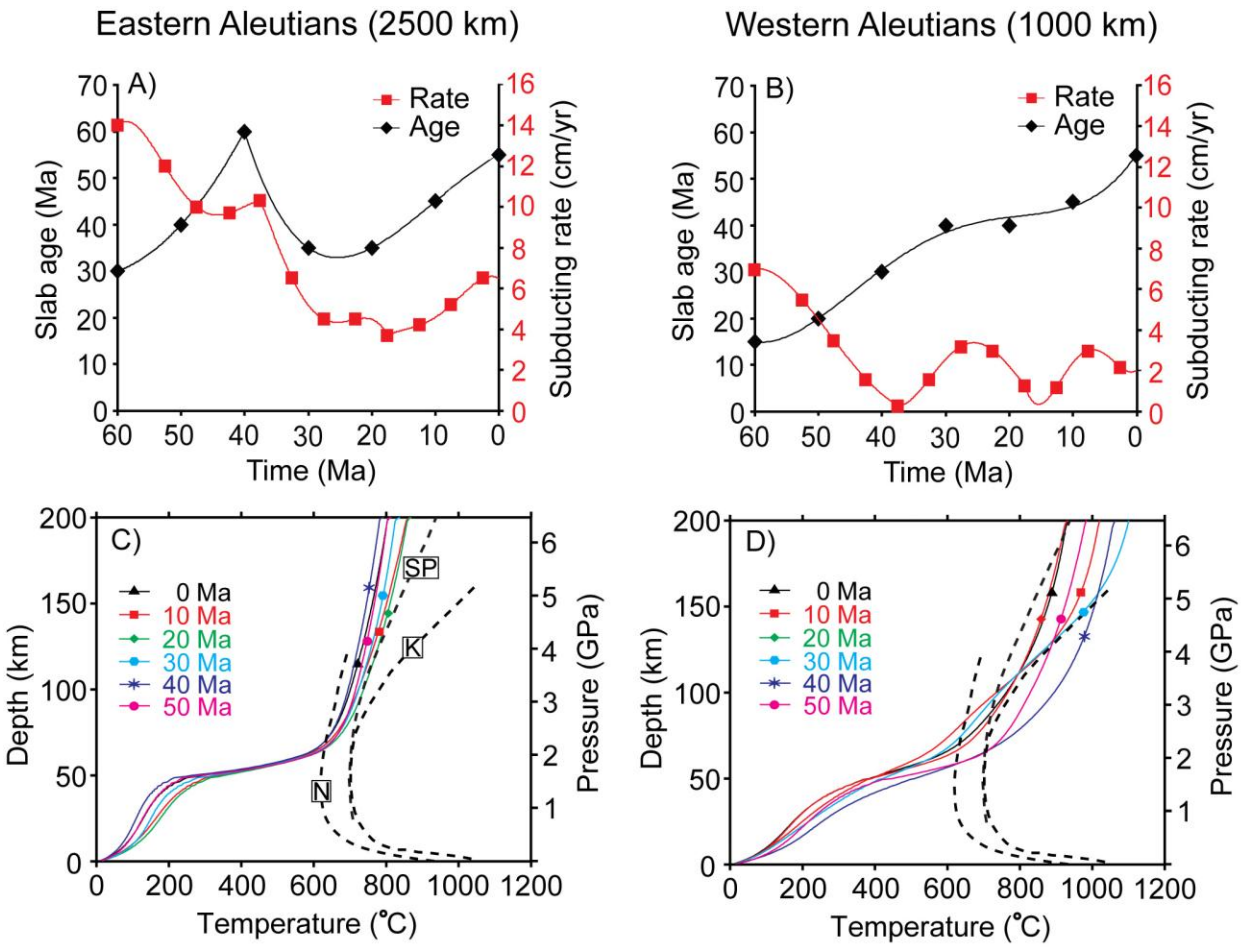

Varying slab age and subducting rate of the incoming plate at the trench (A and B) and depth versus temperature curves (C and D) corresponding to the eastern and western Aleutians using the incompressible model without viscous dissipation. The black diamonds and red squares correspond to the estimated slab age and rate every 10 and 5 Ma, respectively (see the text for details). Piecewise polynomials (a fourth-order polynomial for the age in B) are used to approximate age and rate. The dashed lines labeled with SP, K and N in C and D correspond to the low (Schmidt and Poli, 1998), high (Kessel et al., 2005) end-member solidi of wet basalt and the solidus (Nichols et al., 1994) of wet pelagic sediments, respectively.

Figure 3.3

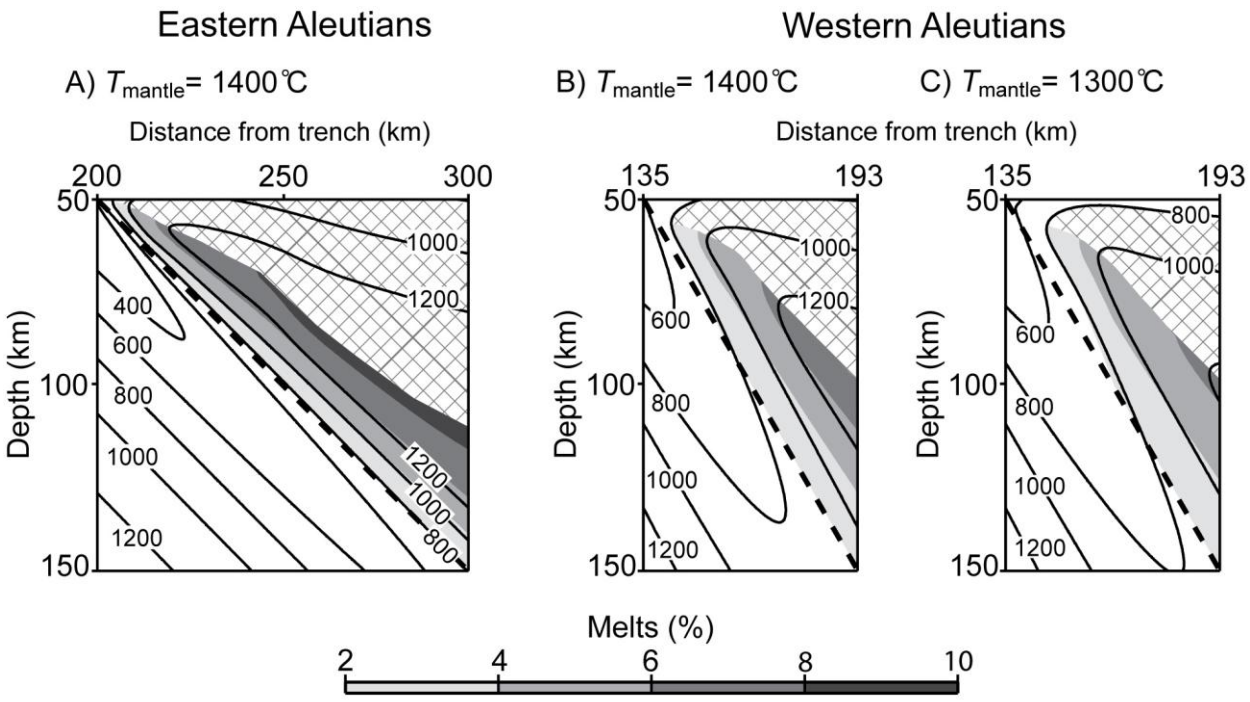

Melt distribution in the mantle wedge using the melt calculation of Grove et al. (2006) and using the incompressible model experiments with viscous dissipation. C: Melt distribution corresponding to lower mantle temperatures (see the text for details). The dashed lines are the slab surface, and the unit of temperature is Celsius. The hatched regions correspond to decreasing temperatures with decreases in depth, where melt distribution is described qualitatively only.

Chapter 4

Effect of slab buckling on subduction history and its implications *

Abstract

Recent seismic tomography images show apparent thickening of the subducted slab in shallow lower mantle. Analysis using the scaling laws for buckling of descending fluid indicates that buckling resulting from lateral slab deformation across the 660 km discontinuity is consistent with the seismic tomography images. However, the influence of complex dynamic subduction on the slab buckling has not been evaluated from the conditions used for the derivation of the scaling laws. Therefore, we formulate 2-D dynamic subduction experiments and evaluate the validity of the scaling laws by varying the viscosity increase across the 660 km discontinuity, effective slab strength, Clapeyron's slope of the phase transitions, side-wall boundary conditions and compressibility. Our calculations show that more cycles of periodic slab buckling develops by larger viscosity increases across the 660 km discontinuity, smaller effective slab strength, phase transitions, reflecting boundary conditions. The effect of compressibility on slab buckling is relatively minor. Periodic slab buckling results in periodic variations of convergence rate and dip of the subducting slab. Despite the complex dynamic subduction, the scaling laws predict slab buckling period and amplitudes within error of 20%. Periodic slab buckling has important implications in geology. The periodic convergence rate is consistent with time-dependent seafloor spreading at the mid-ocean ridge and convergence rate at the trench constrained by plate reconstruction. In addition, the alternating migration of arc volcanoes in the Andes can be correlated with the observed alternating dip of the subducting slab developed by slab buckling. Our calculations and geological evidence imply the periodic slab buckling is a natural expression of Earth's subduction.

Keywords: Slab buckling, Numerical model, Subduction zone

* This work will be submitted to Journal of Geophysical Research

4.1 Introduction

Subduction zones are a fundamental component of Earth's dynamic surface and play important roles in Earth's thermal and chemical evolution, plate tectonics, heat budget, and recycle of volatiles [e.g., *Stern*, 2002; *Elliott*, 2003; *van Keken*, 2003; *King*, 2007]. Because subduction zones are not directly accessible, diverse geophysical observations contributes to our understanding of subduction zones. Recent seismic tomography images show that apparent thickening of the subducted slab in shallow lower mantle is not due to limited resolution but indicates real slab structures [*Fukao et al.*, 2001; *Karason and van der Hilst*, 2001; *Ren et al.*, 2007]. The amount of thickening of the subducted slab at a depth of ~1200 km is around five times the thickness of the subducting oceanic lithosphere. Slab thickening caused by the slowly descending slab due to increasing viscosity with depth is inconsistent with the observed slab thickening [*Gurnis and Hager*, 1988; *Gaherty and Hager*, 1994; *Billen and Hirth*, 2007]. Instead, slab buckling resulting from lateral deformation of the subducting slab in the shallow lower mantle is attributed to the observed slab thickening in the tomographic images. Laboratory and numerical experiments have successfully generated extensive slab buckling in the shallow lower mantle, indicating that the slab buckling is consistent with the seismic observations [*Gaherty and Hager*, 1994; *Guillou-Frottier et al.*, 1995; *Christensen*, 1996; *Behounková and Cízková*, 2008].

Buckling of fluid descending onto a rigid plate has been studied through theoretical, analog and numerical experiments for decades [e.g., *Taylor*, 1968; *Griffiths and Turner*, 1988; *Tome and McKee*, 1999; *Ribe*, 2003]. The scaling laws derived from numerical experiments have been successfully applied to predict the slab buckling in the Middle America and Java subduction zones [*Ribe et al.*, 2007]. However, the scaling laws were derived by using the simplified numerical experiments: It is not clear how applicable they will be to more complex subduction experiments. The scaling laws rely on the experiments with 1) a kinematically injected fluid, whereas subduction is driven by buoyancy and may

not have a constant mass flux, 2) an incompressible homogeneous fluid, whereas slabs experience phase transitions and compression, 3) a symmetrically descending fluid from the slot, whereas slabs asymmetrically subduct at the trench and 4) a negligible viscosity of the ambient fluid around the descending fluid, whereas slabs are surrounded by highly viscous upper mantle. Among these assumptions, the limitations associated with 3 and 4 could be resolved because the scaling laws are valid for slanting fluid and large viscosity contrasts ($\eta_{slab}/\eta_{uppermantle} > 100$) between the upper mantle and subducting slab do not significantly affect slab deformation [*Ribe et al.*, 2007]. Thus, we evaluate whether the scaling laws are valid for Earth's subduction carrying the limitations associated with1 and 2.

Although time-dependent slab buckling has been identified in previous studies [*Christensen*, 1996; *Enns et al.*, 2005; *Behounková and Cízková*, 2008], a consequence of slab buckling on the convergence rate of the oceanic plate at the trench and slab morphology in the mantle has not been evaluated during the entire subduction life cycle (initiation, self-sustaining period and cessation). Dynamic evolution of the subducting slab is controlled by numerous subduction and mantle parameters; however, the conditions necessary for the slab buckling mode have not been mapped out. In addition, most subduction experiments are based on an incompressible mantle formulation and studies examining the effect of compressibility on mantle convection are rare [e.g., *Jarvis and McKenzie*, 1980; *Leng and Zhong*, 2008; *Lee and King*, 2009]. Thus, the purpose of this study is to quantitatively evaluate the effect of selected subduction and mantle parameters on slab buckling including; viscosity increase across the 660 km discontinuity (upper-lower mantle boundary), slab strength (viscosity), phase transitions in the mantle and slab, side-wall boundary conditions (reflecting/flow-through) and compressibility. We first present details of the numerical model formulation with relevant mantle and subducting slab parameters. We then evaluate the effect of each parameter on the slab buckling and the validity of the scaling laws derived by Ribe (2003) for our subduction models. Our calculations show that the slab buckling is generally consistent with the scaling laws (errors < 20 %) unless trench migration is significant. In addition, we show that a natural expression of Earth's subduction is periodic variations of convergence

rate and dip of the subducting slab. Then we compare our findings with geological observations. We show that the slab buckling in our calculations is consistent with the time-dependent mid-ocean spreading rate [*Cogné and Humler*, 2004], convergence rate of the oceanic plate at trench [*Sdrolias and Müller*, 2006] and alternating migration of the arc volcanoes [*Kay et al.*, 2006].

4.2 Numerical Models.

4.2.1 Governing equation and reference states

Although the governing equations and related parameters are described in several previous studies [*Jarvis and McKenzie*, 1980; *Ita and King*, 1994; *Schubert et al.*, 2001; *King et al.*, 2010], we briefly describe the governing equations and parameters here. The governing equations of the mantle convection with phase transitions can be defined below,

$$0 = \nabla \cdot (\rho \vec{v}), \qquad \text{- } \textit{continuity equation} \qquad (1)$$

$$0 = -\nabla P + \rho \vec{g} + \nabla \cdot \underline{\tau}, \qquad \text{- } \textit{momentum equation} \qquad (2)$$

$$\rho C_P \frac{DT}{Dt} - \alpha \frac{DP}{Dt} = \nabla \cdot (k \nabla T) + \phi + \rho H + \rho T \frac{DS_L}{Dt}, \qquad \text{- } \textit{energy equation} \qquad (3)$$

where ρ is the density, t is the time, $\vec{v}$ is the velocity, P is the pressure, $\vec{g}$ is the gravitational acceleration, $\underline{\tau}$ is the deviatoric stress tensor, C_P is the heat capacity at constant pressure, α is the thermal expansivity, T is the temperature, k is the thermal conductivity, and H is the rate of radiogenic heat production. S_L is the entropy change related to the phase transitions. $\frac{D}{Dt}$ is the total derivative and ϕ is the viscous dissipation, which are described as,

$$\frac{D}{Dt} = \frac{\partial}{\partial t} + v_i \frac{\partial}{\partial x_i} \qquad \text{- } \textit{total derivative} \ (4)$$

$$\phi = 2\eta \dot{\varepsilon}_{ij} + \lambda \dot{\varepsilon}_{kk} \delta_{ij} \qquad \text{- } \textit{viscous dissipation} \ (5)$$

where η is the dynamic viscosity, $\dot{\varepsilon}_{ij}$ is the strain rate tensor, δ_{ij} is the Kronecker delta, λ is the second (bulk) viscosity corresponding to $\frac{2}{3}\eta$ or 0 for the compressible or incompressible fluids, respectively.

If the mantle is chemically homogeneous and motionless, then mantle density is only a function of pressure due to adiabatic compression [*Birch*, 1952]. However, phase transitions in the mantle prevent the use of the adiabatic mantle density approximation [*Birch*, 1952]. As a first-order approximation, we assume that the density increase due to phase transitions can be represented as a perturbation to the reference density analogous to the density perturbations resulting from thermal expansion/contraction and dynamic pressure. Therefore, the reference density profile can be expressed with the Adams-Williamson equation [*Birch*, 1952] and, the linear summation of the reference density and perturbations can be described as follows,

$$\rho = \bar{\rho}(\bar{P},\bar{T}) + \rho'(P',T',\Pi), \qquad \text{- } \textit{density} \text{ (6)}$$

$$T = \bar{T} + T', \qquad \text{- } \textit{temperature} \text{ (7)}$$

$$P = \bar{P} + P', \qquad \text{- } \textit{pressure} \text{ (8)}$$

where the overbar and prime represent the reference state and perturbation from the reference state, respectively. $\bar{\rho}$ is the reference density corresponding to the Adams-Williamson equation. The density perturbation (ρ') is a function of the dynamic pressure (P'), temperature perturbation (T') and phase transition (Π). For an incompressible mantle, the reference density is constant (ρ_0) throughout the mantle. With the assumption of constant gravitational acceleration (g_0) and thermal expansivity (α_0) and ignoring phase transitions, the net adiabatic temperature distribution ($\bar{T}$) and lithostatic pressure ($\bar{P}$) are defined below;

$$\bar{T} = T_{potential}\left(e^{\frac{Diz}{d}} - 1\right), \qquad \text{- } \textit{adiabatic temperature distribution} \text{ (9)}$$

$$\overline{P} = \rho_c g_0 H_T \Gamma \left(e^{\frac{Diz}{\Gamma d}} - 1 \right), \qquad \text{- } \textit{lithostatic pressure} \text{ (10)}$$

where $T_{potential}$ is the mantle potential temperature, d is the domain thickness, z is the depth. H_T and Γ are the temperature scale height of compressible mantle and the Grüneisen's parameter, defined as $\frac{C_p}{g_0 \alpha_0}$ and $\frac{\alpha_0 K_s}{\overline{\rho} C_p}$, respectively, and Di is the dissipation number, $\frac{\alpha_0 g_0 d}{C_P}$. Because the thermal boundary layer is thin when compared with the depth of the mantle, the mantle is nearly adiabatic and we can calculate the net adiabatic temperature distribution from the surface. For the incompressible mantle, $\overline{T}$ = 0 and $\overline{P} = \rho_c g_0 d$ because there is no adiabatic compression in the incompressible mantle. The density perturbation due to dynamic pressure, temperature and phase transitions can be expressed below:

$$\rho' = \overline{\rho} \left(\frac{P'}{K_T} - \alpha_0 T' + \pi_{410} \frac{\delta\rho_{410}}{\overline{\rho}_{410}} + \pi_{660} \frac{\delta\rho_{660}}{\overline{\rho}_{660}} \right), \qquad \text{- density perturbation (11)}$$

$$\pi = \frac{1}{2} \left[1 + \tanh \left(\frac{P - P_t - \gamma (T - T_t)}{\rho_0 g_0 d_L} \right) \right], \qquad \text{- progress function (12)}$$

where K_T is the isothermal bulk modulus, assumed a constant and interchangeable with K_S here. π_{410} and π_{660} are the progress functions [*Richter*, 1973] corresponding to the two major phase transitions in the mantle; from olivine to wadsleyite (~410 km depth) and from ringwoodite to perovskite plus magnesiowüstite (~660 km depth), respectively [*Akaogi et al.*, 1989; *Ito and Takahashi*, 1989; *Fei et al.*, 2004; *Akaogi et al.*, 2007]. P_t and T_t are the reference pressure and temperature where 50% of phase transitions are progressed, which are fixed in this study, γ is the Clapeyron slope of the phase transitions, d_L is the phase loop, $\delta\rho_{410}$ and $\delta\rho_{660}$ are the density increases across the phase transition zones, and $\overline{\rho}_{410}$ and $\overline{\rho}_{660}$ are the reference densities calculated from the Adams-Williamson equation corresponding

to 410 and 660 km depth, respectively. For the incompressible mantle, $\overline{\rho}$, $\overline{\rho}_{410}$, and $\overline{\rho}_{660}$ are reduced to a constant, ρ_0 and the dynamic pressure term, $P^{'}/K_T$ is neglected.

The entropy changes due to phase transitions can be approximated by using the Clausius-Clapeyron and volume-density relations [*Ita and King*, 1994], described below;

$$S_L = \pi\Delta S = \pi\left(-\gamma\frac{\delta\rho}{\overline{\rho}}\right). \qquad \text{- entropy change (13)}$$

To apply non-dimensionalization to the governing equations, we use the relations for the velocity, pressure, time and density, described below;

$$\nu = \frac{\kappa_0}{d},\ P = \frac{\eta_0\kappa_0}{d^2},\ t = \frac{d^2}{\kappa_0},\ \ \overline{\rho} = \rho_0\overline{\rho}^{'} \text{ and } \kappa_0 = \frac{k_0}{\rho_0 C_P}$$

where κ_0 is the thermal diffusivity and η_0 is the reference viscosity. By applying the non-dimensionalization and keeping the original descriptions for convenience, the governing equations are reduced to the Anelastic Liquid Approximation (ALA);

$$0 = \nabla\cdot(\overline{\rho}^{'}\vec{v}), \qquad \text{- } \textit{continuity equation} \qquad (14)$$

$$0 = -\nabla P^{'} + \frac{Di}{\Gamma_0}P^{'}\hat{g} - Ra\overline{\rho}^{'}\left[T^{'} - \frac{1}{\alpha_0\Delta T}\left(\pi_{410}\frac{\delta\rho_{410}}{\overline{\rho}_{410}} + \pi_{660}\frac{\delta\rho_{660}}{\overline{\rho}_{660}}\right)\right]\hat{g} + \nabla\cdot\underline{\tau},$$

$$\text{- } \textit{momentum equation} \qquad (15)$$

$$\overline{\rho}^{'}\frac{DT^{'}}{Dt} + Di\overline{\rho}^{'}T^{'}\omega = \nabla^2 T^{'} + \frac{Di}{Ra}\phi + \overline{\rho}^{'}H + Di^2\overline{T} - \frac{\overline{\rho}^{'}(T^{'}+\overline{T}+T_0)}{C_p}\left(\frac{DS_{L,410}}{Dt} + \frac{DS_{L,660}}{Dt}\right),$$

$$\text{- } \textit{energy equation} \qquad (16)$$

where T_0 is the surface temperature, *Ra* is the Rayleigh numbers defined as $\frac{\rho_0 g_0 \alpha_0 \Delta T d^3}{\eta_0\kappa_0}$. ω is the dimensionless velocity along the z-direction. ΔT is the temperature difference between the top and bottom; $\overline{T}_{bottom} + T_{potential} - T_0$. For the incompressible mantle, the dissipation number is 0 and the

governing equations are reduced to the Bousinessq Approximation (BA). The constants used for governing equations and reference state can be found in Table 1.

To solve the governing equations, we modified ConMan [*King et al.*, 1990], a finite element code based on 2-D Cartesian coordinate system for the ALA and BA experiments. The continuity and momentum equations are solved by using the penalty method [*Hughes*, 1987] and the energy equation is solved with the Streamline Upwind Petrov-Gelerkin [*Hughes and Brooks*, 1979] with a second-order predictor and corrector time-stepping scheme. The ALA implementation has been benchmarked against other mantle convection codes [*King et al.*, 2010].

4.2.2 Rheology

Deformation of lithosphere and mantle includes brittle, ductile and viscous behaviors [*Kohlstedt et al.*, 1995]. To consider the brittle-ductile behavior of lithosphere, we adopt the pseudoplastic yielding formulation described in Tackley [2000]. The lithospheric yielding strength is dominated by the smaller of the competing brittle and ductile strengths, described as,

$$\sigma_{yielding} = \min\left[z'\sigma_{brittle}, \sigma_{ductile}\right], \qquad \text{- yielding strength (17)}$$

where $\sigma_{brittle}$ and $\sigma_{ductile}$ correspond to brittle and ductile strength, respectively. The brittle strength is a function of the dimensionless depth, z', which is 0 at the top and 1 at the bottom. Although the brittle and ductile strengths are poorly constrained, we use constant brittle and ductile strengths of 10 and 0.5 GPa, respectively, consistent values used in previous dynamic subduction studies [*Tackley*, 2000; *Billen and Hirth*, 2007].

Below the brittle regime, the viscous mantle deformation is calculated by using an Arrhenius-type law controlled by temperature and pressure. Laboratory experiments [*Karato and Wu*, 1993; *Hirth and Kohlstedt*, 2003] show that the deformation of the upper mantle can be approximated by diffusion and dislocation creep; however, diffusion creep is thought to be the dominant deformation mechanism in the lower mantle. Thus, following previous work [*Billen and Hirth*, 2007; *Kneller et al.*, 2007; *Lee and King*,

2009] we formulate a composite viscosity of diffusion and dislocation creep for the upper mantle and diffusion creep for the lower mantle. The composite viscosity for the upper mantle is expressed as;

$$\eta_{comp} = \left(\frac{1}{\eta_{dif}} + \frac{1}{\eta_{dis}} \right)^{-1} \quad \text{- composite viscosity (18)}$$

where the diffusion and dislocation creep are described below;

$$\eta_{dif} = A_{dif}^{-1} d_g^{\ m} \exp\left[\frac{E_{dif} + PV_{dif}}{RT} \right] \quad \text{- diffusion creep (19)}$$

$$\eta_{dis} = A_{dis}^{\frac{-1}{n}} \exp\left[\frac{E_{dis} + PV_{dis}}{nRT} \right] \dot{\varepsilon}_s^{\frac{1-n}{n}} \quad \text{- dislocation creep (20)}$$

where A is the prefactor, E is the activation energy, V is the activation volume, d is the grain size, n is the stress exponent, m is the grain size exponent, R is the gas constant and $\dot{\varepsilon}$ is the second invariant of strain rate.

The pressure is calculated by using the linear summation of the reference states and density increases due to phase transitions. The temperature is calculated by summing the temperature perturbation, adiabatic temperature distribution and surface temperature (Figure 1b). However, the difference in the reference states for the ALA and BA formulations result in a large difference in the calculated viscosity. To facilitate the comparison between the ALA and BA formulations, we use the reference states ($\overline{P}$ and $\overline{T}$) from the ALA calculations for the viscosity calculations of the BA formulation. Finally, the effective viscosity of the lithosphere and mantle is defined below;

$$\eta_{eff} = \min\left[\eta(P, T, \dot{\varepsilon}), \frac{\sigma_{yielding}}{2\dot{\varepsilon}} \right] \quad \text{- effective viscosity (21)}$$

There are noticeable differences in the rheological parameters between the laboratory measurements and estimations from observations. For example, the brittle strength measured in the laboratory is much stronger than the strength estimated from geophysical observations [e.g., *Williams et al.*, 2004; *Carpenter et al.*, 2009]. Also, direct laboratory measurement of mantle viscosity are limited to

the upper mantle and more studies are required to evaluate the effect of water and volatiles on the mantle viscosity [*Karato*, 2010]. There is evidence showing that the upper mantle viscosity, especially, asthenosphere under the oceanic lithosphere is much weaker than the estimates based on laboratory measurements and glacial isostatic adjustment [*Ranalli*, 2001; *Hirth and Kohlstedt*, 2003]. Thus, we use a modified lithosphere and mantle rheology that is consistent with geophysical observations rather than laboratory measurements for deeper mantle [e.g, *King and Masters*, 1992; *King*, 1995]. The parameters used for the rheology and viscosity structure are described in Table 2 and Figure 1, respectively.

Previous studies have shown that the effective slab viscosity may be only 2-3 order larger than the mean upper mantle viscosity [*Zhong and Davies*, 1999; *Wu et al.*, 2008], in contrast to the very large viscosity (> ~10^{26} Pa.s) calculated from laboratory based rheology equations. However, recent numerical experiment studies show that a low CMB viscosity (~10^{20} Pa.s) reduces the geoid above the subduction zones significantly, which reconciles geoid calculations with observations and allows very stiff slabs [*Tosi et al.*, 2009] . The phase transition from perovskite to post-perovskite and partial melting may reduce the viscosity around the CMB [*Lay et al.*, 2004; *Ito and Toriumi*, 2007]. Thus, we use a viscosity reduction factor to reduce the CMB viscosity to ~10^{20} Pa.s between 2690 and 2890 km with a 100 km thick overlying linear viscosity transition zone.

4.2.3 Model setup

We formulate our numerical experiments using a domain of 2890 by 11560 km (1 by 4) consisting of 164 by 578 four-node quadrilateral elements. Because the phase transitions occur through thin phase loops (5 km), we uses rectangular elements spanning a width-height range of 20 by 5 km from 380 to 440 km and from the 620 to 690 km. Otherwise, 20 by 20 km elements are used throughout the remainder of the domain. The plate boundary (thrust) between the left-side oceanic and right-side continental lithosphere is defined at the center of the top of the domain (5780 km). Diverse implementations for the thrust zone have been used in previous studies [e.g., *Zhong and Gurnis*, 1995;

Chen and King, 1998; *Billen and Hirth*, 2007] and we implement a diagonal weak zone (27 degree) consisting of 16 elements with a constant viscosity of 10^{20} Pa.s (Figure 2).

The surface and bottom temperatures are constant (Table 1) with no heat flux boundaries along the side-walls. The surface of the overriding continental lithosphere is fixed (no-slip) to avoid symmetric subduction of the oceanic and continental lithosphere due to slab suction and viscous coupling between the subducting slab and overriding lithosphere [e.g., *Chen and King*, 1998; *Conrad et al.*, 2004; *Cízková et al.*, 2007; *Behounková and Cízková*, 2008]. The bottom and side-walls are free-slip boundaries along x and z directions, respectively. The oceanic plate is kinematically subducted along the weak zone with a convergence rate of 5 cm/a for 4 Myr in order to develop a slab with sufficient negative buoyancy to subduct under its own buoyancy. After that, the oceanic plate is released to subduct dynamically.

For the initial temperatures for the lithosphere and mantle, we use the half-space cooling model with a mantle potential temperature of 1673 K [*Stein and Stein*, 1992]. The net mantle adiabatic temperature profile is added to temperatures calculated from the half-space cooling model. For the continental lithosphere, we use a uniform thickness of thermal boundary layer corresponding to a 120 Myr old lithosphere. For the oceanic lithosphere, we use the half-space cooling model assuming a spreading rate of 5 cm/a from the left top (mid-ocean ridge), which creates ~120 Myr old plate at the trench (5780 km).

4.3 Results

4.3.1 Effect of viscosity increases across the 660 km discontinuity on slab buckling

Because there are a large number of parameters that influence the dynamics of subduction and in order to avoid redundancy, the experiments described in this study use a maximum slab strength of 10^{24} Pa.s, brittle and ductile strengths of 10 and 0.5 GPa, no phase transitions, low viscosity CMB, reflecting side-wall boundary conditions and an incompressible mantle unless otherwise noted.

A viscosity increase across the 660 km discontinuity (upper and lower mantle boundary) has been proposed based on fitting the observed long-wavelength geoid, ranging from ~10 to 100-fold [e.g., *Hager*, 1984; *King and Masters*, 1992; *Čadek and Fleitout*, 1999; *Mitrovica and Forte*, 2004] and plays a crucial role in the slab deformation and the style of mantle convection (e.g., whole or layered mantle convection) [e.g., *Gurnis and Hager*, 1988; *King and Hager*, 1994; *Behounková and Cízková*, 2008]. Thus, as a first step, we evaluate the effect of a viscosity increase across the 660 km discontinuity by conducting a series of experiments where we vary the grain size for the lower mantle resulting in 4-, 16-, 32-, 48-, 64-, 80-, 96-, 112- and 128-fold viscosity increases (Figure 1a and Table 2). These experiments show that slab buckling requires a viscosity increase across the 660 km discontinuity. A 4-fold viscosity increase develops fast and continuous subduction with negligible lateral slab deformation (no slab buckling) in the lower mantle. Increasing viscosity across the 660 km discontinuity acts a barrier and slows down slab descending in the lower mantle; large lateral slab deformation (slab buckling) develops. With increasing viscosity across the 660 km discontinuity, lateral slab deformation develops and periodic slab buckling is obtained when the viscosity increase is larger than 48-fold. Figure 3 shows that snapshots of slab temperatures and trajectories corresponding to the experiments using 16- and 80-fold viscosity increases, the representatives of no slab buckling and slab buckling regimes, respectively. With increases in viscosity across the 660 km discontinuity, more cycles of periodic slab buckling develop.

The time-dependent evolution of subduction with increases in viscosity across the 660 km discontinuity can be quantitatively analyzed by evaluating convergence rate and thickness of the oceanic lithosphere, and time-evolving lateral amplitude of the slab at the 660 km discontinuity, depicted in Figure 4. The convergence rate is measured at the surface; 200 km from the trench. The depth corresponding to 1200 C° is used to measure the thickness of the oceanic lithosphere. Time-evolving lateral amplitude of the slab at the 660 km discontinuity is measured by tracking x-coordinates of the mid-surface of the subducting slab from the left-wall boundary when the slab crosses the 660 km discontinuity. Using the subduction history, the amplitude and period of slab buckling are quantitatively evaluated and will be used for the slab buckling analysis described later.

As seen in Figure 4a, the experiment using a 16-fold viscosity increase shows that the convergence rate sharply increases up to ~41 cm/a when the slab descends to the upper mantle, observed in previous studies [*Cízková et al.*, 2007; *Behounková and Cízková*, 2008]. The catastrophic fast subduction weakens after 7.4 Myr when the subducting slab reaches and descends to the lower mantle. After the initial phase, the convergence rate becomes relatively stable by when the slab detaches at 104 Myr, corresponding to stable subduction with small variations in the dip of the subducting slab with time (Figure 4a). The thickness of the converging lithosphere shows an abrupt decrease of slab thickness corresponding to the catastrophic fast subduction in the initial phase (Figure 4c). After the initial phase, the thickness of lithosphere gradually decreases with time by when the slab detaches though small variations continue due to the small-scale convection cells (dripping) developed beneath the lithosphere. The amplitude of the slab at the 660 km discontinuity shows small variations because of the stable dip of the subducting slab, resulting in little periodic slab buckling (Figure 4e). With the small-scale convection cells developing beneath the lithosphere, small-scale convection cells develop above the 660 km discontinuity (upwelling) during the entire experiment run (110 Myr). The ridge, initially located at the left-top corner, migrates toward the trench with time; however, ridge subduction does not occur because the slab detaches before the ridge reaches the trench; ridge subduction is never observed in any of the calculations in this study.

Compared with the experiment using a 16-fold viscosity increase, the experiment using an 80-fold viscosity increase develops slab buckling and shows a much different subduction history. The subduction history can be broken down into three phases; 1) initial unstable subduction, 2) steady-state slab buckling, and 3) de-buckling of the stacked slab and slab detachment correspond to the circled 1, 2 and 3, respectively (Figure 4b, 4d and 4f). In the initial unstable subduction phase continuing by 46 Myr, catastrophic fast subduction (~37 cm at 7.4 Myr) and following unstable early slab buckling develop, resulting in an abrupt decrease of the slab thickness (Figure 4b and 4d). In the steady-state slab buckling phase between 46 and 119 Myr, a stable periodic buckling mode develops; the buckled slab stacks in the shallow lower mantle and slowly descends to the deeper lower mantle (Figure 3b). The periodic slab

buckling and convergence rate result in near-constant slab thickness (Figure 4d). In the steady-state slab buckling phase, there is an excellent correlation between the periodic convergence rate and dip of the subducting slab (Figure 4a). The local peaks of the convergence rate correspond to the locally shallowest and steepest dip of the subducting slab at 300 km depth; shallowing and steepening dip correspond to the local troughs of the convergence rate. The dip of the subducting slab at 150 km depth shows offsets from the dip of the subducting slab at 300 km depth. As expected, there is a good correlation between the lateral amplitude of the slab at the 660 km discontinuity and the dip of the subducting slab at 300 km (Figure 4f). In the de-buckling of the stacked slab and slab detachment phase, the stacked slab descends to the deep lower mantle and enters the low viscosity CMB; the stacked slab in the shallow lower mantle is de-buckled. Due to the de-buckling of the stacked slab, the style of slab deformation changes from steady-state slab buckling to continuous fast subduction without significant slab buckling by when slab detaches (Figure 3b and 4b). The continuous fast subduction results in less periodic evolution of the dip of the subducting slab (Figure 4b and 4f). In this phase, the slab thickness decreases with time, similar to the experiments showing no slab buckling (Figure 4c). After the slab detaches, the oceanic plate continues migrating toward the trench at a very slow rate while the detached slab in the upper and lower mantle continues descending and laterally spreading above the CMB. The very slow migration of the remnant oceanic lithosphere toward the trench is a consequence of the viscous coupling between the plate and whole mantle scale return flow due to the slab suction by the subducting slab in the lower mantle [*Conrad and Lithgow-Bertelloni*, 2004].

4.3.1.1 Slab buckling analysis

Following the description in Ribe et al. (2007), the style of slab buckling can be divided into two end members; viscous and gravitational buckling modes. The style of slab buckling is determined by using the dimensionless parameter below;

$$\Pi = H_d \left(\frac{g\Delta\rho}{\overline{\eta} U_1 d_1^2}\right)^{1/4}, \qquad \text{- dimensionless parameter (18)}$$

where H_d is the effective fall height, g is the effective gravity, $\Delta\rho$ is the density contrast (density contrast between subducting slab and ambient upper mantle), $\overline{\eta}$ is the mean slab viscosity, U_1 is the velocity of slab where slab buckling occurs, and d_1 is the slab thickness where slab buckling occurs. If the parameter Π is smaller than a critical value of 3.9, the buckling mode falls into viscous buckling mode, the mode of slab buckling in the Earth. In the viscous buckling mode, the amplitude of the slab buckling can be calculated by using the simple equation below;

$\delta = 0.5H_d + d_1 = \delta_1 + d_1$, - amplitude of the slab buckling (19)

where δ_1 is the amplitude of the slab buckling measured along the mid-surface of the slab [*Ribe*, 2003]. To calculate the unknown values of U_1 and d_1, we use the law of conservation of mass;

$U_0 \times d_0 = U_1 \times d_1$, - conservation of mass (20)

where U_0 and d_0 are the velocity (convergence rate of the oceanic lithosphere) and thickness of fluid (oceanic lithosphere) at the slot (trench), respectively, which can be easily measured. However, it is difficult to calculate U_1 and d_1 of the deforming slab in the mantle therefore, the buoyancy number (B) is useful;

$$B = \frac{g\Delta\rho H_d^{\,2}}{\overline{\eta} U_0}.$$ - buoyancy number (21)

If the buoyancy number is small enough (< 1.0), the falling fluid (slab) experiences negligible extension/compression along the mid-surface of the falling fluid [*Ribe*, 2003]. Thus, the thickness and velocity of the slab are assumed constant throughout the upper mantle; U_0 and d_0 can be substituted for U_1 and d_1.

Figure 5 depicts the convergence rate and time-evolving amplitude of the slab in the steady-state slab buckling phase of the experiment using an 80-fold viscosity increase. Because the parameter is valid for the steady-state slab buckling, the steady-state slab buckling phase is chosen. In contrast to kinematically injected fluid (constant mass flux) used to develop the scaling laws [*Ribe*, 2003], the convergence rate in the subduction experiments periodically evolves with slab buckling; three cycles are

discerned by evaluating slab deformation consisting of steepening and shallowing stages (Figure 5c and 5d). Because the fluid is incompressible and no phase transitions are used in these experiments, the dynamic evolution of the convergence rate contrasting constant mass flux is the only deviation from the scaling laws. Here averaged convergence rate and slab thickness in the steady-state slab buckling phase are used for velocity (U_0) and thickness (d_0) of fluid, respectively (Figure 5a and 4d). To measure the amplitude of the slab buckling along the mid-surface (δ_1), the time-evolving amplitude of the slab is used (Figure 5b).

To calculate the dimensionless parameter, the density and viscosity of the subducting slab need to be evaluated. However, the density and viscosity of the subducting slab depend on slab temperatures and, the viscosity significantly varies from the slab core to surface. Therefore, the equations defined in Parmentier et al. [1976] are applied to calculate mean slab density and viscosity, described below;

$$\overline{\rho} = \frac{\int_V \Delta\rho dV}{\int_V dV}, \qquad \text{- mean slab density (22)}$$

$$\overline{\eta} = \frac{\int_V \eta \dot{\varepsilon} dV}{\int_V \dot{\varepsilon}\, dV}. \qquad \text{- mean slab viscosity (23)}$$

The mean slab density and viscosity evolves with time but, the variations are relatively small in the steady-state slab buckling phase. Therefore, we use the averaged mean slab density and viscosity for buckling analysis. Due to the angle of subduction, the effective fall height is the distance between the bottom of the oceanic lithosphere at the trench and the mean slab amplitude at the 660 km discontinuity which also varies with time. However, the variations are relatively small in the phase and the mean can be approximated by assuming that the averaged dip of subduction is 60 degree; the effective fall height is simply calculated below;

H_d = (660 km – d_0)/sin(60°). - effective fall height (24)

Table 3 shows the amplitudes of calculated and measured slab buckling by using the set of experiments described above. With increases in viscosity across the 660 km discontinuity, the steady-state slab buckling phase has more cycles and longer wavelength. Regardless of increases in viscosity, variations of mean slab buoyancy ($\Delta\rho g$) are insignificant. However, mean slab viscosity and mean convergence rate generally decreases with increases in viscosity across the 660 km discontinuity. Buoyancy numbers (> 1.0) corresponding to the experiments indicate slab extension/compression in the mantle but, the extension/compression (< 10%) is negligible. Generally, the measured buckling amplitude of the slab is consistent with the calculated buckling amplitude of the slab; the error is smaller than 15% despite the complexities of the dynamic subduction experiments. The last cycle usually has a smaller amplitude compared with the other cycles and, it is attributed to the de-buckling of the stacked slab due to the low viscosity CMB. The period of slab buckling also is close to the value for pure viscous buckling (~1.218), which indicates that the scaling laws are in good agreement with the slab buckling for a wide range of viscosity increases across the 660 km discontinuity (Table 3).

4.3.2 Slab buckling in kinematic and dynamic subduction experiments

The slab buckling analysis above shows that scaling laws developed by Ribe (2003) can be successfully applied to time-dependent subduction experiments even though the scaling laws were derived from kinematic model experiments using a constant mass flux. However, a question still remains; how large is the derivation from the scaling laws due to time-dependent dynamic subduction? To answer the question, a comparison between dynamic and kinematic subduction experiments is conducted to discern the influence of time-dependent dynamic subduction. Previous studies show that slab buckling occurs in dynamic as well as kinematic subduction experiments [*Christensen*, 1996; *Cízková et al.*, 2007; *Behounková and Cízková*, 2008]. However, a quantitative comparison between dynamic and kinematic subduction has not been conducted. Han and Gurnis [1999] show that the dynamic subduction experiment can be approximated by a kinematic subduction experiment when an appropriate convergence

rate is prescribed. Although their experiments show near steady-state subduction instead of periodic slab buckling, their work suggests that a similar style of slab buckling develops in the kinematic subduction experiments when the prescribed convergence rate is comparable with the mean convergence rate of the dynamic subduction experiments.

To evaluate the influence of time-dependent dynamic subduction, selected dynamic subduction experiments (16-, 48- and 80-fold viscosity increases) described above are repeated using kinematically prescribed convergence rate along the surface of the oceanic lithosphere. Because the scaling laws are valid for the steady-state slab buckling phase, the temperature and flow structures corresponding to 26.5, 39.7 and 39.7 Myr of the dynamic subduction experiments using 16-, 48- and 80-fold viscosity increases are used for the initial conditions of the kinematic subduction experiments. Instead of the time-dependent convergence rate in the dynamic subduction experiments, constant rates of 5.94, 3.80 and 3.38 cm/a are used for the kinematic subduction experiments using 16-, 48- and 80-fold viscosity increases.

Figure 6 shows the time-evolving amplitude of the slab at the 660 km discontinuity and slab thickness corresponding to the dynamic and kinematic subduction experiments using 16- and 80-fold viscosity increases. Generally, slab trajectory and thickness show fairly similar styles of slab evolution with time in both the kinematic and dynamic subduction experiments. The experiment using a 16-fold viscosity increase evolves differently after 90 Myr because the slab does not detach in the kinematic subduction experiment (Figure 6a and 6c). The experiment using an 80-fold viscosity increase shows a good correlation in amplitude and wavelength (period) of the slab buckling except for the cycle 3. The stacked slab in the kinematic subduction experiment is de-buckled due to the low viscosity CMB where subducted slab enters earlier than the dynamic subduction experiment. Table 4 shows relevant slab buckling analysis corresponding to the dynamic and kinematic subduction experiments. As expected, the amplitude and wavelength of slab buckling agree within 20 % for the scaling laws in both the dynamic and kinematic subduction experiments. These experiments show that the deviations from the scaling laws in the dynamic subduction experiments are not the consequence of the time-dependent convergence rate; the scaling laws predict slab buckling in the dynamic subduction experiments.

4.3.3 Effect of larger slab strength on slab buckling

We evaluate the slab buckling by using a maximum slab viscosity of 10^{24} Pa.s which creates an effective slab viscosity of ~10^{22} Pa.s; 2-3 order higher than the upper mantle viscosity. As described above, the low viscosity CMB allows reasonable geoid observed over the subduction zones with stronger slab calculations [*Tosi et al.*, 2009]. Therefore, it is worth evaluating whether the scaling laws can be applicable to the experiments with increasing slab strength.

We repeat the same subduction parameters and rheologies except for using a maximum slab viscosity of 10^{26} Pa.s. Table 5 shows relevant parameters and calculations for slab buckling analysis. Similar to the experiments using a maximum slab viscosity of 10^{24} Pa.s, all the experiments begin with exceptionally high convergence rates (~ 40 cm/a) until the subducting slab reaches the 660 km discontinuity (Figure 7a). The minimum viscosity increase across the 660 km discontinuity required for periodic slab buckling is 64-fold, larger than the 48-fold viscosity increase needed to develop slab buckling in the experiments using a maximum slab viscosity of 10^{24} Pa.s. The three phases of the subduction (initial unstable subduction, steady-state slab buckling, and de-buckling of the stacked slab and slab detachment) are apparent (Figure 7), as observed in the experiments using a maximum viscosity of 10^{24} Pa.s. The experiments using larger slab viscosities allow for a longer lifespan of subduction and the steady-state slab buckling phase, slightly slower mean convergence rate, and longer period (wavelength) of slab buckling compared with the experiments using smaller slab viscosities (Table 5 and Figure 7). Due to the larger effective slab viscosity (~10^{24} vs. ~10^{22} Pa.s), the buoyancy numbers are much smaller than those from the experiments using a maximum slab viscosity of 10^{24} Pa.s, which indicates the stiffer slabs undergoing negligible slab compression/extension. Compared with the previous experiments using a smaller effective slab viscosity, larger deviations from the scaling laws occur in the last cycle; the last buckling cycle is more strongly affected by the low viscosity CMB more than in the experiments using a smaller slab viscosity (Figure 7a and 7c). Despite the measurable differences, the

scaling laws still predict the slab buckling for the experiments using a maximum slab viscosity of 10^{26} Pa.s; the scaling laws are valid for a wide range of the slab viscosity.

4.3.4 Effect of phase transitions on slab buckling

Numerous studies evaluated the effect of phase transitions on the vigor of penetration of the subducting slab in the lower mantle [e.g., *Christensen and Yuen*, 1985; *Christensen*, 1995; *King and Ita*, 1995; *Tackley*, 1995; *Cserepes et al.*, 2000; *King*, 2002]. In particular, it is well known that as a result of the endothermic phase transition from ringwoodite to perovskite plus magnesiowüstite the phase boundary in the subducting slab occurs at a deeper depth than the surrounding mantle; high density slab can be significantly retarded or even stop at ~660 km depth [*Christensen and Yuen*, 1984]. However, there is a consensus that even with phase transitions, slabs penetrate into the lower mantle, consistent with the existence of slab buckling in the shallow lower mantle as inferred from seismic tomography.

The effect of phase transitions on the style of slab buckling has been rarely studied [*Behounková and Cízková*, 2008]. Běhounková and Čížková [2008] evaluate the effect of phase transitions on the style of slab buckling by switching on and off individual phase transitions from olivine to wadsleyite and/or from ringwoodite to perovskite plus magnesiowüstite. They found that the phase transition from olivine to wadsleyite develops significant slab buckling. However, the phase transition from ringwoodite to perovskite plus magnesiowüstite itself plays only a minor role in the development of slab buckling. Although they show that the contribution of individual phase transitions on the style of slab buckling, they do not evaluate whether the slab buckling is consistent with the scaling laws derived by Ribe [2003]. Thus, we evaluate the validity of the scaling laws by including both phase transitions from olivine to wadsleyite and from ringwoodite to perovskite plus magnesiowüstite.

Laboratory and theoretical studies show large uncertainties of the Clapeyron slopes of the phase transitions from olivine to wadsleyite and from ringwoodite to perovskite plus magnesiowüstite [*Duffy*, 2005; *Frost*, 2008 and references therein]. Here, we use median values of the Clapeyron slopes of 2 and -2 MPa/K for the phase transitions from olivine to wadsleyite and from ringwoodite to perovskite plus

magnesiowüstite. The density increases across the phase transitions are assumed constant; 5 % and 9 % for the phase transitions from olivine to wadsleyite and from ringwoodite to perovskite plus magnesiowüstite, respectively, constrained by laboratory and seismological observations [*Dziewonski and Anderson*, 1981; *Bina and Wood*, 1987]. Including the phase transitions, we perform a series of experiments with 4-, 16-, 32-, 48- and 64-fold viscosity increases.

Figure 8 shows selected snapshots of the slab temperatures and trajectories corresponding to the experiments using 16- and 64-fold viscosity increases as representative examples. Compared with the experiments without phase transitions, all the experiments except for the experiment using a 4-fold viscosity increase develop significant slab buckling, indicating that the phase transitions reduce the minimum viscosity increase across the 660 km discontinuity. In addition, an additional slab pull due to phase transitions from olivine to wadsleyite increases convergence rate of the oceanic lithosphere; very high convergence rates of ~65 cm/a are observed in the initial unstable slab buckling phase (Figure 9a and 9b). Similar to the experiments developing periodic slab buckling described in sections 3.1, 3.2 and 3.3, subduction consists of three phases; initial unstable subduction, steady-state slab buckling, and de-buckling of the stacked slab and slab detachment. However, thickness of the oceanic lithosphere gradually decreases with time in all the experiments, especially in the experiments using a smaller viscosity increase (Figure 9c vs. 9d). The lifespan of the subduction and wavelength of the slab buckling are reduced compared with the experiments without phase transitions.

Table 6 shows relevant parameters and calculations for the slab buckling analysis. The steady-state slab buckling phase occurs much earlier and shorter than the experiments without phase transitions. The effective slab buoyancy and viscosity do not significant vary with time. The mean convergence rates in the steady-state slab buckling phase are much higher than the experiments without phase transitions and tend to increase with subsequent cycles, especially, in the experiments using larger viscosity increases across the 660 km discontinuity. Thus, we calculate the buoyancy numbers and dimensionless parameters by separately analyzing each cycle of slab buckling, although this assumes each cycle is under the steady-state. Because the buoyancy numbers are smaller than 1.0, no extension of the subducting slab is

assumed. The buckling analysis shows that all the experiments tend to decrease the amplitude of the slab buckling with subsequent cycles caused by de-buckling of the stacked slab. As observed in the experiments above, period (wavelength) of the slab buckling increases with increases in viscosity across the 660 km discontinuity. Despite the heterogeneous composition of slab due to the presence of the phase transitions, the scaling laws generally predict the period (wavelength) and amplitude of the slab buckling; deviations from the scaling laws due to the phase transitions are not significant.

4.3.5 Effect of the flow-through boundary conditions on slab buckling

3-D subduction experiments are still very expensive and there are significant challenges in creating 3-D plate-like subduction; thus, 2-D Cartesian models remain important tools in subduction modeling. However, the 2-D Cartesian models require an examination of the side-wall boundary conditions. Flow-through boundary conditions allow lateral flow of the mantle (trench migration if the mantle is the reference frame) whereas the reflecting boundary conditions confine the return flow of the mantle. The experiments using flow-through boundary conditions reduce slab buckling [*Enns et al.*, 2005; *Billen*, 2008]. Here, we evaluate the effect of the flow-through boundary conditions on the slab buckling by including the phase transitions which develop more cycles of periodic slab buckling, shown above. To avoid numerical instabilities, we use the thermal and flow structures at 12 Myr from the dynamic subduction experiments using the reflecting boundary conditions.

Figure 10 shows that the convergence rate with time and selected snapshots of the slab trajectories in the mantle corresponding to the experiments using the flow-through boundary conditions. In the experiment using a 16-fold viscosity increase, slab buckling develops when the slab passes the phase transition zone from olivine to wadsleyite at ~410 km depth; periodic convergence rate indicates slab buckling (Figure 10a). However, the mean mantle flows to the right, relative to the trench, keeping the buckled slab from being stacked on the top of itself in the shallow lower mantle. Therefore, the apparent slab morphology in the shallow lower mantle does not show the extensive slab buckling, as seen in the previous experiments. At ~27 Myr, the mantle flows to the left direction (trench advance if the

mantle is assumed as the reference frame) by the slab detachment at 41 Myr with negligible slab buckling. In the experiments using larger viscosity increases across the 660 km discontinuity, less slab buckling develops when the slab passes the phase transition zone from olivine to wadsleyite compared with the experiment using a smaller viscosity increase across the 660 km discontinuity; the amplitude of the convergence rate becomes smaller. In addition, larger viscosity increases across the 660 km discontinuity keep the subducting slab from descending into the lower mantle and stacked slab is not observed. As a result, the scaling laws are not relevant to the experiments using the flow-through boundary conditions.

Because the mantle flows in the experiments using the flow-through boundary conditions are dynamically controlled, it is difficult to quantitatively evaluate the effect of the lateral mantle flows on slab buckling; these experiments would be the end-member experiments (fast mantle flows) significantly reducing slab buckling. However, our findings show that the development of slab buckling is sensitive to the influence of ambient mantle flows (trench migration); mantle flows suppress slab buckling in the mantle.

4.3.6 Effect of mantle compressibility on slab buckling

Previous studies have shown that the effect of compressibility on the mantle convection is relatively minor [*Jarvis and McKenzie*, 1980; *Lee and King*, 2009; *King et al.*, 2010]. However, the effects of compressibility in previous studies were evaluated by using one or more of the simple environments including: constant or temperature dependent mantle viscosity, homogeneous mantle (no phase transitions) and shallower upper mantle (small Rayleigh number). Because the mantle adiabat and density increases due to the adiabatic mantle compression are significant (Figure 1), the effect of the mantle compressibility on the slab evolution could be more considerable than that in previous studies. Thus, we evaluate the validity of the scaling laws by analyzing the slab buckling of the heterogeneous subducting slab caused by compressibility. For simplicity, the same parameters and rheologies for the experiment using a maximum slab viscosity of 10^{24} Pa.s are repeated by including the Anelastic liquid approximation (equations 14, 15 and 16).

Similar to the experiments using the incompressible fluid approximation in sections 3.1, 3.2, 3.3 and 3.4, all the experiments show pulses of convergence rates (~40 cm) in the initial phase. Increases in viscosity across the 660 km discontinuity develop more cycles of slab buckling. An 80-fold viscosity increase is required for periodic slab buckling, larger than a 64-fold viscosity increase in the incompressible subduction experiments. Because the experiments using 48- and 64-fold viscosity increases show irregular period and amplitude of buckling, slab buckling analysis is not applied. Due to the adiabatic mantle compression, the subducting slab has higher density (~10%) than the incompressible subducting slab (Table 7). However, the mean slab viscosity is a little smaller than the incompressible slab viscosity due to higher slab temperatures, which offset the density increases. The thickness of the converging oceanic lithosphere is a little thinner than in the incompressible subduction experiments. The thinner lithosphere is attributed to the heat generated by viscous dissipation [*Lee and King*, 2009]; high shear strain rate beneath the oceanic lithosphere contributes to a large heat source in the upper mantle and temperatures below the oceanic lithosphere (120 km depth) are ~1370 C°, ~50 C° higher than the incompressible subduction experiments (equation 5 and 16).

Compared with the incompressible subduction experiments, slab buckling shows irregular and asymmetric amplitude and wavelength (period) (Figure 7c vs. 11a). The wavelength of the slab buckling for the later cycle significantly decreases but, the amplitude of the slab buckling does not decrease even though the slab enters the low viscosity CMB (Figure 11a and 11b). The different style of subduction history is attributed to weak slab pull in the low viscosity CMB; the return flow of the mantle along the CMB contributes to significant heat generated by viscous dissipation, which thermally dissipates the subducted slab in the low viscosity CMB. Therefore, the subducting slab in the mantle is not significantly affected by the mantle flow in the low viscosity CMB. Table 7 shows that the convergence rate increases with time whereas the thickness of the oceanic lithosphere is relatively constant regardless of the increasing convergence rates. Due to the relatively small mean slab viscosity, the buoyancy number is larger than 1.0 but, the slab extension is neglected in the slab buckling analysis. The measured buckling amplitudes show larger irregularities compared with the incompressible subduction experiments. As

shown above, all the experiments show decreasing dimensionless periods for the later cycle of the slab buckling, due to shorter wavelength of the slab buckling. Except for the later cycle, however, the scaling laws are generally valid (error < 20%) in the compressible subduction experiments.

4.4 Discussion

4.4.1 Geological implications of periodic convergence rate and slab buckling

The periodic convergence rate and slab buckling observed in our calculations (e.g., Figure 4) have interesting implications for geology. Seismic tomography images show that a dip of the subducting slab in the shallow depth (~100 km depth) depends on an age of the subducting slab; older slab tends to have steeper dip [*Jarrard*, 1986; *King*, 2001; *Sdrolias and Müller*, 2006]. However, there is a poor correlation between the age and dip of the subducting slab in the deeper upper mantle (from ~150 to 400 km depth); the dips are scattered regardless of the slab ages [*Jarrard*, 1986; *King*, 2001; *Cruciani et al.*, 2005; *Sdrolias and Müller*, 2006]. As described above, our results show time-dependent variations of the dip of the subducting slab in the mid-upper mantle due to slab buckling; the dip of the slab varies from ~45° to even larger than 90° (Figure 4 and 5). Because seismic tomography only provides present-day snapshots of the subducting slab, we only see an instant within the time-dependent evolution of the dip of the subducting slab, consistent with the observed poor correlation between the slab age and dip [*King*, 2001].

Plate reconstruction models of Sdrolias and Müller [2006] show that the convergence rate of the oceanic lithosphere toward the trench has been changed in a time-dependent manner. Our calculations show that a sudden increase and following decrease of the convergence rate occur when the slab passes the upper mantle and reaches the bottom of the upper mantle. For example, the Izu-Bonin-Mariana subduction zone shows a sudden increase and decrease of the convergence rate since the initiation of subduction at ~50 Ma, and following sinusoidal-like evolution of the convergence rate (Figure 12a). Slab

buckling is observed in the Mariana arc and not in the Izu-Bonin, which is thought to be attributed to the asymmetric roll-back along the Izu-Bonin-Mariana where Mariana is the hinge point of the asymmetric roll-back [*Sdrolias and Müller*, 2006]. Our results show that periodic convergence rate is expected in subduction zones even though trench roll-back occurs; trench roll-back prevents slab stacking on the top of itself in the shallow lower mantle, observed in our calculations (Figure 10). The convergence rate in the Java and Middle America subduction zones where slab buckling is observed also shows sinusoidal-like convergence rate with time (Figure 12). Therefore, the time-dependent convergence rate is an important supporting evidence for slab buckling in the mantle.

Along with the time-dependent convergence rate at the trench, the time-dependent spreading rate at the mid-ocean ridges since 180 Ma [*Cogné and Humler*, 2004; *Conrad and Lithgow-Bertelloni*, 2007; *Stepashko*, 2008] is also consistent with the time-dependent evolution of the convergence rate and slab buckling in our calculations. These studies show that the spreading rate of the oceanic lithosphere bounded by subduction zones evolves in a time-dependent manner compared with the spreading rate at the mid-ocean ridges bounded by passive margins (e.g., west Pacific vs. north Atlantic plates). Because most of the driving force (~90%) of the subduction is attributed to the slab [*Forsyth and Uyeda*, 1975; *Lithgow-Bertelloni and Richards*, 1998; *Conrad and Lithgow-Bertelloni*, 2002], the generation of the oceanic lithosphere at the ridge is a passive phenomenon. Therefore, it can be hypothesized that the generation of the oceanic lithosphere at the mid-ocean ridge is controlled by the termination of the oceanic lithosphere at the trench; the generation and termination rates of the oceanic lithosphere balance each other. For example, there is a good positive correlation between the half-spreading rate of the Nazca plate and the convergence rate along the Andes arc (Figure 12b). However, ridge migration/jump, trench migration (roll-back/advance) and asymmetric spreading rate at the mid-ocean ridge may results in a large over/underestimation of the spreading rate, which causes difficulties in quantitative comparisons between spreading and convergence rates [*Cogné and Humler*, 2004; *Sdrolias and Müller*, 2006]. In addition, the underlying plumes and/or hotter mantle under the mid-ocean ridge causing rapid ocean spreading at the mid-ocean ridge result in an imbalance between spreading and convergence rates [*Larson*, 1991; *Cogné*

and Humler, 2004]. Despite the difficulties, the simple balance as a first-order approximation indicates that the time-dependent spreading rate at the mid-ocean ridge is a natural expression of the time-dependent convergence rate caused by slab buckling.

In addition to the geophysical studies described above, geochemical and petrological evidence also indicates significant time-dependence in subduction zones. For instance, the temporal and spatial arc magmatism in the south-central Andes has been related to the time-dependent dip of the subducting slab [e.g., *Jordan et al.*, 2001; *Kay et al.*, 2005; *Kay et al.*, 2006]. Although the detailed mechanism is likely to be complicated by trench migration and subduction erosion, the alternating eastward and westward migrations of the arc volcanoes is thought to be related to the alternating shallowing and steepening dip of the subducting slab, respectively [*Kay*, 2002; *Folguera et al.*, 2006; *Kay et al.*, 2006]. Plate reconstruction models show that the convergence rate in the south-central Andes was increasing from early Oligocene to mid-Miocene and decreasing since mid-Miocene [*Sdrolias and Müller*, 2006] (Figure 13a). Because arc volcanoes are found from ~100 to 150 km above the subducting slab regardless of slab dip [*Syracuse and Abers*, 2006], the shallowing slab corresponding to the increasing convergence rate from early Oligocene to mid-Miocene relocates the arc volcanoes to the eastward. Since mid-Miocene, the steepening slab corresponding to the decreasing convergence rate migrates the arc volcanoes to the westward. Our calculations of slab buckling are well correlated with the periodic convergence rate and dip of the subducting slab (Figure 13b), which is supported by the seismic tomography images showing apparent slab thickening in the lower mantle [*Grand*, 1994; *Fukao et al.*, 2001; *Ren et al.*, 2007; *Li et al.*, 2008]. Although this is a first-order approximation due to paucity of other subduction conditions such as trench migration, our calculations indicate that the slab buckling contributes to the alternating migration of arc volcanoes in the Andes.

4.4.2 Caveats and limitations

As described above, periodic convergence rate is a consequence of periodic slab buckling in the mantle. In addition, we show that varying dip of the subducting slab is a common process of time-

dependent nature of Earth's evolution. However, it is worth noting some caveats and limitations of this study.

First, the influence of the initial temperature and viscosity structure is needed to be evaluated. For the initial temperature and viscosity structure, a 1-D (depth-dependent) temperature and density profiles calculated from the half-space cooling model and the Adams-Williamson equation with phase transitions are used; absolutely a priori condition but broadly used in previous studies [e.g., *Han and Gurnis*, 1999; *Conrad and Hager*, 2001; *Billen and Hirth*, 2007; *Lee and King*, 2010]. The initial temperature and viscosity structures evolve through secular cooling, radiogenic heat production and mantle convection including plume and subduction; transient 2-D structures establish. Because Earth's heat budget has been evolved for ~ 4.6 billion year, the initial temperature and viscosity structures at the subduction initiation are transient 2-D structures. In the analog or numerical experiments using 1-D temperature and viscosity structures (e.g., radial viscosity structure), the influence of the transient 2-D temperature and viscosity structures is not an issue [e.g., *Funiciello et al.*, 2003; *Enns et al.*, 2005]. However, the mantle and slab viscosities as well as the depth of the phase transitions considered in this study are sensitive to temperature and pressure; the transient 2-D temperature and viscosity structures could influence the slab evolution in the initial phase. For example, the initial temperature profile of the oceanic lithosphere defined by the half-space cooling model rapidly evolves to a different temperature profile which reflects the influence of shearing and small-scale convection cells beneath the oceanic lithosphere; the deviation from the initial conditions becomes larger in the experiments including compressibility. Therefore, cares should be taken into account in the numerical and analog experiments to avoid significant deviations from the 1-D a priori temperature and viscosity profiles.

Second, most of the experiments here do not consider the effect of trench migration on the slab evolution; the trench expressed as a weak zone is fixed at the middle of the domain (Figure 2). The effect of trench migration (advance or roll-back) has been studied for decades through numerical and analog experiments [*Zhong and Gurnis*, 1995; *Christensen*, 1996; *Funiciello et al.*, 2003; *Enns et al.*, 2005; *Schellart*, 2005]. Because of difficulties in treatment of the thrust zone between the subducting slab and

overriding plate, diverse alternatives are used to model trench migration; 1) kinematically migrated trench [e.g., *Christensen*, 1996; *Olbertz et al.*, 1997], 2) free subducting plate without an overriding plate [e.g., *Funiciello et al.*, 2003; *Enns et al.*, 2005] and 3) flow-through boundary conditions with a fixed trench [e.g., *Gurnis and Hager*, 1988; *Chen and King*, 1998]. Despite the limitation of the methods, the experiments show that trench migration (advance or roll-back) creates a stagnant slab above the 660 km discontinuity and the penetration of the subducting slab in the lower mantle is suppressed; we observe similar results in our calculations. However, we only evaluate two end-members; no trench migration (reflecting boundary conditions) or very fast trench migration (flow-through boundary conditions). The influence of the intermediate rate of trench migration on the subduction zones, consistent with the plate reconstruction models, remains for a future study.

In this study, with the exception of shallower depth, viscosity of the subducting slab is controlled by temperature, density and strain rate (upper mantle only) in the Arrhenius type viscosity equation. However, water, pre-developed faults/cracks and grain size reduction in the subduction slab may reduce the effective slab strength significantly [*Ranalli*, 1991; *Riedel and Karato*, 1997; *Hirth and Kohlstedt*, 2003]. For example, if the grain size of the subducting slab is reduced through the phase transition from olivine to spinel in the upper mantle [*Riedel and Karato*, 1997], the slab strength entering the lower mantle will be weaker than our calculations, leading to even shorter wavelength (period) slab buckling in the lower mantle. In addition, laboratory measurements show that thermal expansivity and conductivity of the mantle are pressure and temperature dependent [*Hofmeister*, 1999; *Liu and Li*, 2006]. If the thermal expansivity (conductivity) of the subducting slab decreases (increases) with depth, the reduced negative slab buoyancy retards its descending to the lower mantle [*Ita and King*, 1998]; slab buckling should be more prevalent than our results.

4.5 Summary and Conclusion

Recent seismic tomography images show that apparent slab thickening in the shallow lower mantle is not an artifact but a real slab structure, which is consistent with slab buckling. Our calculations demonstrate that periodic slab buckling is a common process expected in subduction systems and results in periodic convergence rate of oceanic lithosphere. In our calculations, we examine the effect of the following factors on periodic slab buckling by using 2-D dynamic subduction experiments and the findings are summarized below.

1. A viscosity increase across the 660 km discontinuity (upper-lower mantle boundary) is required to develop periodic slab buckling in shallow lower mantle. Larger mean slab viscosities require larger viscosity increases across the 660 km discontinuity; a 48-fold viscosity increase for the mean slab viscosity of ~10^{22} Pa.s whereas a 64-fold viscosity increase for the mean slab viscosity of ~10^{24} Pa.s is required for periodic slab buckling.

2. The subduction history developing periodic slab buckling consists of three phases; 1) initial unstable subduction, 2) steady-state slab buckling, and 3) de-buckling of the stacked slab and slab detachment. In the phase 1, catastrophic fast subduction and a sudden reduction of slab thickness occur. In the phase 2, stable slab buckling is developed by stacking on itself in the shallow lower mantle and results in periodic convergence rate. In the phase 3, the stacked slab is de-buckled due to the descending slab in the low viscosity CMB, which results in continuous slab descending with little slab buckling.

3. Phase transitions from olivine to wadsleyite (~410 km depth) and/or from ringwoodite to perovskite plus magnesiowüstite (~660 km depth) develop significant slab buckling compared with the experiments without phase transitions; shorter wavelength (period), larger amplitude and faster convergence rate occur. Phase transitions reduce the viscosity increase required for the onset of periodic slab buckling.

4. Flow-through boundary conditions allowing lateral mantle flow develop less slab buckling. Lateral mantle flow (trench migration if the mantle is the reference frame) keeps the subducting slab from stacking on itself in the shallow lower mantle; the stagnant slab on the bottom of the upper mantle does not develop apparent slab thickening (buckling).

5. The dynamic subduction experiments including compressibility develop periodic slab buckling, similar to the incompressible dynamic subduction experiments. However, the heat generated by viscous dissipation along the low viscosity CMB thermally dissipates the subducted slab and weakens the return flow of the mantle in the CMB. Thus, de-buckling of the stacked slab in the lower mantle does not occur; the amplitude of the slab buckling does not significantly decrease.

With our calculations, we examine whether the scaling laws for buckling behavior of descending fluid are valid for the slab buckling in our calculations. Despite the complexities of dynamic subduction experiments, the scaling laws derived by Ribe [2003] generally predict (error < 20%) the slab buckling. However, the scaling laws are not valid for the experiments using the flow-through boundary conditions; stationary subduction without significant trench migration and lateral mantle flow is required for periodic slab buckling.

Periodic slab buckling and convergence rate of the oceanic lithosphere have meaningful geological implications. First, the periodic shallowing and steepening subducting slab in depth from ~150 to 400 km is consistent with the poor correlation between slab age and dip; the seismic tomography images only show present-day snapshots of either shallowing or steepening slab. Second, the sinusoidal-like style of the convergence rate evaluated from the plate reconstruction models is apparently similar to the periodic convergence rate observed in our calculations. Third, the oceanic plates of which margins are bounded by subduction zones (e.g., Pacific plate) show large amplitude of seafloor spreading rate; the time-dependent convergence rate of the oceanic lithosphere due to the slab buckling derives the time-dependent seafloor spreading rate. Last, the alternating eastward and westward migration of the arc volcanoes in the Andes is thought to be related to the alternating shallowing and steepening subducting slab; the style of the slab buckling and convergence rate is well consistent with the alternating migration of the arc volcanoes in the Andes. In summary, the geological evidence strongly suggests that the periodic slab buckling is a natural expression of Earth's subduction.

References

Akaogi, M., E. Ito, and A. Navrotsky (1989), Olivine-modified spinel-spinel transitions in the system Mg_2SiO_4-Fe_2SiO_4: Calorimetric measurements, thermochemical calculation, and geophysical application, *Journal of Geophysical Research*, *94*, 15,671-615,685.

Akaogi, M., H. Takayama, H. Kojitani, H. Kawaji, and T. Atake (2007), Low-temperature heat capacities, entropies and enthalpies of Mg_2SiO_4 ploymorphs, and a-b-g and post-spinel phase relations at high pressure, *Physics and Chemistry of Minerals*, *34*, 169-183.

Behounková, M., and H. Cízková (2008), Long-wavelength character of subducted slabs in the lower mantle, *Earth and Planetary Science Letters*, *275*(1-2), 43-53.

Billen, M. I. (2008), Modeling the dynamics of subducting slabs, *Annual Review of Earth and Planetary Sciences*, *36*(1), 325-356.

Billen, M. I., and G. Hirth (2007), Rheologic controls on slab dynamics, *Geochemistry Geophysics Geosystems*, *8*(8), Q08012, doi: 10.1029/2007gc001597.

Bina, C., and B. Wood (1987), Olivine-spinel transitions: Experimental and thermodynamic constraints and implications for the nature of the 400-km seismic discontinuity, *Journal of Geophysical Research*, *92*, 4,853-854,866.

Birch, F. (1952), Elasticity and constitution of the Earth's interior, *Journal of Geophysical Research*, *57*, 227-286.

Čadek, O., and L. Fleitout (1999), A global geoid model with imposed plate velocities and partial layering, *Journal of Geophysical Research*, *104*(B12), 29055-29075.

Carpenter, B. M., C. Marone, and D. M. Saffer (2009), Frictional behavior of materials in the 3D SAFOD volume, *Geophysical Research Letter*, *36*(5), L05302.

Chen, J. N., and S. D. King (1998), The influence of temperature and depth dependent viscosity on geoid and topography profiles from models of mantle convection, *Physics of the Earth and Planetary Interiors*, *106*(1-2), 75-92.

Christensen, U. (1995), Effectts of phase-transitions on mantle convection, *Annual Review of Earth and Planetary Sciences*, *23*, 65-87.

Christensen, U. R. (1996), The influence of trench migration on slab penetration into the lower mantle, *Earth and Planetary Science Letters*, *140*(1-4), 27-39.

Christensen, U. R., and D. A. Yuen (1984), The interaction of a subducting lithospheric slab with a chemical or phase-boundary, *Journal of Geophysical Research*, *89*(NB6), 4389-4402.

Christensen, U. R., and D. A. Yuen (1985), Layered convection induced by phase-transitions, *Journal of Geophysical Research*, *90*(NB12), 291-300.

Cízková, H., J. van Hunen, and A. van den Berg (2007), Stress distribution within subducting slabs and their deformation in the transition zone, *Physics of the Earth and Planetary Interiors*, *161*(3-4), 202-214.

Cogné, J.-P., and E. Humler (2004), Temporal variation of oceanic spreading and crustal production rates during the last 180 My, *Earth and Planetary Science Letters*, *227*(3-4), 427-439.

Conrad, C. P., and B. H. Hager (2001), Mantle convection with strong subduction zones, *Geophysical Journal International*, *144*(2), 271-288.

Conrad, C. P., and C. Lithgow-Bertelloni (2002), How mantle slabs drive plate tectonics, *Science*, *298*(5591), 207-209.

Conrad, C. P., and C. Lithgow-Bertelloni (2004), The temporal evolution of plate driving forces: Importance of "slab suction" versus "slab pull" during the Cenozoic, *Journal of Geophysical Research*, *109*(B10), B10407.

Conrad, C. P., and C. Lithgow-Bertelloni (2007), Faster seafloor spreading and lithosphere production during the mid-Cenozoic, *Geology*, *35*(1), 29-32.

Conrad, C. P., S. Bilek, and C. Lithgow-Bertelloni (2004), Great earthquakes and slab pull: interaction between seismic coupling and plate-slab coupling, *Earth and Planetary Science Letters*, *218*(1-2), 109-122.

Cruciani, C., E. Carminati, and C. Doglioni (2005), Slab dip vs. lithosphere age: No direct function, *Earth and Planetary Science Letters*, *238*(3-4), 298-310.

Cserepes, L., D. A. Yuen, and B. A. Schroeder (2000), Effect of the mid-mantle viscosity and phase-transition structure on 3D mantle convection, *Physics of the Earth and Planetary Interiors*, *118*(1-2), 135-148.

Duffy, T. S. (2005), Synchrotron facilities and the study of the Earth's deep interior, *Reports on Progress in Physics*, *68*, 1811-1859.

Dziewonski, A. M., and D. L. Anderson (1981), Preliminary reference earth model, *Physics of the Earth and Planetary Interiors*, *25*(4), 297-356.

Elliott, T. (2003), Tracers of the slab, *In: Eiler J (ed.) Inside the Subduction Factory, Washington, D.C.: American Geophysical Union*, *138*, 23-43.

Enns, A., T. W. Becker, and H. Schmeling (2005), The dynamics of subduction and trench migration for viscosity stratification, *Geophysical Journal International*, *160*(2), 761-775.

Fei, Y., J. V. Orman, J. Li, W. vam Westrenen, C. Sanloup, W. Minarik, K. Hirose, T. Komabayashi, M. Walter, and K. Funakoshi (2004), Experimentally determined postspinel transformation boundary in Mg_2SiO_4 using MgO as an internal pressure standard and its geophysical implications, *Journal of Geophysical Research*, *109*(B02305).

Folguera, A., T. Zapata, and V. A. Ramos (2006), Late Cenozoic extension and the evolution of the Neuquén Andes, *Geological Society of America Special Papers*, *407*, 267-285.

Forsyth, D., and S. Uyeda (1975), On the relative importance of the driving forces of plate motion, *Geophysical Journal of the Royal Astronomical Society*, *43*(1), 163-200.

Frost, D. J. (2008), The upper mantle and transition zone, *Elements*, *4*(3), 171-176.

Fukao, Y., S. Widiyantoro, and M. Obayashi (2001), Stagnant slabs in the upper and lower mantle transition region, *Review of Geophysics*, *39*(3), 291-323.

Funiciello, F., G. Morra, K. Regenauer-Lieb, and D. Giardini (2003), Dynamics of retreating slabs: 1. Insights from two-dimensional numerical experiments, *Journal of Geophysical Research*, *108*(B4), 2206.

Gaherty, J. B., and B. H. Hager (1994), Compositional vs thermal buoyancy and the evolution of subducted lithosphere, *Geophysical Research Letters*, *21*(2), 141-144.

Grand, S. P. (1994), Mantle shear structure beneath the Americas and surrounding oceans, *Journal of Geophysical Research*, *99*(B6), 11591-11621.

Griffiths, R. W., and J. S. Turner (1988), Folding of Viscous Plumes Impinging On A Density Or Viscosity Interface, *Geophysical Journal*, *95*(2), 397-419.

Guillou-Frottier, L., J. Buttles, and P. Olson (1995), Laboratory experiments on the structure of subducted lithosphere, *Earth and Planetary Science Letters*, *133*(1-2), 19-34.

Gurnis, M., and B. H. Hager (1988), Controls of the structure of subducted slabs, *Nature*, *335*(6188), 317-321.

Hager, B. H. (1984), Subducted slabs and the geoid - constraints on mantle rheology and flow, *Journal of Geophysical Research*, *89*(NB7), 6003-&.

Han, L. J., and M. Gurnis (1999), How valid are dynamic models of subduction and convection when plate motions are prescribed?, *Physics of the Earth and Planetary Interiors*, *110*(3-4), 235-246.

Hirth, G., and D. Kohlstedt (2003), Rheology of the upper mantle and the mantle wedge: A View from the Experimentalists, *in Inside the Subduction Factory, Geophysical Monograph*, *138*, 83-105, *American Geophysical Union, Washington D.C.*

Hofmeister, A. M. (1999), Mantle values of thermal conductivity and the geotherm from phonon lifetimes, *Science*, *283*(5408), 1699-1706.

Hughes, T. (1987), The Finite Element Method: Linear Static and Dynamics Finite Element Analysis, *Prentice-Hall, Englewood Cliffs, New Jersey*

Hughes, T. J. R., and A. Brooks (1979), 'A multidimensional upwind scheme with no crosswind diffusion', in T. J. R. Hughes, ed., *Finite element methods for convection dominated flows, AMD, 34*, 19-35,

Presented at the Winter Annual Meeting of the ASME, Amer. Soc. Mech. Engrs. (ASME), New York.

Ita, J., and S. D. King (1994), Sensitivity of convection with an endothermic phase change to the form of governing equations, initial conditions, boundary conditions, and equation of state, *Journal of Geophysical Research*, *99*(B8), 15919-15938.

Ita, J., and S. D. King (1998), The influence of thermodynamic formulation on simulations of subduction zone geometry and history, *Geophysical Research Letters*, *25*(9), 1463-1466.

Ito, E., and E. Takahashi (1989), Postspinel Transformations in the System Mg_2SiO_4-$FeSiO_4$ and Some Geophysical Implications, *Journal of Geophysical Research*, *94*(B8), 10637-10646.

Ito, Y., and M. Toriumi (2007), Pressure effect of self-diffusion in periclase (MgO) by molecular dynamics, *Journal of Geophysical Research*, *112*(B4), B04206.

Jarrard, R. D. (1986), Relations among subduction parameters, *Review of Geophysics*, *24*, 217-284.

Jarvis, G., and D. McKenzie (1980), Convection in a compressible fluid with infinite Prandtl number, *Journal of Fluid Mechanics*, *96*(515-583).

Jordan, T. E., W. M. Burns, R. Veiga, F. Pángaro, P. Copeland, S. Kelley, and C. Mpodozis (2001), Extension and basin formation in the southern Andes caused by increased convergence rate: A mid-Cenozoic trigger for the Andes, *Tectonics*, *20*(3), 308-324.

Karason, H., and R. D. van der Hilst (2001), Tomographic imaging of the lowermost mantle with differential times of refracted and diffracted core phases (PKP, P-diff), *Journal of Geophysical Research*, *106*(B4), 6569-6587.

Karato, S.-i. (2010), Rheology of the Earth's mantle: A historical review, *Gondwana Research*, *18*(1), 17-45.

Karato, S.-I., and P. Wu (1993), Rheology of the upper mantle: a synthesis, *Science*, *260*, 771-778.

Kay, S. M. (2002), Tertiary to Recent transient shallow subduction zones in the Central and Southern Andes., *Actas, Congreso Geológico Argentino, 15 CD ROM, Archivos Electrónicos, Artículo, 237: El Calafate, 2 p.*

Kay, S. M., E. Godoy, and A. Kurtz (2005), Episodic arc migration, crustal thickening, subduction erosion, and magmatism in the south-central Andes, *Geological Society of America Bulletin*, *117*(1-2), 67-88.

Kay, S. M., W. M. Burns, P. Copeland, and O. Mancilla (2006), Upper Cretaceous to Holocene magmatism and evidence for transient Miocene shallowing of the Andean subduction zone under the northern Neuquén Basin, *Geological Society of America Special Papers*, *407*, 19-60.

King, S. D. (1995), The viscosity structure of the mantle, *Reviews of Geophysics*, *33*, 11-17.

King, S. D. (2001), Subduction zones: observations and geodynamic models, *Physics of the Earth and Planetary Interiors*, *127*(1-4), 9-24.

King, S. D. (2002), Geoid and topography over subduction zones: The effect of phase transformations, *Journal of Geophysical Research-Solid Earth*, *107*(B1).

King, S. D. (2007), Mantle Downwellings and the Fate of Subducting Slabs: Constraints from Seismology, Geoid Topography, Geochemistry, and Petrology, in *Treatise on Geophysics*, edited by S. Gerald, pp. 325-370, Elsevier, Amsterdam.

King, S. D., and G. Masters (1992), An inversion for radial viscosity structure using seismic tomography, *Geophysical Research Letters*, *19*(15), 1551-1554.

King, S. D., and B. H. Hager (1994), Subducted slabs and the geoid. 1. Numerical experiments with temperature-dependent viscosity, *Journal of Geophysical Research*, *99*(B10), 19843-19852.

King, S. D., and J. Ita (1995), Effect of slab rheology on mass-transport across a phase-transition boundary, *Journal of Geophysical Research*, *100*(B10), 20211-20222.

King, S. D., A. Raefsky, and B. H. Hager (1990), Conman: vectorizing a finite element code for incompressible two-dimensional convection in the Earth's mantle, *Physics of the Earth and Planetary Interiors*, *59*(3), 195-207.

King, S. D., C. Lee, P. E. v. Keken, W. Leng, S. Zhong, E. Tan, N. Tosi, and M. C. Kameyama (2010), A community benchmark for 2-D Cartesian compressible convection in the Earth's mantle, *Geophysical Journal International*, *180*(1), 73-87.

Kneller, E. A., P. E. van Keken, I. Katayama, and S. Karato (2007), Stress, strain, and B-type olivine fabric in the fore-arc mantle: Sensitivity tests using high-resolution steady-state subduction zone models, *Journal of Geophysical Research*, *112*(B4), doi: 10.1029/2006JB004544.

Kohlstedt, D. L., B. Evans, and S. J. Mackwell (1995), Strength of the lithosphere: Constraints imposed by laboratory experiments, *Journal of Geophysical Research*, *100*(B9), 17587-17602.

Larson, R. L. (1991), Latest pulse of Earth: Evidence for a mid-Cretaceous superplume, *Geology*, *19*(6), 547-550.

Lay, T., E. J. Garnero, and Q. Williams (2004), Partial melting in a thermo-chemical boundary layer at the base of the mantle, *Physics of The Earth and Planetary Interiors*, *146*(3-4), 441-467.

Lee, C., and S. D. King (2009), Effect of mantle compressibility on the thermal and flow structures of the subduction zones, *Geochemistry Geophysics Geosystems*, *10*(Q01006), doi: 10.1029/2008GC002151.

Lee, C., and S. D. King (2010), Why are high-Mg# andesites widespread in the western Aleutians? A numerical model approach, *Geology*, *38*(7), 583-586.

Leng, W., and S. Zhong (2008), Viscous heating, adiabatic heating and energetic consistency in compressible mantle convection, *Geophysical Journal International*, *173*, 693-702.

Li, C., R. D. van der Hilst, E. R. Engdahl, and S. Burdick (2008), A new global model for P wave speed variations in Earth's mantle, *Geochemistry Geophysics Geosystems*, *9*(5), Q05018, doi: 10.1029/2007gc001806.

Lithgow-Bertelloni, C., and M. A. Richards (1998), The dynamics of Cenozoic and Mesozoic plate motions, *Review of Geophysics*, *36*(1), 27-78.

Liu, W., and B. Li (2006), Thermal equation of state of $(Mg_{0.9}Fe_{0.1})_2SiO_4$ olivine, *Physics of the Earth and Planetary Interiors*, *157*(3-4), 188-195.

Mitrovica, J. X., and A. M. Forte (2004), A new inference of mantle viscosity based upon joint inversion of convection and glacial isostatic adjustment data, *Earth and Planetary Science Letters*, *225*(1-2), 177-189.

Olbertz, D., M. J. R. Wortel, and U. Hansen (1997), Trench migration and subduction zone geometry, *Geophysical Research Letter*, *24*(3), 221-224.

Parmentier, E., D. Turcotte, and K. Torrance (1976), Studies of finite amplitude non-Newtonian thermal convection with application to convection in the Earth's mantle, *Journal of Geophysical Research*, *81*(11), 1839-1846.

Ranalli, G. (1991), The microphysical approach to mantle rheology, *In: Sabadini, R., Lambeck, K., Boschi, E. (Eds.), Glacial Isostacy, Sea-Level and Mantle Rheology*, 343-378.

Ranalli, G. (2001), Mantle rheology: radial and lateral viscosity variations inferred from microphysical creep laws, *Journal of Geodynamics*, *32*(4-5), 425-444.

Ren, Y., E. Stutzmann, R. D. van der Hilst, and J. Besse (2007), Understanding seismic heterogeneities in the lower mantle beneath the Americas from seismic tomography and plate tectonic history, *Journal of Geophysical Research*, *112*(B1), B01302, doi: 10.1029/2005jb004154.

Ribe, N. M. (2003), Periodic folding of viscous sheets, *Physical Review E*, *68*(3), 036305.

Ribe, N. M., E. Stutzmann, Y. Ren, and R. van der Hilst (2007), Buckling instabilities of subducted lithosphere beneath the transition zone, *Earth and Planetary Science Letters*, *254*(1-2), 173-179.

Richter, F. M. (1973), Dynamical models for sea floor spreading, *Review of Geophysics*, *11*(2), 223-287.

Riedel, M. R., and S.-i. Karato (1997), Grain-size evolution in subducted oceanic lithosphere associated with the olivine-spinel transformation and its effects on rheology, *Earth and Planetary Science Letters*, *148*(1-2), 27-43.

Schellart, W. P. (2005), Influence of the subducting plate velocity on the geometry of the slab and migration of the subduction hinge, *Earth and Planetary Science Letters*, *231*(3-4), 197-219.

Schubert, G., D. L. Turcotte, and P. Olson (2001), Mantle Convection in the Earth and Planets, *Cambridge University Press, Cambridge*.

Sdrolias, M., and R. D. Müller (2006), Controls on back-arc basin formation, *Geochemistry Geophysics Geosystems*, *7*(Q04016), doi:10.1029/2005GC001090.

Stein, C. A., and S. Stein (1992), A model for the global variation in oceanic depth and heat flow with lithospheric age, *Nature*, *359*(6391), 123-129.

Stepashko, A. (2008), Spreading cycles in the Pacific Ocean, *Oceanology*, *48*(3), 401-408.

Stern, R. J. (2002), Subduction zones, *Review of Geophysics*, *40*(4), 1012.

Syracuse, E. M., and G. A. Abers (2006), Global compilation of variations in slab depth beneath arc volcanoes and implications, *Geochemistry Geophysics Geosystems*, *7*(Q05017), doi:10.1029/2005GC001045.

Tackley, P. J. (1995), Mantle dynamics - influence of the transition zone, *Reviews of Geophysics*, *33*, 275-282.

Tackley, P. J. (2000), Self-consistent generation of tectonic plates in time-dependent, three-dimensional mantle convection simulations, *Geochemistry Geophysics Geosystems*, *1*(8), doi: 10.1029/2000gc000043.

Taylor, G. I. (1968), Instability of jets, threads, and sheets of viscous fluid, *Proc. Twelfth Int. Cong. Appl. Mech. Springer Verlag, Berlin*.

Tome, M. F., and S. McKee (1999), Numerical simulation of viscous flow: Buckling of planar jets, *International Journal for Numerical Methods in Fluids*, *29*(6), 705-718.

Tosi, N., O. adek, Z. Martinec, D. A. Yuen, and G. Kaufmann (2009), Is the long-wavelength geoid sensitive to the presence of postperovskite above the core-mantle boundary?, *Geophysical Research Letter*, *36*(5), L05303, doi: 10.1029/2008gl036902.

van Keken, P. E. (2003), The structure and dynamics of the mantle wedge, *Earth and Planetary Science Letters*, *215*(3-4), 323-338.

Williams, C. F., F. V. Grubb, and S. P. Galanis, Jr. (2004), Heat flow in the SAFOD pilot hole and implications for the strength of the San Andreas Fault, *Geophysical Research Letter*, *31*(15), L15S14, doi: 10.1029/2003gl019352.

Wu, B., C. P. Conrad, A. Heuret, C. Lithgow-Bertelloni, and S. Lallemand (2008), Reconciling strong slab pull and weak plate bending: The plate motion constraint on the strength of mantle slabs, *Earth and Planetary Science Letters*, *272*(1-2), 412-421.

Zhong, S. J., and M. Gurnis (1995), Mantle convection with plates and mobile, faulted plate margins, *Science*, *267*(5199), 838-843.

Zhong, S. J., and G. F. Davies (1999), Effects of plate and slab viscosities on the geoid, *Earth and Planetary Science Letters*, *170*(4), 487-496.

Table 4.1 Model parameters

Symbol	Parameter	Value
ρ_0 (kg/m^3)	Density	3300.0
$\overline{\rho}_{410}$(kg/m^3)	Reference density at 410 km	3300.0 (incompressible model) 3595.0 (compressible model)
$\overline{\rho}_{660}$(kg/m^3)	Reference density at 660 km	3300.0 (incompressible model) 3986.0 (compressible model)
$\delta\rho_{410}$(%)	Density increase at 410 km	5
$\delta\rho_{660}$(%)	Density increase at 660 km	9
$P_{t,410}$ (Pa)	Pressure for phase transition at 410 km depth	1.370×10^{10}
$P_{t,660}$ (Pa)	Pressure for phase transition at 660 km depth	2.291×10^{10}
$T_{t,410}$ (K)	Temperature for phase transition at 410 km depth	1789.0
$T_{t,660}$ (K)	Temperature for phase transition at 660 km depth	1866.7
g_0 (m/s^2)	Gravitational acceleration	9.81
α_0 (/K)	Thermal expansivity	2×10^{-5}
C_P (J/kg.K)	Heat capacity	1200
d (m)	Domain thickness	2890×10^3
d_L (m)	Phase loop	2.0×10^4
η_0 (Pa.s)	Reference viscosity	10^{22}
κ_0 (m^2/s)	Thermal diffusivity	1×10^{-6}
T_0 (K)	Surface temperature	273
T_{bottom}(K)	Bottom temperature	2683.53
$T_{potential}$(K)	Mantle potential temperature	1673
$\overline{T}_{bottom}$(K)	Adiabatic temperature at the bottom	1010.53
ΔT (K)	Temperature difference	2410.53
Di	Dissipation number	0.472515
Γ	Grüneisen's parameter	1.1
H (W/kg)	Rate of radiogenic heat production	7.38×10^{-12}
Ra	Rayleigh number	3.767204×10^6

Table 4.2 Rheological parameters

Symbol	Parameter	Value
$\sigma_{brittle}$ (GPa)	Brittle strength	10
$\sigma_{ductile}$ (GPa)	Ductile strength	0.5
A_{dif} ($m^{2.5}$/Pa·s)	Prefactor (dif)	6.10×10^{-19}
A_{dis} ($s^{1.5}$/$Pa^{3.5}$)	Prefactor (dis)	2.40×10^{-16}
E_{dif} (J/mol)	Activation energy (dif)	2.40×10^{5}
E_{dis} (J/mol)	Activation energy (dis)	4.32×10^{5}
$V_{dif,\ 0\ km}$ (m^3/mol)	Activation volume at 0 km (dif)	6.00×10^{-6}
$V_{dif,\ 660\ km}$ (m^3/mol)	Activation volume at 660 km (dif)	4.20×10^{-6}
$V_{dis,\ 0\ km}$ (m^3/mol)	Activation volume at 0 km (dis)	1.50×10^{-5}
$V_{dis,\ 660\ km}$ (m^3/mol)	Activation volume at 660 km (dis)	1.05×10^{-5}
$V_{dif,\ LM}$ (m^3/mol)	Activation volume of lower mantle (dis)	1.80×10^{-6}
$d_{g,\ UM}$ (m)	Grain size for the upper mantle (UM)	1.00×10^{-3}
$d_{g,\ LM,}$ (m)	Grain size for the lower mantle (LM)	0.83×10^{-2} (4-fold) 1.45×10^{-2} (16-fold) 1.92×10^{-2} (32-fold) 2.25×10^{-2} (48-fold) 2.52×10^{-2} (64-fold) 2.76×10^{-2} (80-fold) 2.97×10^{-2} (96-fold) 3.16×10^{-2} (112-fold) 3.33×10^{-2} (128-fold)
n	Stress exponent (dis)	3.5
m	Grain size exponent (dif)	2.5
R (J/mol)	Gas constant	8.314

dif: diffusion creep, dis: dislocation creep, UM: upper mantle, LM: lower mantle

Table 4.3 Slab buckling parameters for the experiments using a maximum slab viscosity of 10^{24} Pa.s

η_{Inc}	Buckling period (Myr)	$\Delta\rho g$ (N/m^3)	η_{slab} (Pa.s)	U_0 (cm/y)	d (km)	H_0 (km)	B	Π	$\delta_{calculated}$ *(km)*	$\delta_{measured}$ *(km)*	*T' (T* Myr*)*
4	No buckling										
16	No buckling										
32	Minor and non-periodic buckling										
48	44-89	304.26	$9.a72\times10^{22}$	3.91	94.08	653.47	1.08	2.76	411.40	409.21, 361.82	1.41 (23.6), 1.23 (20.5)
64	45-90	303.61	9.67×10^{22}	3.70	97.80	649.17	1.13	2.73	412.61	433.08, 426.70	1.45 (25.5), 1.16 (20.4)
80	46-119	301.40	8.94×10^{22}	3.52	96.59	650.57	1.28	2.83	412.22	420.15, 444.66, 384.31	1.51 (27.9), 1.22 (22.6), 1.19 (22.0)
96	48-125	302.27	8.35×10^{22}	3.31	99.83	646.83	1.44	2.86	413.26	419.65, 460.55, 421.04	1.44 (28.2), 1.34 (26.2), 1.13 (22.1)
112	50-131	301.26	7.87×10^{22}	2.97	99.83	646.83	1.70	2.98	413.26	431.91, 443.59, 414.69	1.41 (30.7), 1.20 (26.0), 1.08 (23.4)
128	53-142	300.66	7.32×10^{22}	2.77	101.23	645.21	1.94	3.06	413.71	445.54, 448.31, 396.87	1.40 (32.5), 1.26 (29.3), 1.15 (26.8)

η_{Inc}: viscosity increase, $\Delta\rho g$: mean slab buoyancy, η_{slab}: mean slab viscosity, U_0: mean convergence rate, d: mean slab thickness, H_0 : distance between slab input and the center of the buckled slab at the 660 km discontinuity, B : buoyancy number, $\delta_{calculated}$: theoretical amplitude of buckling, $\delta_{measured}$: measured buckling amplitude, *T' (T)*: dimensionless period and corresponding period of buckling (1.218 for pure forced folding). Calculations of the mean parameters are based on the buckling period. Multiple values for $\delta_{measured}$ and *T' (T)* correspond to each cycles of slab buckling.

Table 4.4 Slab buckling parameters for kinematic and dynamic subduction experiments using a maximum slab viscosity of 10^{24} Pa.s D: dynamic subduction experiment, K: kinematic subduction experiment

η_{Inc}	Buckling period (Myr)	$\Delta\rho g$ (N/m^3)	η_{slab} (Pa.s)	U_0 (cm/y)	d (km)	H_0 (km)	B	Π	$\delta_{calculated}$ *(km)*	$\delta_{measured}$ *(km)*	*T' (T* Myr*)*
16 (D)	No buckling										
16 (K)	No buckling										
48 (D)	44-89	304.26	9.72×10^{22}	3.91	94.08	653.47	1.08	2.76	411.40	409.21, 361.82	1.41 (23.6), 1.23 (20.5)
48 (K)	44-80	314.63	1.23×10^{23}	3.80	88.59	659.81	0.92	2.75	409.63	438.10	1.33 (23.1)
80 (D)	46-119	301.40	8.94×10^{22}	3.52	96.59	650.57	1.28	2.83	412.22	420.15, 444.66, 384.31	1.51 (27.9), 1.22 (22.6), 1.19 (22.0)
80 (K)	46-100	313.67	9.25×10^{22}	3.38	90.58	657.51	1.37	2.99	410.28	439.88, 445.66	1.38 (26.8), 1.28 (24.8)

Table 4.5 Slab buckling parameters for the experiments using a maximum slab viscosity of 10^{26} Pa.s

η_{Inc}	Buckling period (Myr)	$\Delta\rho g$ (N/m^3)	η_{slab} (Pa.s)	U_0 (cm/y)	d (km)	H_0 (km)	B	Π	$\delta_{calculated}$ *(km)*	$\delta_{measured}$ *(km)*	*T' (T* Myr*)*
4	No buckling										
16	No buckling										
32	Minor and non-periodic buckling										
48	Minor and non-periodic buckling										
64	51-104	302.86	5.90×10^{24}	3.14	97.56	649.45	0.02	0.99	422.28	432.80, 374.71	1.37 (28.3), 1.21 (25.0)
80	52-133	301.83	5.38×10^{24}	2.99	97.12	649.96	0.02	1.03	422.10	452.59, 400.57, 347.39	1.38 (30.0), 1.05 (22.9), 1.26 (27.3)
96	54-142	301.09	4.69×10^{24}	2.63	100.82	645.69	0.03	1.07	423.66	425.08, 382.70, 340.20	1.34 (33.0), 1.21 (29.7), 0.99 (24.4)
112	56-147	299.48	4.65×10^{24}	2.52	101.16	645.29	0.03	1.08	423.81	427.16, 400.28, 370.97	1.35 (34.6), 1.04 (26.6), 1.15 (29.5)
128	59-153	287.99	4.14×10^{24}	2.52	99.75	646.92	0.04	1.11	423.21	442.80, 457.39, 399.04	1.47 (37.7), 1.14 (29.1), 1.04 (26.7)

Table 4.6 Slab buckling parameters for the experiments using a maximum slab viscosity of 10^{24} Pa.s and phase transitions

η_{Inc}	Buckling period (Myr)	$\Delta\rho g$ (N/m^3)	η_{slab} (Pa.s)	U_0 (cm/y)	d (km)	H_0 (km)	B	Π	$\delta_{calculated}$ *(km)*	$\delta_{measured}$ *(km)*	*T' (T* Myr*)*
4	No buckling										
16	18-41	317.32	1.32×10^{23}	12.54	104.44	641.50	0.25	1.75	425.19	477.25	1.51 (7.72)
				11.14	95.84	651.43	0.29	1.91	421.56	443.22	1.20 (7.02)
				13.14	87.65	660.89	0.30	2.15	418.10	379.83	1.39 (7.01)
32	22-57	311.92	1.01×10^{23}	8.45	103.49	642.60	0.48	2.07	421.31	485.55	1.28 (9.76)
				8.44	94.93	652.48	0.49	2.20	421.17	456.76	1.18 (9.09)
				11.34	87.24	661.37	0.38	2.16	417.92	435.19	1.35 (7.85)
				11.01	80.49	669.16	0.40	2.29	415.98	405.62	1.15 (7.00)
48	27-77	310.67	8.84×10^{22}	7.13	104.34	641.63	0.64	2.22	425.15	471.94	1.31 (11.81)
				7.05	95.85	651.43	0.67	2.36	421.56	466.06	1.23 (11.40)
				8.20	87.93	660.57	0.59	2.40	418.22	447.73	1.27 (10.27)
				8.52	81.15	668.40	0.58	2.51	415.35	416.39	1.05 (8.26)
				11.21	75.44	674.99	0.45	2.45	412.94	411.26	1.22 (7.35)
64	30-97	309.76	7.69×10^{22}	5.56	103.94	642.08	0.94	2.45	424.98	477.62	1.26 (14.55)
				6.23	95.79	651.49	0.86	2.51	421.54	475.25	1.34(14.03)
				6.34	88.29	660.15	0.87	2.64	418.37	462.54	1.18 (12.28)
				7.71	81.94	667.48	0.73	2.64	415.69	430.48	1.15 (9.97)
				8.62	76.64	673.61	0.67	2.68	413.44	399.74	1.11 (8.64)
				10.27	72.29	678.63	0.57	2.66	411.60	369.67	1.00 (6.63)

Table 4.7 Slab buckling parameters for the experiments using a maximum slab viscosity of 10^{24} Pa.s (Compressible model)

η_{Inc}	Buckling period (Myr)	$\Delta\rho g$ (N/m^3)	η_{slab} (Pa.s)	U_0 (cm/y)	d (km)	H_0 (km)	B	Π	$\delta_{calculated}$ *(km)*	$\delta_{measured}$ *(km)*	*T' (T* Myr*)*
4	No buckling										
16	No buckling										
32	No buckling										
48	Minor and non-periodic buckling										
64	No systematic buckling										
80	52-119	339.98	7.98×10^{22}	3.76 3.82 3.95	87.71	660.83	1.56 1.53 1.51	3.07 3.05 3.04	412.22	433.06, 379.31, 426.99	1.34 (23.5), 1.31 (22.6), 1.22 (20.7)
96	50-143	340.96	7.70×10^{22}	3.46 3.52 3.95 4.50 4.93	87.38	661.20	1.76 1.73 1.54 1.36 1.24	3.17 3.16 3.07 2.97 2.90	413.26	418.87, 352.39, 313.96, 439.67, 324.65	1.39 (26.5), 1.23 (23.1), 1.06 (17.7), 1.02 (15.0), 0.83 (11.2)
112	49-151	334.82	7.12×10^{22}	3.12 3.22 3.62 4.22 4.62	87.37	661.22	2.08 2.01 1.79 1.54 1.40	3.30 3.28 3.18 3.06 2.99	413.26	410.47, 361.63, 421.59, 431.13, 408.59	1.39 (29.4), 1.41 (29.0), 0.93 (16.9), 1.12 (17.6), 0.78 (11.2)
128	51-164	330.14	6.95×10^{22}	2.88 2.97 3.43 3.82 4.21	89.67	658.56	2.26 2.18 1.89 1.70 1.54	3.32 3.29 3.18 3.09 3.02	413.71	406.13, 373.76, 439.65, 424.91, 494.84	1.40 (32.0), 1.37 (30.3), 1.01 (19.4), 1.17 (20.2), 0.72 (11.2)

Figure 4.1

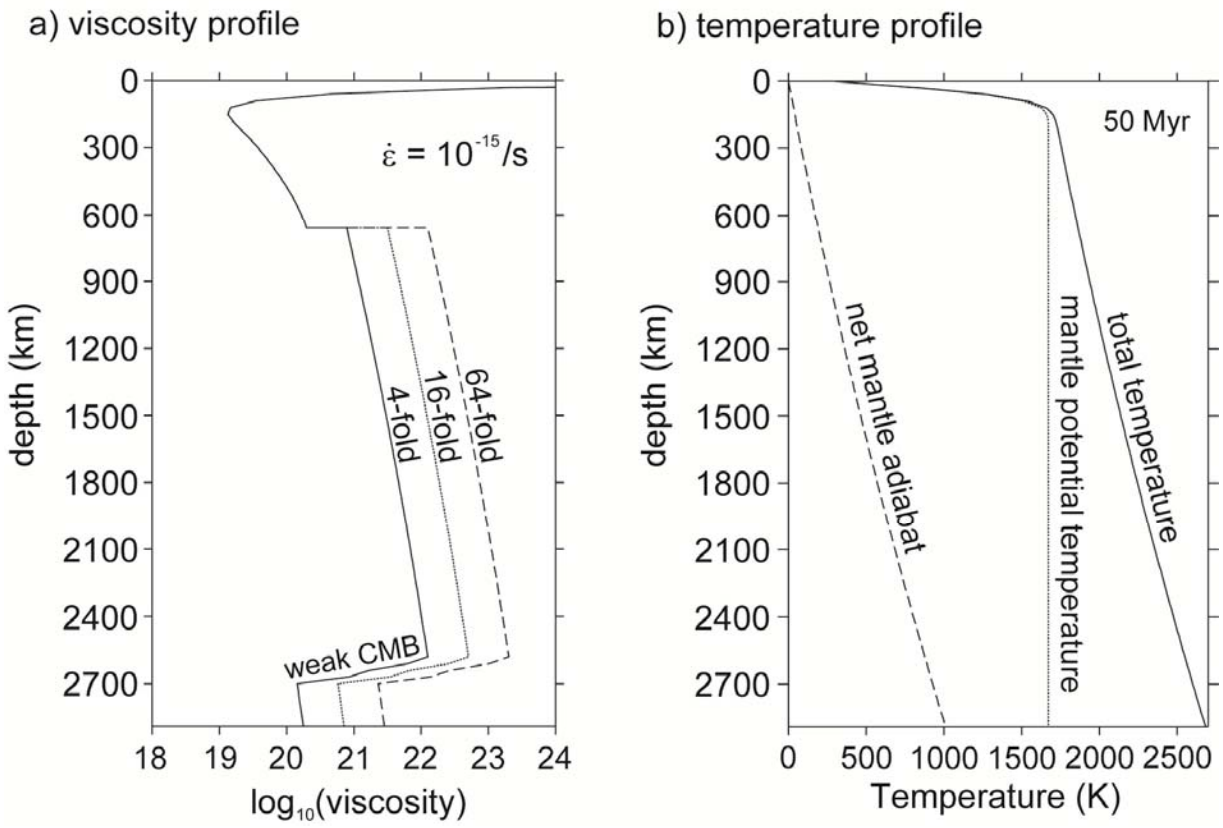

Initial viscosity (a) and temperature profiles (b) used in this study. The viscosity profiles correspond to 4-, 16- and 64-fold viscosity increases with the low viscosity CMB for a 50 Myr old oceanic lithosphere plus net mantle adiabat. The other viscosity profiles for the higher viscosity increases are omitted for clarity. For the viscosity profiles of the upper mantle, activation volumes of the diffusion and dislocation creep are assumed to linearly decrease with depth by 30% at the 660 km discontinuity (Table 2). To calculate the viscosity of dislocation creep, a strain rate of 10^{-15}/s is used. The activation volume of the lower mantle is constant regardless of depth. Viscosity increases across the 660 km discontinuity are calculated by using grain sizes described in Table 2. Pressure and temperature for the viscosity calculation are updated each time step. The net mantle adiabat is based on the Adams-Williamson equation and kept constant during the entire experiment run.

Figure 4.2

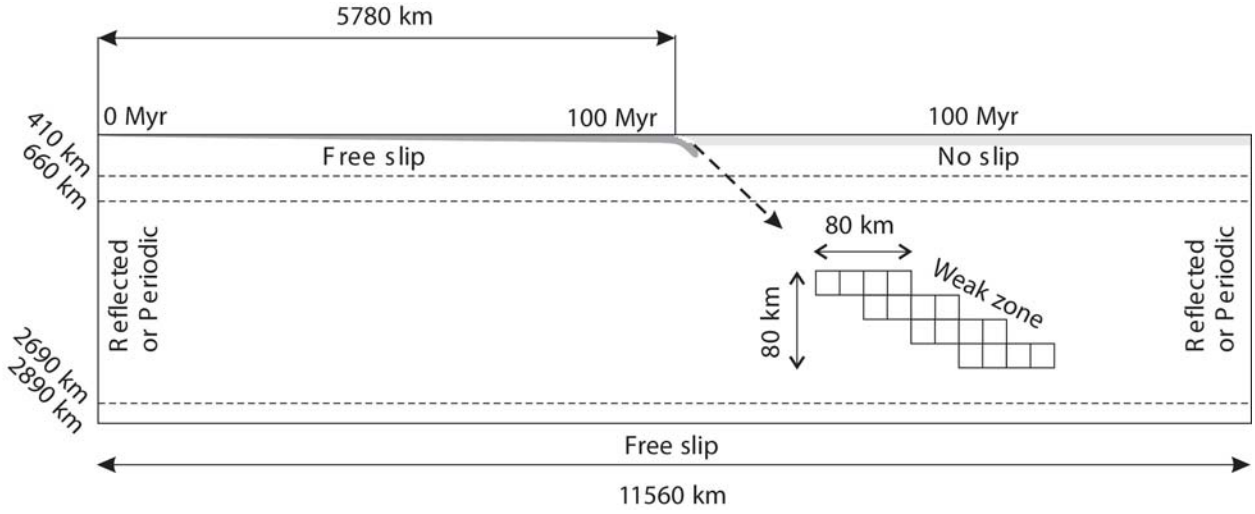

Schematic diagram of the dynamic subduction model. The weak zone consists of 16 elements and is used to approximate the thrust between the subducting slab and overriding plate. The dashed lines correspond to 410, 660 and 2690 km depths.

Figure 4.3

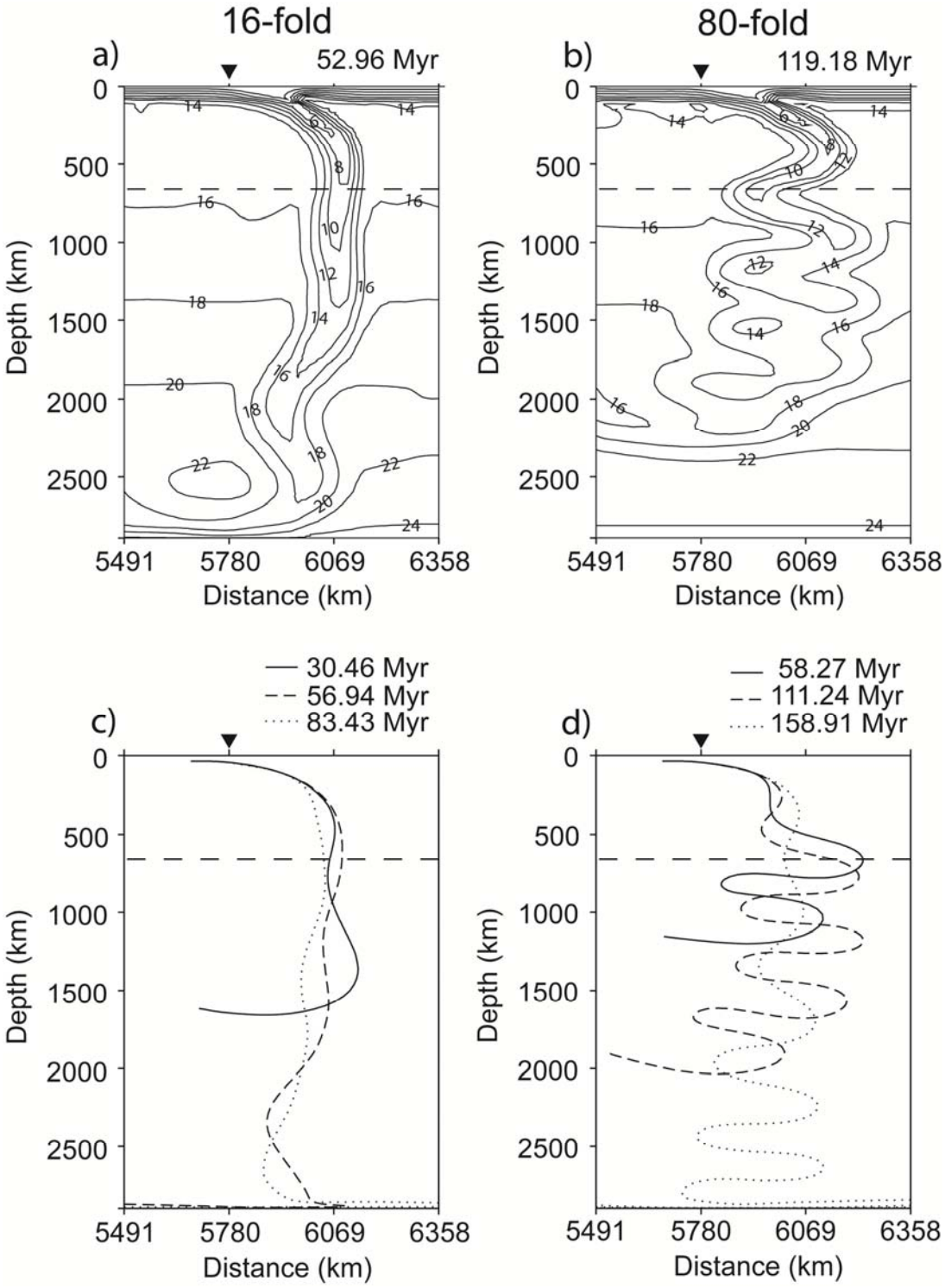

Snapshots of slab temperatures (a and b) and trajectories (c and d) corresponding to the experiments using 16- and 80-fold viscosity increases. Distance is measured from the left-wall boundary of the model

domain and exaggerated 2.3 times for a better viewing. The dashed horizontal line corresponds to the 660 km discontinuity. An interval of 200 ˚C is used for depicting slab temperatures (for a better view, the temperatures are divided by 100). The unit for slab temperatures is Celsius. The slab trajectories are depicted by linking tracers which are implemented along the mid-surface of the converging oceanic plate. Initially, 2000 tracers are implemented at 35 km depth and 110 km away from the trench and each tracer is released every 0.1 Myr.

Figure 4.4

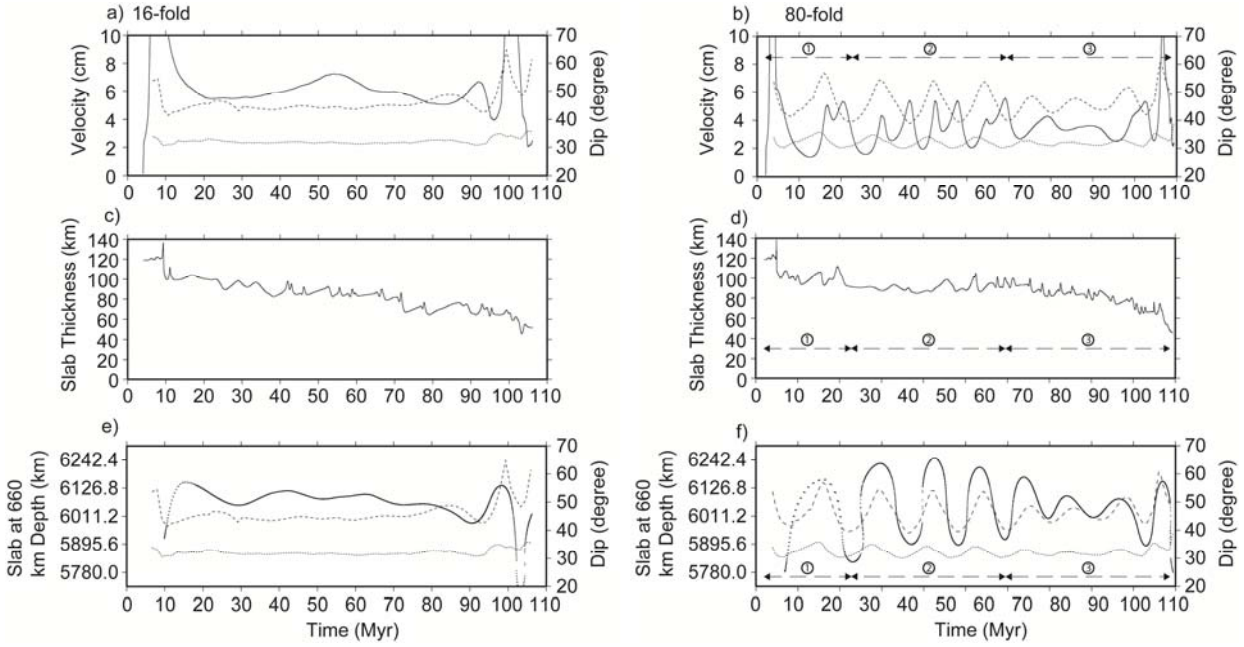

Convergence rate, slab thickness and time-evolving lateral amplitude of the subducting slab at the 660 km discontinuity corresponding to the experiments using 16- and 80-fold viscosity increases. The fine and coarse dashed lines correspond to the dip of the subducting slab at 150 and 300 km depth, respectively. The dip of the subducting slab varies with depth due to its arc-shape curvature; thus the dip is estimated by measuring the dip of the line linking the 35 km depth at the trench with 150 (300) km depth in the mid-surface of the subducting slab. The boundaries for the three phases are somewhat arbitrarily defined because the transitions between the phases are continuous. We assume the first local trough of the amplitude of the slab as the boundary between the phase 1 and 2, which is the starting point of the steady-state slab buckling. For the boundary between the phase 2 and 3, we assume the last local trough of the amplitude of the slab after which release of the stacked slab occurs. The dots indicate x-coordinates of the subducting slab crossing the 660 km discontinuity with time.

Figure 4.5

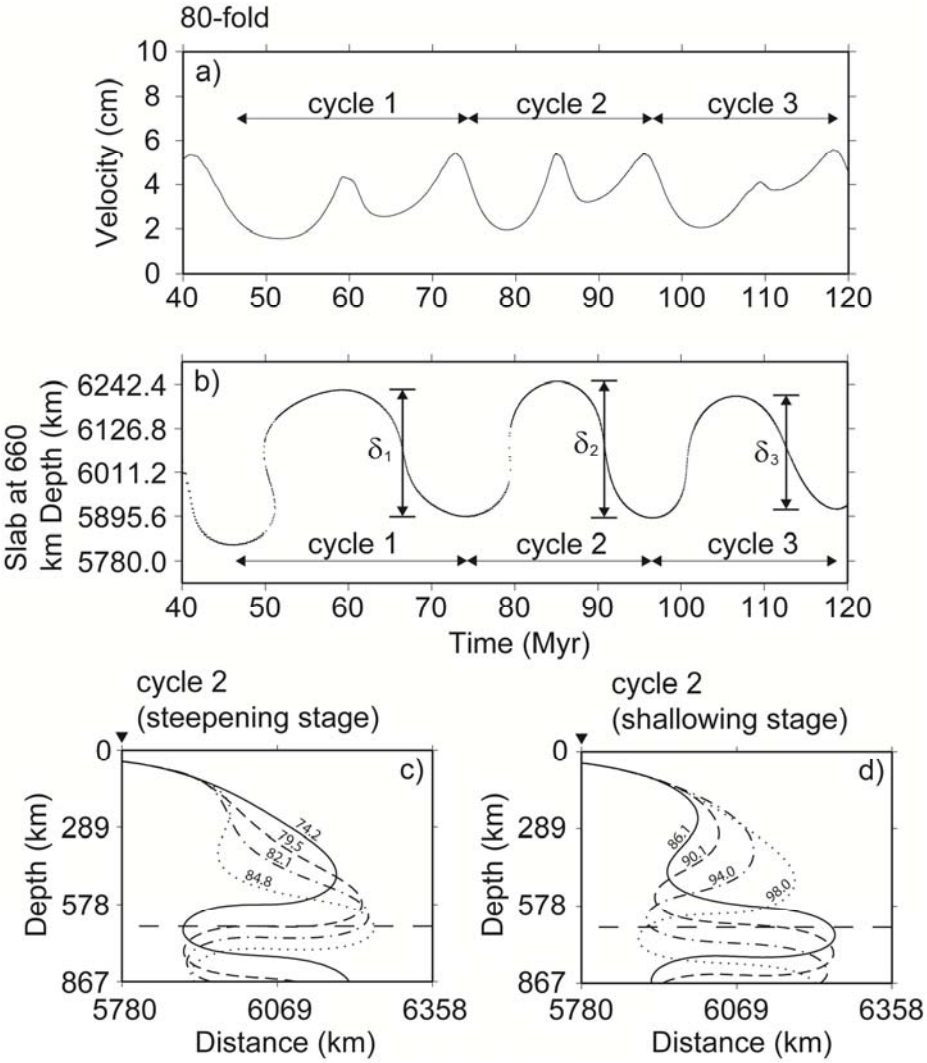

Convergence rate and time-evolving amplitude of the subducting slab at the 660 km discontinuity corresponding to the experiment using an 80-fold viscosity increase in the steady-state slab buckling phase. Each cycle is defined by using the local lowest amplitudes (b). Because the amplitude of each cycle varies with time, the amplitude of the slab is measured by gauging the distance between the local peak and trough plus the slab thickness. Each cycle consists of steepening and shallowing stages; c and d show the steepening and shallowing stages for the cycle 2, respectively. For a better viewing, the distance is exaggerated 2 times. The numbers on the slab trajectories indicate elapsed time (Myr) since the initiation of subduction.

Figure 4.6

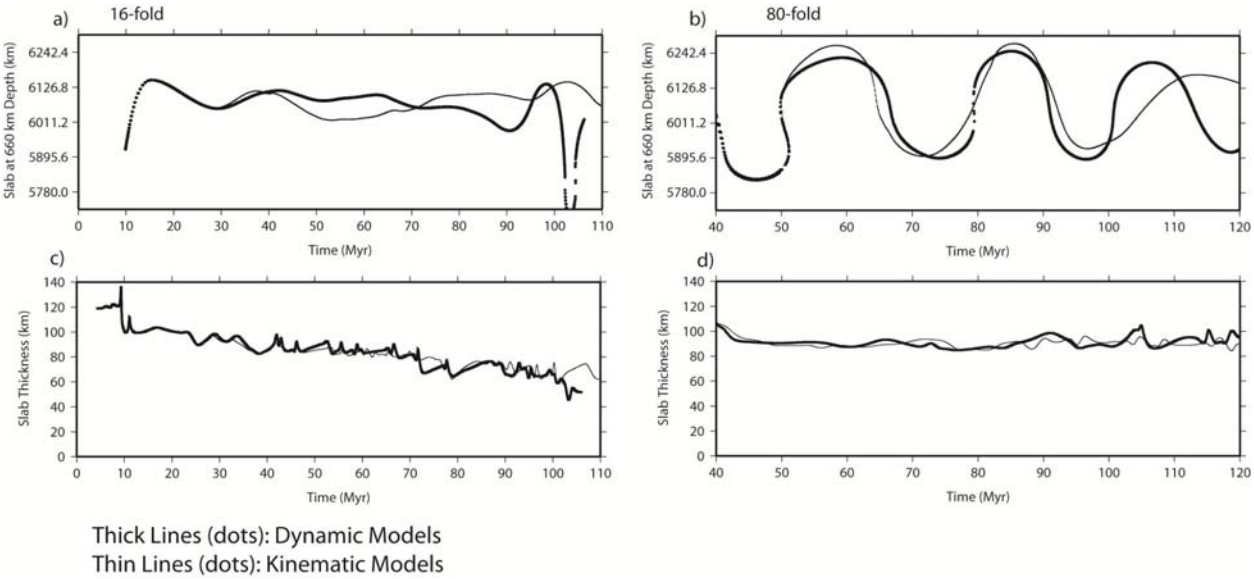

Time-evolving amplitude of the subducting slab at the 660 km discontinuity (a and b) and slab thickness (c and d) corresponding to the dynamic and kinematic subduction experiments using 16- and 80-fold viscosity increases.

Figure 4.7

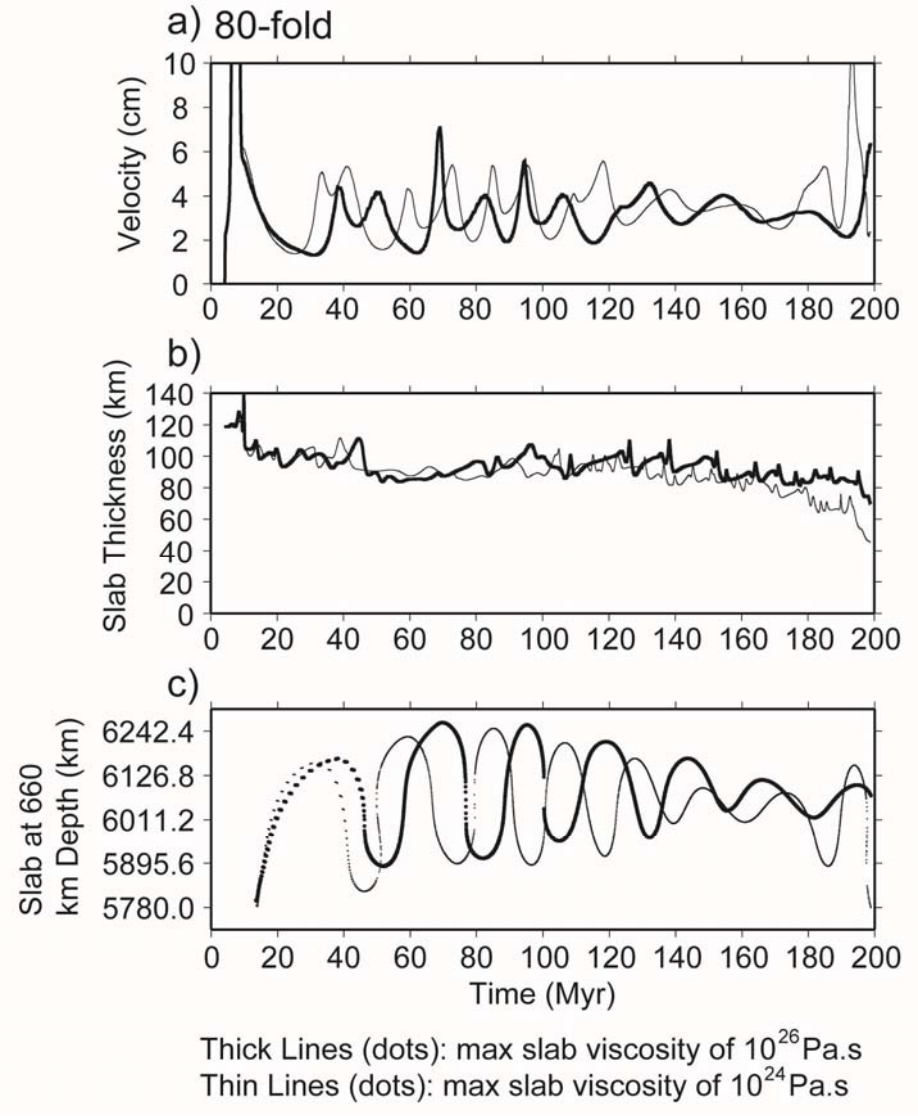

Convergence rate, slab thickness and time-evolving lateral amplitude of the subducting slab at the 660 km discontinuity corresponding to the experiment using an 80-fold viscosity increase with a maximum slab viscosity of 10^{26} Pa.s.

Figure 4.8

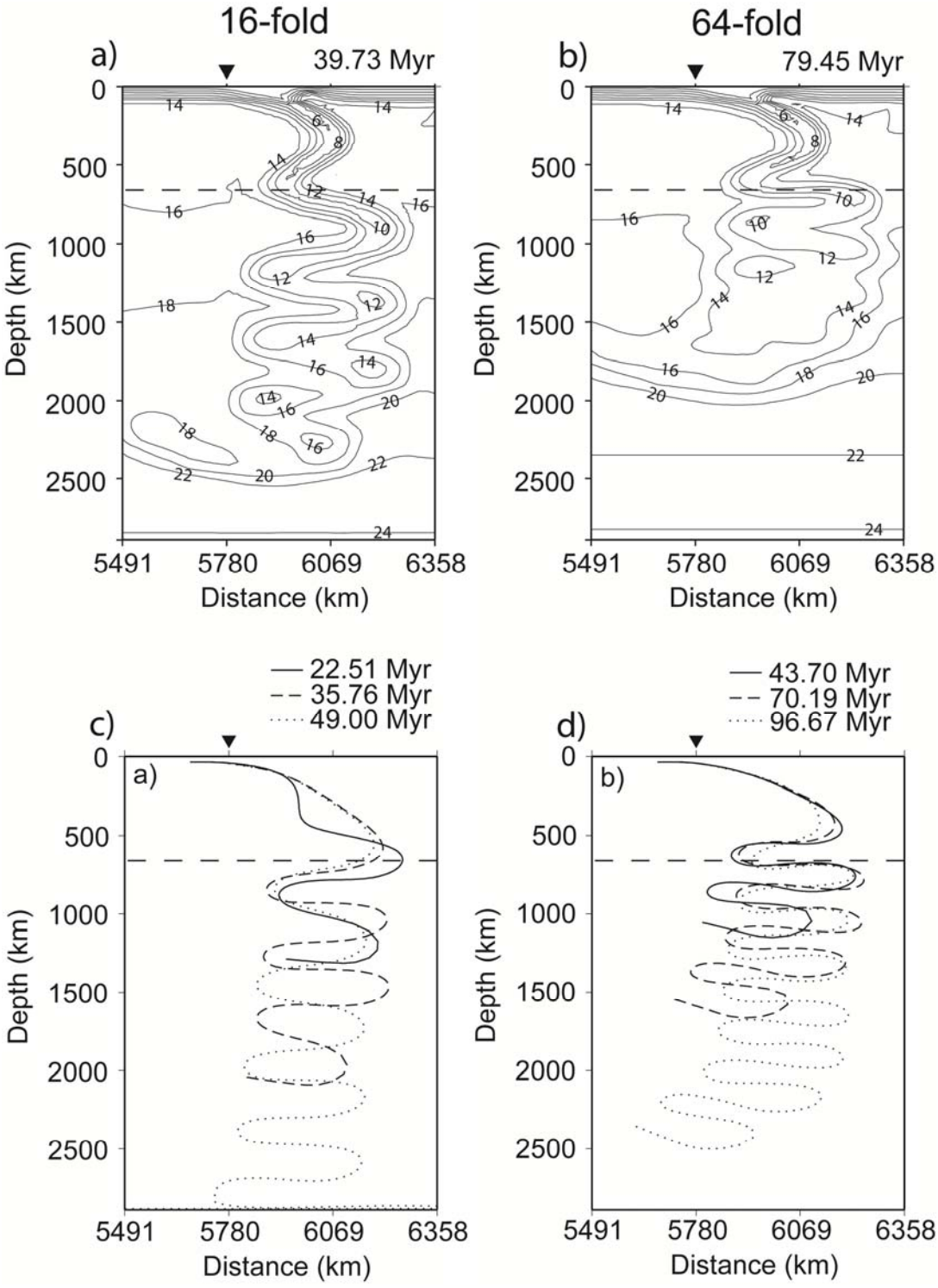

Snapshots of slab temperatures and trajectories corresponding to the experiments using 16- and 64-fold viscosity increases and phase transitions. The other notations are same with Figure 3.

Figure 4.9

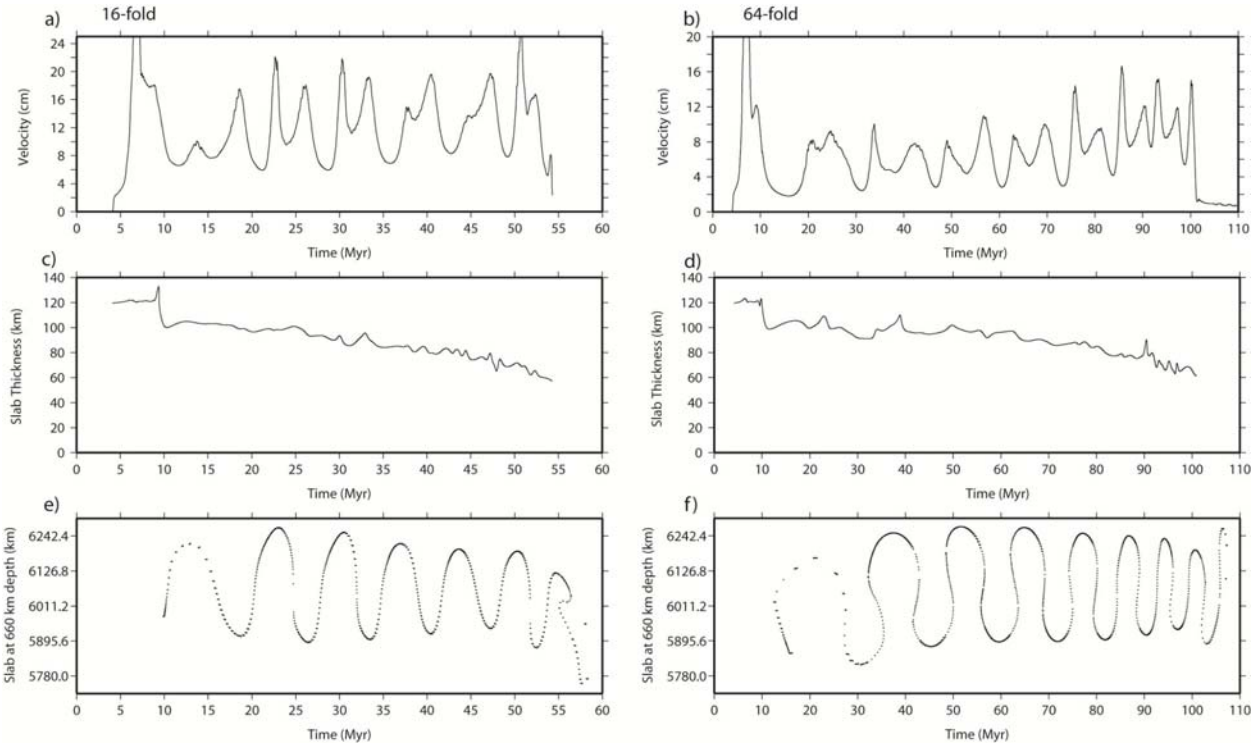

Convergence rate, slab thickness and time-evolving lateral amplitude of the subducting slab at the 660 km discontinuity corresponding to the experiments using 16- and 64-fold viscosity increases and phase transitions. The other notations are same with Figure 4.

Figure 4.10

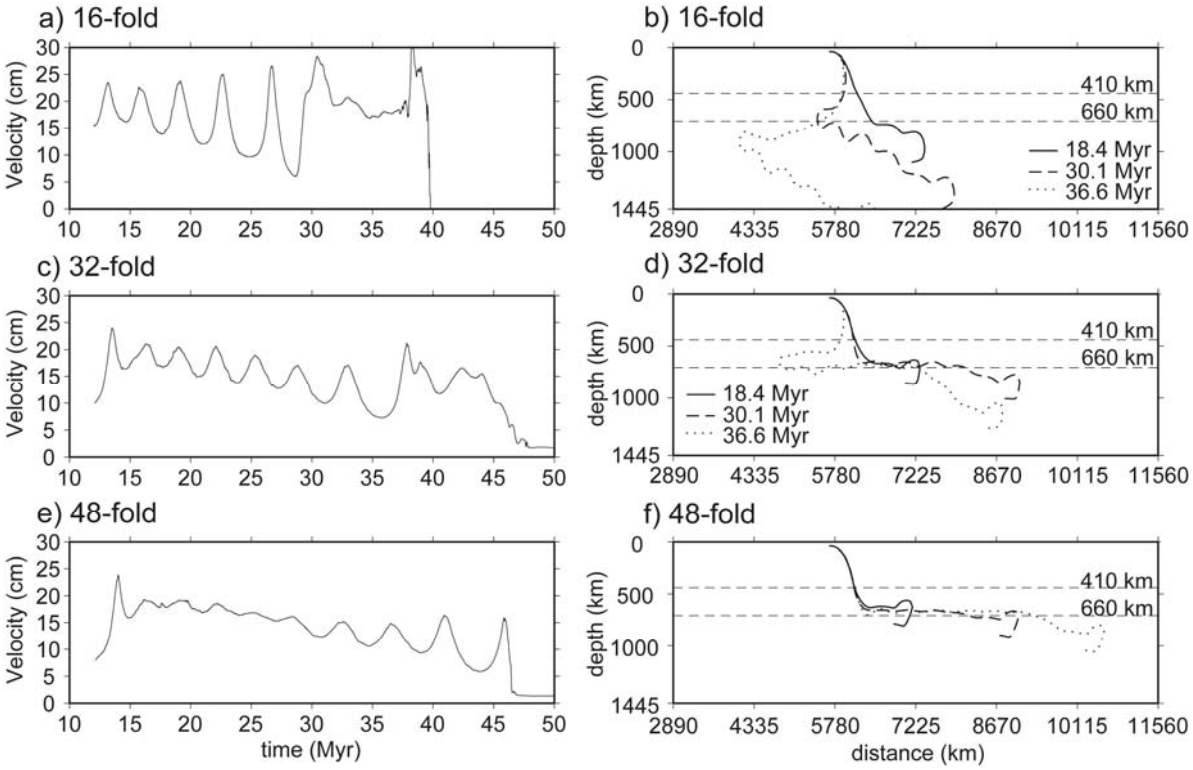

Convergence rate and slab trajectories of the experiments using the flow-through boundary conditions and phase transitions. Larger increases in viscosity across the 660 km discontinuity such as 48-fold efficiently suppress slab descending into the lower mantle (f).

Figure 4.11

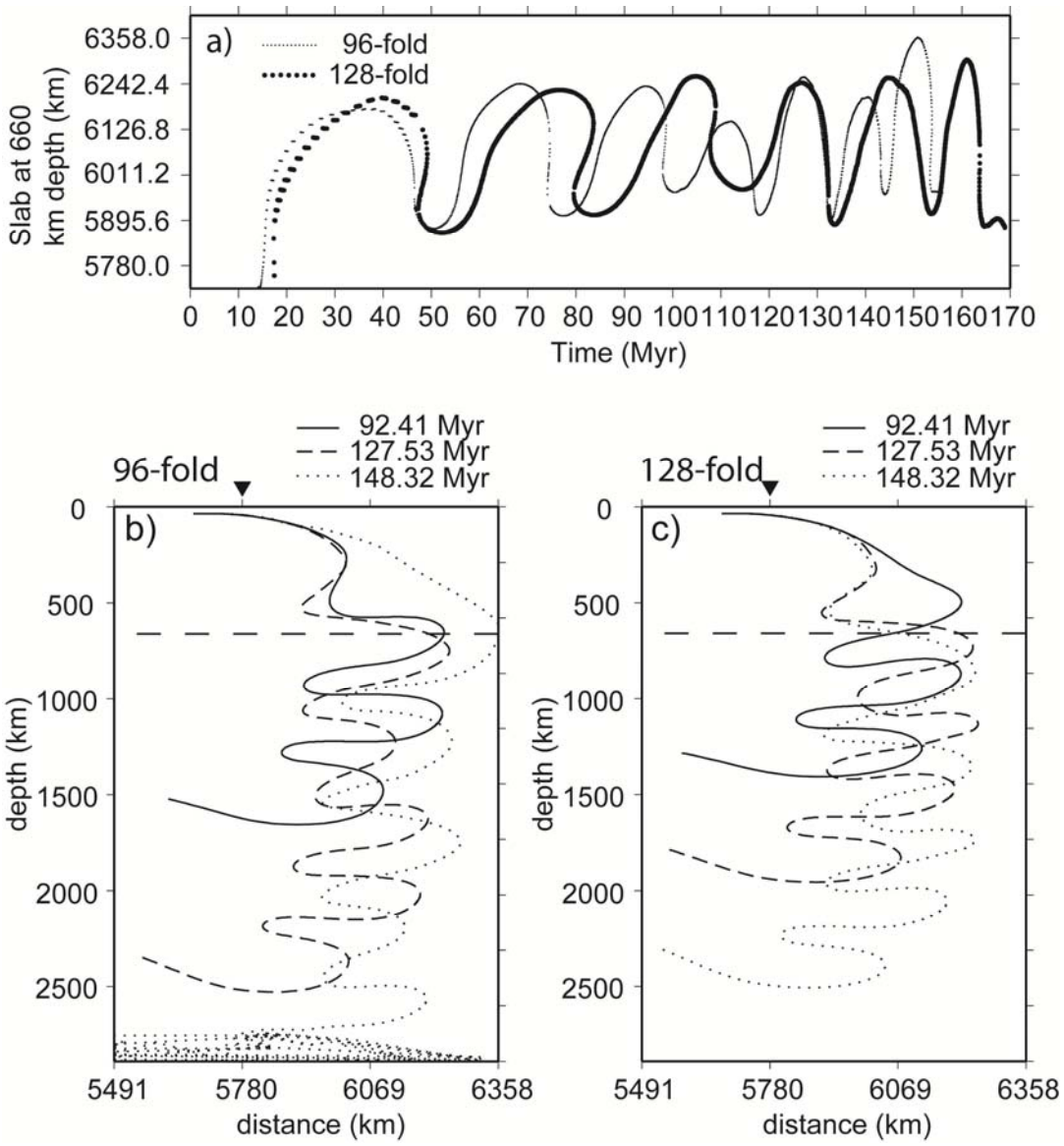

Time-evolving lateral amplitude of the subducting slab at the 660 km discontinuity (a) and snapshots of the slab trajectories corresponding to the experiments using 96- and 128-fold viscosity increases with the compressible fluid approximation (b and c). Slab detaches at 155 and 169 Myr for the experiments using 96- and 128-fold viscosity increases, respectively.

Figure 4.12

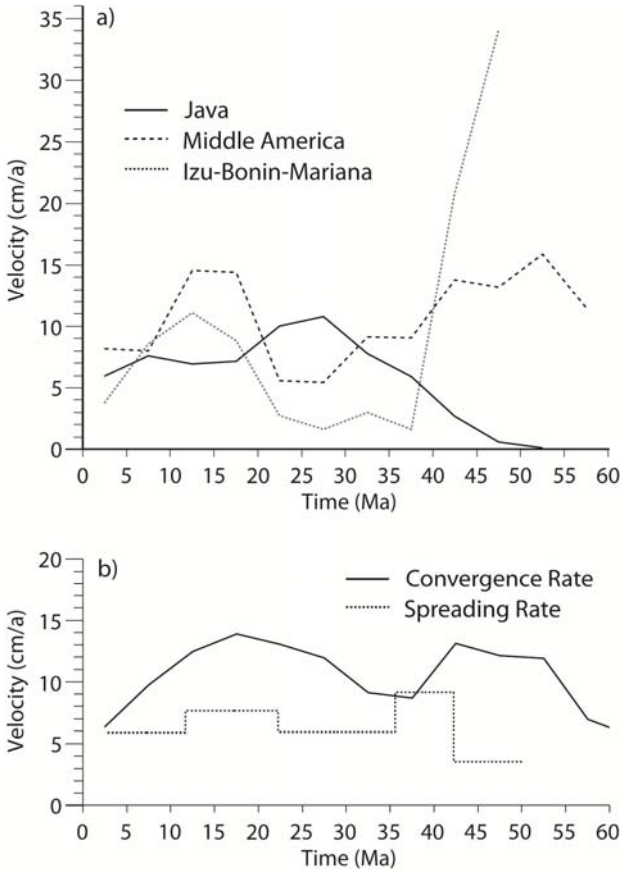

a) Convergence rates at the Java, Middle America and Izu-Bonin-Mariana arcs [*Sdrolias and Müller*, 2006]. The convergence rates do not significantly vary along the trench and median values are used. b) Median convergence rate at the Andes arc and averaged half-spreading rate at the mid-ocean ridge (East Pacific Rise) of the Nazca plate from Sdrolias and Müller [2006] and Cogné and Humler [2004], respectively. For a and b, the convergence rate are depicted by averaging the convergence rate every 5 Ma.

Figure 4.13

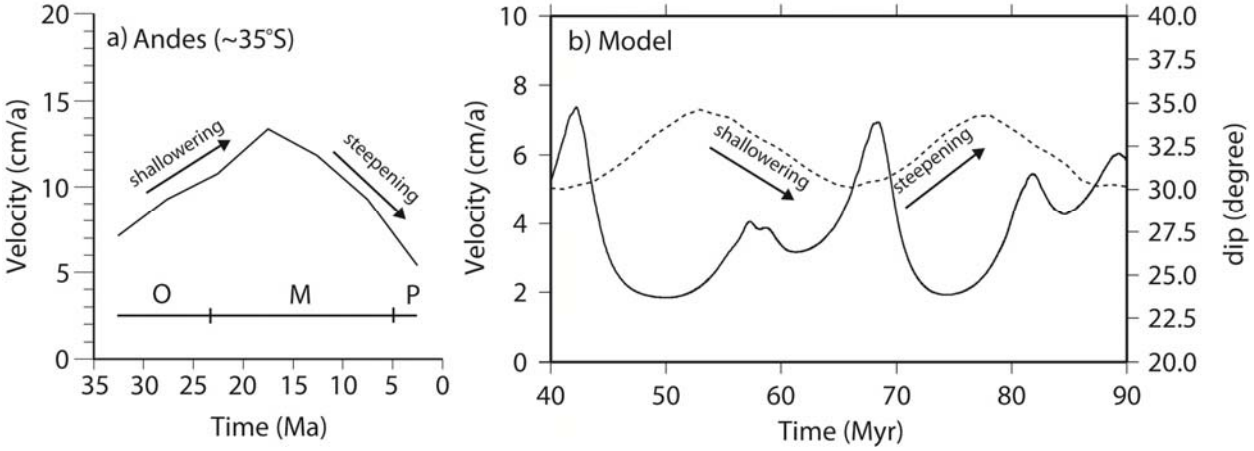

a) Convergence rate at the Andes arc estimated at ~35˚S from Sdrolias and Müller (2006). The convergence rate is depicted by averaging the convergence rate every 5 Ma. O, M and P correspond to Oligocene, Miocene and Pliocene. b) Convergence rate and dip of the subducting slab from the experiment using a 64-fold viscosity increase. The dashed line corresponds to the dip of the subducting slab at 150 km depth.

Chapter 5

Future directions in subduction research

In the studies described in this thesis, I show that time-dependent convergence rate and slab dip developed by buckling of the slab is Earth's natural expressions of subduction (Chapter 4) and that the effect of compressibility on subduction is minor (Chapter 2 and 4). Our understanding of subduction zones related to temporal and spatial evolution of arc volcanisms can be considerably improved when time-dependent, as opposed to steady-state subduction models, are considered (Chapter 3 and 4). However, the effects of trench migration constrained by plate reconstruction on buckling behavior of the slab have not been systematically evaluated- a future study to be tested in 2-D kinematic/dynamic subduction models. In addition, all the studies described in this thesis are based on 2-D Cartesian models where we consider a cross section normal to the trench; 3-D aspects of subduction zones, such as along-strike variations of trench geometry, convergence rate and slab age, cannot be considered. Therefore, another future study should focus on the time-dependence of the subduction parameters (convergence rate, slab age and trench migration) in 3-D models in order to evaluate the influence of 3-D aspects of subduction zones; 4-D (time + 3-D domain) models. Here, I briefly describe several suitable future studies for time-dependent 2-D and more importantly 4-D subduction models.

5.1 Future studies (time-dependent 2-D subduction models)

5.1.1 Effect of Trench Migration on Buckling Behavior of the Subducting Slab; A General Study

As discussed in the limitations and caveats to the work presented in Chapter 4, the most significant difference in buckling behavior of the slab is between the models with no trench migration and significantly fast trench migration; fast trench migration efficiently suppress slab buckling. The reflecting boundary conditions might be suitable for the subducting slab that has been surrounded by other

subducting slabs which may confine the mantle flows and/or that has experienced negligible trench migration (e.g., the Mariana subduction system) [*Fukao et al.*, 2001; *Li et al.*, 2008]. However, plate reconstruction models show that most of the subduction zones have experienced some amount of trench migration influencing the buckling behavior of the slab. Therefore, a systematic study is required to investigate the effect of trench migration on buckling behavior of the subducting slab by varying the migration rate from zero to the value from the experiments using the flow-through boundary conditions described in Chapter 4. However, as discussed in Chapter 4, it is difficult that the convergence and trench migration rate dynamically evolve as what constrained by the plate reconstruction models. As an alternative to control the trench migration, Chen and King [1998] imposed velocities along the side-walls of the computational domain to imitate trench migration. Using the imposed velocities, the influence of the trench migration on the slab buckling behavior can be tested. The buckling behavior of the slab constrained by such a study could be compared with seismic tomography images.

5.2 Future studies (4-D subduction models)

5.2.1 Distribution of High Mg# Andesites in the Aleutian Island Arc: time-dependent 3-D Numerical Model Approach

The next step for the Aleutians should be 4-D kinematic-dynamic subduction modeling to evaluate the effect of trench geometry and oblique convergence on distribution of high Mg# andesites in the Aleutian island arc, an improved study based on the time-dependent 2-D kinematic-dynamic subduction models described in Chapter 3. For the 2-D subduction models, the trench-normal vector of the convergence velocity was used for the convergence rate at the eastern and western Aleutians. However, plate reconstruction models [*Sdrolias and Müller*, 2006] show that there is a significant component of oblique convergence of the incoming Pacific plate to the Aleutian trench and, that this component becomes increasingly significant throughout the western Aleutians (Figure 1 in Chapter 3). Thus, the large trench-parallel vector of the oblique convergence velocity in the western Aleutians may

drive lateral mantle flow in the mantle wedge, which may change thermal and flow structures different than those from the 2-D subduction models. The steady-state 3-D subduction model experiments conducted by Honda and Yoshida (2005) show that the experiments using trench-normal vector of the oblique convergence velocity result in similar thermal and flow structures of the experiments using oblique convergence velocity. However, the combined effects of the concave Aleutian trench and oblique convergence of the incoming Pacific plate on the thermal and flow structures of the mantle wedge and subducting slab have not been evaluated. Through 4-D subduction models, the distribution of slab melting responsible for high Mg# andesites could be constrained and compared with the petrological and geochemical observations in the Aleutian island arc, building on the 2-D time-dependent work presented in Chapter 3.

5.2.2 Effect of Asymmetric Trench Roll-back on Slab Morphology in the Izu-Bonin-Mariana (IBM) Subduction System

The intraplate Izu-Bonin-Mariana (IBM) subduction system has been a focus for Earth scientists for decades [*Ben-Avraham and Uyeda*, 1983; *Hall et al.*, 1995; *Bryant et al.*, 2003; *Straub et al.*, 2009]. Bathymetry studies across the IBM subduction system show the characteristic trench geometry; a relatively-straight trench along the Izu-Bonin subduction system is changed into a concave trench in the Mariana subduction system. The origin of the concave trench is thought to be caused by the subduction of the low-density Ogasawara plateau at the north-end Mariana trench since mid-Miocene [*Mason et al.*, 2010]. Along with the trench geometry, seismic tomography images show the unique slab morphology in the IBM subduction system [*Fukao et al.*, 2001; *Miller et al.*, 2005; *Li et al.*, 2008]. Below the backarc of the Izu-Bonin subduction system, the subducted slab is stagnant above the 660 km discontinuity without apparent slab thickening. Unlike the stagnant slab in the Izu-Bonin subduction system, the slab below the backarc of the Mariana subduction system steeply subducts in the upper mantle and experiences apparent slab thickening in the shallow lower mantle.

Laboratory and numerical experiments show that stagnant slabs above the 660 km discontinuity develop when the trench roll-back is significant [*Zhong and Gurnis*, 1995; *Christensen*, 1996; *Funiciello et al.*, 2003a; *Funiciello et al.*, 2003b; *Enns et al.*, 2005]. In Chapter 4, stagnant slabs are observed in the experiments using flow-through boundary conditions which imitate trench migration (Figure 10 in Chapter 4). Thus, the stagnant slab in the Izu-Bonin subduction system could be attributed to the trench roll-back along the Izn-Bonin trench. Previous studies and the calculations in Chapter 4 (Figure 3b in Chapter 4) show that the slab buckling develops in stationary subduction systems with little influence of the trench migration [*Enns et al.*, 2005; *Behounková and Cízková*, 2008]. Therefore, the steeply subducting slab and apparent slab thickening (slab buckling) in the Mariana subduction system is through to have developed under a trench that has been stationary since the initiation of subduction. The along-strike variations of the slab morphology require significant trench roll-back in the Izu-Bonin subduction system and a stationary trench in the Mariana subduction system. Recent plate reconstruction models hint at the along-strike variations of trench migration in the IBM subduction system. Sdrolias and Müller [2006] show that the IBM subduction system has experienced asymmetric trench roll-back with a hinge located at the south end of the Mariana subduction zone ever since the initiation of subduction at ~50 Ma; the trench along the IBM subduction system rotates clockwise (Figure 4b in Sdrolias and Müller, 2006). Therefore, the asymmetric trench roll-back is consistent with the asymmetric slab morphology along the IBM subduction system.

Although the asymmetric slab morphology along the IBM subduction system can be intuitively understood, the detailed effect of asymmetric trench roll-back on the slab morphology can be essentially tested through 3-D subduction model experiments. Although several 3-D subduction models were carried out in order to infer the slab morphology in the IBM subduction system [e.g., *Piromallo et al.*, 2006; *Mason et al.*, 2010] asymmetric trench roll-back has not been considered. Thus, a focused study is to evaluate the effects of asymmetric trench roll-back (migration) on the slab morphology by using a series of 4-D subduction model experiments.

The first step should be to formulate a 4-D subduction model where asymmetric trench roll-back is kinematically prescribed with time-dependent convergence rate and slab age. The asymmetric trench roll-back, convergence rate and plate age will be constrained by the plate reconstruction model from Sdrolias and Müller [2006]. While the incoming oceanic plate is kinematically controlled, deformation of the subducting slab in the mantle is dynamically governed. The calculations in Chapter 4 and previous studies show that slab buckling develops in both kinematic and dynamic subduction model experiments [*Behounková and Cízková*, 2008]. Therefore, the kinematic subduction experiments would be sufficient to allow stagnant slab or steep slab subduction with slab buckling. This study would be a first-order approximation in order to understand the effect of asymmetric trench roll-back on the slab morphology in the IBM subduction system.

Following this study, subduction of the Ogasawara plateau and dynamically controlled trench roll-back can be separately tested and compared with the kinematic subduction experiments above. Mason et al. [2010] show that the low-density Ogasawara plateau which is reluctant to subduct develops slab tearing at the north end of the Mariana subduction system. If the plateau develops slab tearing, the slab tearing physically separates the subducting slab into two parts; the northern slab influenced by trench roll-back and the southern slab under the influence of the stationary trench. The slab tearing may contribute to easier development of the stagnant slab in the Izu-Bonin subduction system because the slab is independently controlled by the trench roll-back without the interference of the steeply subducting slab in the Mariana subduction system.

References

Behounková, M., and H. Cízková (2008), Long-wavelength character of subducted slabs in the lower mantle, *Earth and Planetary Science Letters*, *275*(1-2), 43-53.

Ben-Avraham, Z., and S. Uyeda (1983), Entrapment origin of marginal seas: in Geodynamics of the Western Pacific-Indonesian Region, Geodyn. Ser, *11, edited by T. W. C. Hilde and S. Uyeda*, 91-104, AGU, Washington D. C..

Bryant, C. J., R. J. Arculus, and S. M. Eggins (2003), The geochemical evolution of the Izu-Bonin arc system: A perspective from tephras recovered by deep-sea drilling, *Geochemistry Geophysics Geosystems*, *4*(11), 1094. doi: 10.1029/2002gc000427

Chen, J. N., and S. D. King (1998), The influence of temperature and depth dependent viscosity on geoid and topography profiles from models of mantle convection, *Physics of the Earth and Planetary Interiors*, *106*(1-2), 75-92.

Christensen, U. R. (1996), The influence of trench migration on slab penetration into the lower mantle, *Earth and Planetary Science Letters*, *140*(1-4), 27-39.

Enns, A., T. W. Becker, and H. Schmeling (2005), The dynamics of subduction and trench migration for viscosity stratification, *Geophysical Journal International*, *160*(2), 761-775.

Fukao, Y., S. Widiyantoro, and M. Obayashi (2001), Stagnant slabs in the upper and lower mantle transition region, *Review of Geophysics*, *39*(3), 291-323.

Funiciello, F., C. Faccenna, D. Giardini, and K. Regenauer-Lieb (2003a), Dynamics of retreating slabs: 2. Insights from three-dimensional laboratory experiments, *Journal of Geophysical Research*, *108*(B4), 2207.

Funiciello, F., G. Morra, K. Regenauer-Lieb, and D. Giardini (2003b), Dynamics of retreating slabs: 1. Insights from two-dimensional numerical experiments, *Journal of Geophysical Research*, *108*(B4), 2206.

Hall, R., J. R. Ali, C. D. Anderson, and S. J. Baker (1995), Origin and motion history of the Philippine Sea Plate, *Tectonophysics*, *251*(1-4), 229-250.

Li, C., R. D. van der Hilst, E. R. Engdahl, and S. Burdick (2008), A new global model for P wave speed variations in Earth's mantle, *Geochemistry Geophysics Geosystems*, *9*(5), Q05018. doi: 10.1029/2007gc001806

Mason, W. G., L. Moresi, P. G. Betts, and M. S. Miller (2010), Three-dimensional numerical models of the influence of a buoyant oceanic plateau on subduction zones, *Tectonophysics*, *483*(1-2), 71-79.

Miller, M. S., A. Gorbatov, and B. L. N. Kennett (2005), Heterogeneity within the subducting Pacific slab beneath the Izu-Bonin-Mariana arc: Evidence from tomography using 3D ray tracing inversion techniques, *Earth and Planetary Science Letters*, *235*(1-2), 331-342.

Piromallo, C., T. W. Becker, F. Funiciello, and C. Faccenna (2006), Three-dimensional instantaneous mantle flow induced by subduction, *Geophysical Research Letters*, *33*(8), L08304, doi: 10.1029/2005gl025390

Sdrolias, M., and R. D. Müller (2006), Controls on back-arc basin formation, *Geochemistry Geophysics Geosystems*, *7*(Q04016), doi:10.1029/2005GC001090.

Straub, S. M., S. L. Goldstein, C. Class, and A. Schmidt (2009), Mid-ocean-ridge basalt of Indian type in the northwest Pacific Ocean basin, *Nature Geosciences*, *2*(4), 286-289.

Zhong, S. J., and M. Gurnis (1995), Mantle convection with plates and mobile, faulted plate margins, *Science*, *267*(5199), 838-843.